DESIGN AND APPLICATIONS OF A Z-GRADIENT ARRAY IN MAGNETIC RESONANCE IMAGING

A DISSERTATION SUBMITTED TO

THE GRADUATE SCHOOL OF ENGINEERING AND SCIENCE

OF BILKENT UNIVERSITY

IN PARTIAL FULFILLMENT OF THE REQUIREMENTS FOR

THE DEGREE OF

DOCTOR OF PHILOSOPHY

IN

ELECTRICAL AND ELECTRONICS ENGINEERING

By

Niyazi Koray Ertan

January 2019

DESIGN AND APPLICATIONS OF A Z-GRADIENT ARRAY IN MAGNETIC RESONANCE IMAGING

By Niyazi Koray Ertan

January 2019

We certify that we have read this dissertation and that in our opinion it is fully adequate, in scope and in quality, as a dissertation for the degree of Doctor of Philosophy.

Ergin Atalar(Advisor)

Emine Ülkü Sarıtaş Çukur

Behçet Murat Eyüboğlu

Özgür Salih Ergül

Yusuf Ziya İder

Approved for the Graduate School of Engineering and Science:

Ezhan Karaşan
Director of the Graduate School

ABSTRACT

DESIGN AND APPLICATIONS OF A Z-GRADIENT ARRAY IN MAGNETIC RESONANCE IMAGING

Niyazi Koray Ertan
Ph.D. in Electrical and Electronics Engineering
Advisor: Ergin Atalar
January 2019

Array of gradient coils driven by independent power amplifiers can generate gradient fields with dynamically changing gradient field profiles. Nine channel prototype z-gradient coil array with a diameter of 25 cm is designed and manufactured. Previously designed gradient power amplifiers with maximum voltage of 50 V and maximum current of 20 A are used to independently drive the coils. Mutual coupling between gradient coils are investigated to maintain high time fidelity in the gradient waveform. A first-order circuit model including the mutual couplings is provided to analytically calculate the input voltages and minimum achievable rise times for a given set of gradient array currents and amplifier limitations. Mutual impedance of the system is measured which is in a good agreement with the first order circuit model inside the operating bandwidth of the amplifiers (<10kHz). An example z-gradient profile is optimized and used in Magnetic Resonance Imaging (MRI) phantom experiment as a readout gradient. After validating the proper functioning of the hardware with current measurements and MRI experiments, advantages of dynamically arrangeable field profiles generated by z-gradient array are investigated.

Firstly, linear gradient in variable Volume of Interests (VOIs) with variable linearity errors are optimized with four different performance parameters such as maximization of gradient strength for unit amplifier current limits, maximization of slew rate for unit amplifier voltage limits, minimization of current norm and peak vector B-field for a unit gradient strength. Decreasing the size of the gradient VOI and allowing more linearity error increases all performance parameters more than five times among the sweep ranges. The advantage of dynamic field optimization is demonstrated in Diffusion Weighted Imaging (DWI). Maximization of gradient fields only inside the slice volume rather than entire coil volume results in 4 times higher gradient strength which decreases the diffusion encoding gradient duration 3 times and halves the echo time. Increased signal to noise ratio (SNR) of the diffusion weighted images results in better estimate for the apparent diffusion coefficient (ADC) values inside the phantom.

Secondly, gradient array is also capable of generating nonlinear gradient field distributions. In addition to many applications of nonlinear gradients in MRI, two novel applications based on nonlinear gradients are proposed. In the first application, nonlinear gradients are used to encode multiple slice locations to the same frequency. Excitation of multiple slices is achieved with a single band radio frequency (RF) pulse in contrast to multi-band RF pulses with higher specific absorption rate (SAR) and peak power. Two different field design method is presented and both of them are analyzed in terms of slice thickness error, center location variation, gradient strength per unit norm current, power dissipation. Two and three slices are excited with a single band RF pulse in phantom experiments. In the second application, a single channel nonlinear gradient field is simultaneously used with linear gradients during spoke excitation to mitigate the B_1^+ inhomogeneity. Excitation k-space with increased dimension are introduced for simultaneous use of linear and nonlinear gradients by including independent k-space variables for nonlinear gradient channel. Simulations are performed for 1D, 2D, RF power limited and RF power unlimited cases to demonstrate the enhanced B_1^+ homogeneity for simultaneous use of linear and nonlinear gradients compared to using only linear or only nonlinear gradients. Proposed method results in 2.3 times more decrease in the excitation inhomogeneity compared to using only linear gradients in MRI experiments.

Keywords: Gradient array, Nonlinear gradients, NSEM, RF Excitation, B1 inhomogeneity, SAR, Dynamic Gradient Optimization, DWI, Diffusion MRI, SMS, Multi-slice Excitation, Field Monitoring, Hall Effect, Gradient Linearity, Mutual Coupling.

ÖZET

Z-GRADYAN DİZİSİNİN TASARIMI VE MANYETİK REZONANS GÖRÜNTÜLEMEDEKİ UYGULAMALARI

Niyazi Koray Ertan
Elektrik ve Elektronik Mühendisliği, Doktora
Tez Danışmanı: Ergin Atalar
Ocak 2019

Bağımsız gradyan güç yükselteçleri tarafından sürülen gradyan sargı dizileri dinamik olarak ayarlanabilen manyetik alan profilleri yaratabilirler. Bu doğrultuda, 25 cm çapında 9 kanallı bir gradyan sargı dizisi tasarlanmış ve üretilmiştir. Daha önceden tasarlanan, 50 V voltaj ve 20 A akım sağlama kapasitesine sahip güç yükselteçleri, sargıları bapımsız olarak beslemek için kullanılmıştır. Gradyan sarımlardaki yüksek akım hassasiyetini sağlayabilmek için bu sargılardaki karşılıklı kuplaj değerlendirilmiştir. Karşılıklı kuplaj etkisini de içeren birinci dereceden bir devre modeli önerilmiştir. Bu model, verilen bir gradyan akım seti ve güç yükselteç limitleri için gerekli olan voltajları ve elde edilebilecek minimum çıkış süresini analitik olarak hesaplanmasını sağlamaktadır. Karşılıklı kuplaj ve kanallar arasındaki empedanslar ölçülmüş ve önerilen birinci devre modeli ile güç yükselteçlerinin çalışma bandı içerisinde (<10kHz) uyumluluk gözlenmiştir. Örnek bir z-gradyan alanı için eniyileştirme yapılmış ve bu alan Manyetik Rezonans Görüntüleme (MRG) deneylerinde frekans kodlayıcı gradyan olarak kullanılmıştır. Gradyan dizisi donanımının uygun bir şekilde çalıştığı akım ölçümleri ve MRG deneyleri ile tasdiklendikten sonra dinamik olarak ayarlanabilen alan profillerinden kaynaklı avantajlar araştırılmıştır.

İlk olarak, farklı boyutlardaki hedef hacimlerde oluşturulan doğrusal gradyanlar, değişken doğrusallık hataları belirlenerek dört parametre için eniyileştirme yapılmıştır. Bu parametreler birim yükselteç akımı ile oluşturulabilecek maksimum gradyan gücü, birim yükselteç voltajı ile oluşturulabilecek olan maksimum çıkış hızı (slew rate), birim gradyan gücü için gerekli olan minimum akım normu ve minimum manyetik alan tepe değeridir. Daha küçük hacimlerde ve daha yüksek doğrusallık hataları ile bu parametrelerinde her birinde simulasyonlarda süpürülen değerler arasında 5 kattan fazla artış gözlenmiştir. Buradan kaynaklanan avantaj difüzyon ağırlıklı görüntülemeye uygulanmıştır. Doğrusal gradyan alanı yalnızca ilgili kesit içerisinde eniyileştirildiğinde, sargının

bütün hacminde yapılan eniyileştirmeye oranla, gradyan gücünde 4 kat artış elde edilmiştir. Bu difüzyon gradyan süresini 3 kat azaltmıştır ve eko zamanını yarıya indirmiştir. Artan sinyal gürültü oranı sayesinde fantom için hesaplanan ADC haritalarında daha iyi tahminler yapılmıştır.

İkinci olarak, gradyan dizileri doğrusal olmayan gradyanlar üretebilirler. Doğrusal olmayan gradyanlar sayesinde iki yenilikçi uygulama geliştirilmiştir. İlk uygulamada, doğrusal olmayan gradyanlar birden çok kesit pozisyonunu tek bir frekansa şifrelemek için kullanılmıştır. Bu sayede, tek bantlı bir RF darbe ile çoklu kesit seçimi gerçekleştirilmiştir. Geleneksel çoklu kesit seçimlerinde kullanılan RF darbelerinden kaynaklanan SAR ve RF tepe gücü artışı gibi dezavantajlar engellenmiştir. Bu tekniği gerçekleştirebilmek için iki farklı tasarım yöntemi önerilmiştir. İki yöntem de kesit kalınlığı hatası, merkez nokta kayması, gradyan gücü ve güç tüketimi açısından incelenmiş ve karşılaştırılmıştır. Fantom MRG deneylerinde, tek bantlı RF darbe ile iki ve üç kesit uyarımı sağlanmıştır.İkinci uygulamada, tek kanallı bir doğrusal olmayan gradyan, doğrusal gradyanlar ile spoke uyarımı sırasında eşzamanlı kullanılarak B_1^+ düzensizliklerinden kaynaklı uzaysal uyarım düzensizliklerini azaltmak için kullanılmıştır. Doğrusal olmayan gradyanlar için bağımsız bir k-uzay değişkeni tanımlanarak, problem bir boyut genişlemiş uyarım k-uzayında tekrar ifade edilmiştir. Tek boyutlu, iki boyutlu, RF güç limitli ve RF güç limitsiz olmak üzere simulasyonlar yapılmıştır. Önerilen yöntem MRG deneylerindeki uyarım düzensizliklerini sadece doğrusal gradyanların kullanıldığı duruma oranla 2.3 kat daha fazla azaltmıştır.

Anahtar sözcükler: Gradyan Dizisi, Doğrusal Olmayan Gradyanlar, NSEM, Radyo Dalga Uyarımı, B1 düzensizliği, Özgül Soğurulma Hızı, Dinamik Gradyan Optimizasyonu, Difüzyon Ağırlıklı Görüntüleme, Eşzamanlı Çoklu Kesit, Çoklu Kesit Uyarımı, Manyetik Alan İzleme, Hall Etkisi, Gradyan Doğrusallığı, Karşılıklı Kuplaj.

Acknowledgement

Although I do not feel comfortable squeezing the invaluable memories shared with amazing people into a few pages, I could not ignore the possibility that these pages may act as a reminder of those memories both for me and the people who supported me during my PhD training.

First of all, I would like to express my deepest appreciation to Prof. Ergin Atalar. I have decided to pursue a PhD in medical imaging after taking his course and observing his research skills as an intern at his lab. His enthusiasm for teaching and research have excited me to learn how to teach and do research. His advices and contributions on my scientific, academic and personal life were remarkable. Most of his effort was on teaching to fish rather than giving one, which will guide me through all my academic life. He was quite supportive in personal issues and guided me to the correct direction whenever I felt lost. It was a privilege to work with him. Thank you for everything.

I would like to thank my jury members for spending their precious time on this dissertation and providing useful feedback. Prof. Emine Ülkü Sarıtaş Çukur made a great contribution on this thesis. She is also an encouraging mentor who has a significant role in my decision to continue research after the PhD. Prof. Murat Eyüboğlu was very kind to attend my numerous committee meetings even on short notice and commented on my work continuously. I thank Prof. Yusuf Ziya İder for several reasons. I learned a lot from him in his courses. He is a kind and experienced professor and I appreciate his realistic and honest advices throughout my undergraduate and graduate trainings. I also want to thank Prof. Özgür Ergül for his careful comments on this thesis from computational electromagnetics perspective.

Soheil (Süheyl) Taraghinia deserves a special thank for this thesis. He was always there to help me with the experiments and hardware related issues. I cannot imagine conducting endless experiments without him and his jokes. Apart from his significant contributions to almost all parts of the thesis, he is a very good friend and hopefully we can continue to work together in the future.

I am grateful to all UMRAM family for providing a productive research and social environment. Specifically, I thank Aydan Ercingöz for all the interesting talks and her patient attitude with the administrative issues. I feel very lucky to have Buse Merve Ürgen as a close friend and her continuous support. I enjoyed my therapy sessions with her. I hope she will let me continue to discuss some life-related questions in the future too. Cemre Arıyürek and I always had very much in common to talk about. The PhD (especially deadlines) would not be funny without her, and I will definitely miss working close to her. I am always impressed with the perspective of Umut Gündoğdu who is one of the best people I know. I would like thank him for his mentorship. I benefit a lot from Dr. Volkan Açıkel's experiences on both research and academic life. I thank him for all the cool things he taught to me. I learned a lot from our technical and social discussions with Taner Demir. I felt that I can always trust on his support during my PhD. Uğur Yılmaz was one of the most talented researchers that I have met and I was lucky to have scientific discussions with him. I thank Alireza Sadeghi-Tarakameh for his help in the research as well as his optimism for the academic life. I thank Arzu Ceylan Has and Berk Silemek with whom I have lived the craziest moments of my PhD. I thank Redi Poni for his practical ideas and being a cheerful friend. I also thank Ehsan Kazemi, Reza Babaloo, Reyhan Ergün and Said Aldemir for being great group members. We have laughed too much with Sevgi Kafalı and I want to thank her for all the small talks. I thank Toygan Kılıç for being a cheerful, trustworthy and funny friend. And finally, office life at UMRAM would have been too boring without Özgür Yılmaz, Yavuz Muslu, Alper Özaslan, Efe Ilıcak, Mustafa Ütkür, Ayşenur Karaduman, Cansu Öğülmüş, Zahide Pamir and Utku Kaya. I thank Dr. Ali Çağlar Özen, Dr. Emre Kopanoğlu, Dr. Esra Abacı Türk and Dr. Can Kerse for motivating me at the beginning of my PhD.

I also want to thank my close friends who supported me not only during my PhD but also during my entire life. These are the people that I have grown up with and they have all contributed to my personality. I would like to thank Berkay Akyapı for his ideas, kindness and awesome friendship. I hope we can live in the same city again. I thank Can Önol for being a very smart and funny friend and I hope we will be wrong about our future projections. I thank Alper Yoğurt for his friendship beginning from high school. I am always inspired by his passion for science without pragmatism. I thank Erdem Karagül for providing very strong support during my darkest days and triggering my interest in philosophy. I thank my best friends Emre Yeşilyurt, Yalım Can Arslan and Harun Yöney for being like a brother to me. If I did not meet Emre, I would have written this thesis at least a year ago. I do not regret any minute that we spent for fun. I thank all of you for making me laugh, enlarging my vision. I will always count on your support.

I cannot find a way to thank Beril Aydın for all her support. She is always the source of my cheer. She has not only tolerated all my stress and changed my mood, but she has also given me the power I need to move forward in life. She has been with me in all my good and bad moments during my PhD training. She has supported me on every decision I make and wanted the best for me all the time. I am already very excited for our future life. I thank you for standing by me.

I would like to thank my father, Nazmi Ertan for all his support. My mother, Sevgi Ertan, deserves the most important credit in this thesis as well as all my life. She is the best mother that I can imagine, and I dedicate this thesis to my beautiful and lovely mother. There is no way to thank her enough.

I should limit the list at this point; however, I also thank to other colleagues, friends and family members for all their help and support. I would also like to thank The Scientific and Technological Council of Turkey (TÜBITAK), BIDEB 2211 Program for funding me during my PhD studies.

Contents

List of Figures

List of Tables

Chapter 1

Introduction

Magnetic Resonance Imaging (MRI) is one of the most commonly used imaging techniques in clinical applications and neuroscience. In a regular MRI scan, 3 linear gradient fields in rectangular coordinates are used to encode spatial information of the object to the frequency. Linear gradients provide linearly changing magnetic field in the direction of B_0; therefore, every linear gradient field produces iso-frequency lines in the corresponding direction which allows one-to-one mapping of spin coordinates to frequency.

In conventional MRI scanners, there are three gradient coils generating three different type linear gradient field which corresponds three physical axes. Each coil is driven by gradient power amplifiers (GPAs) with voltage and current specifications around 2000 V and 1000 A for modern whole body scanners. During the design stage of gradient coils, target magnetic fields are specified in terms of gradient linearity error, total inductance, power dissipation and peripheral nerve stimulation characteristics in a certain volume [1]. After manufacturing the gradient coils, these parameters and field profiles cannot be altered, can only be scaled by modulating amplifier outputs. These specifications and target volume are generally determined based on a general MRI application. Although conventional gradient coil works reasonably well for most of the applications, they do not generate optimal fields for each sequence, each target organ and application. Additionally, nonlinear gradient fields with arbitrary spatial dependency have already proven to be useful in many aspects of both the reception [2–9] and excitation [10–14] phases of an imaging sequence.

Main motivation behind this thesis is to design and implement a gradient array hardware that can generate dynamically changeable magnetic field profiles. Gradient array system consists of multiple gradient coils that can be independently driven by separate GPAs. Therefore, individual field profiles can be superposed dynamically to improve the encoding in MRI by either generating the linear gradient fields with dynamically adaptable parameters in target volume of interests (VOI)s only or generating nonlinear gradient fields for some novel applications. High degree of flexibility in the gradient field profile enables variety of novel applications with the expense of increased hardware complexity. In scope of this thesis, hardware solutions and novel applications are proposed to expedite the transition period of gradient array technology towards clinical applications.

In Chapter 2, z-gradient array hardware is introduced. Firstly, nine channel z-gradient coil array with a diameter of 25 cm is designed and manufactured. Each channel is wound continuously on a cylinder with total length of 27.5 cm. Continuous winding of the channel enables to modulate current density on the cylinder freely which increased the flexibility of field combinations that one can obtain. Magnetic field profile of each channel is both simulated using Biot-Savart law and measured using MRI experiments to ensure proper functioning of the coil array. Additionally, Gradient currents requires high time-fidelity for artifact free MR images, driver system for the gradient array is explained. Gradient array systems might be mutually coupled. Although, it is theoretically possible to design the uncoupled coil elements, it decreases the degree of freedom in the design stage and it is impossible to obtain zero coupling practically due to the limited physical space and feed cables. Therefore, it is highly significant to consider mutual coupling in the driver part. Therefore, first order circuit model approximation for mutually coupled array coils including amplifier filters are proposed and validated with impedance meter measurements. This simple model enabled analytical calculation of minimum rise times for a given current waveforms and amplifier voltage limitations since rise time of each channel becomes dependent to current flowing through other channels due to coupling. Improved version of previously designed GPAs and user-interface [15] is also explained. Lastly, accurately driving mutually coupled gradient coil arrays are validated with both current measurements and MRI experiments. This hardware is utilized in all chapters except the Chapter 6. In Chapter 6, a single channel, similar z-coil with a slightly different radius is used in combination with system's linear gradients.

In chapter 3, it is demonstrated that the z-gradient coil array can generate dynamically changeable linear gradient profiles with various different parameters in different VOI shapes and lengths. Firstly, coil currents are optimized for minimum linearity error of the gradient fields inside a cylindrical and truncated ellipsoid VOIs with variable diameters and lengths. Secondly, an example spherical VOI with diameter of 20 cm is determined as an example VOI to investigate performance metrics of the system. Four optimization problems are formulated such as (1) maximum gradient strength per unit amplifier current limitations, (2) maximum slew rate per unit amplifier voltage limitations, (3) minimum current norm required to obtain unit gradient strength and (4) min amplitude of vectoral magnetic field inside the entire coil for a unit gradient strength. All optimization problems are constrained by maximum allowed gradient linearity error. Maximum allowed gradient linearity error and truncation length of the spherical VOI in z-direction is swept jointly to demonstrate that a z-gradient array can be dynamically changed to utilize the tradeoffs between the performance parameters of gradient fields.

In Chapter 4, advantage of dynamically adjustable field profiles are demonstrated in DWI. In DWI, sufficient contrast in diffusivity requires high b-values with either long gradient durations or high gradient strengths. Since gradient strength is limited by the GPAs in conventional scanners, duration of the diffusion encoding gradients should be increased. Increased duration of diffusion encoding gradient results in increased echo time (TE) and decreased signal to noise ratio (SNR) which decreases the diagnostic quality of DWI [16]. We propose to utilize the z-gradient array to maximize the gradient strength only inside a selected VOI where diffusion images will be acquired. Furthermore, gradient nonlinearity error might also be modulated in this VOI to further increase the gradient strength which results in spatially dependent b-value for apparent diffusion coefficient (ADC) calculations. Theory and formulations in Chapter 3 is used to design the gradient field profiles. Field profile simulations and DWI experiments are performed for two cases for comparison. In the first case, field profiles are design for all slices in VOI while imaging a single slice at the center. In the second case, field profiles are designed for only central z-slice where imaging occurs. In this comparison, it is demonstrated that maximizing the gradient fields only inside the current VOI and allowing more and more nonlinearity results in increased diffusivity estimation inside the phantom.

In Chapter 5, first example application of nonlinear gradients generated by the z-gradient coil array is explained. Multi-slice MRI is a tool to excite and image multiple slices simultaneously which either decreased the total scan time or increases SNR. Since conventional linear gradients provide one-to-one mapping between frequency and spatial coordinates, multi-slice excitation pulse involves multiple frequencies with increased specific absorption rate (SAR), peak radio frequency (RF) amplitude and power [17]. Although there are techniques for linear gradients to suppress the increase in RF pulse related parameters [18–26], multi-slice RF pulses have either higher durations or higher SAR compared to single slice RF pulses. Using the z-gradient array, it is demonstrated that multiple slice locations can be mapped to the same frequency; therefore, single slice RF pulses can be used to excite multiple slices without increase in the pulse duration or SAR. Field design techniques and formulations for two different proposed techniques are provided to design spatially oscillating magnetic field profiles. Limitations and performance parameters of this technique such as minimum slice separation, slice profile discrepancy and maximum attainable gradient strength is investigated using simulations. Lastly, MRI experiments is used to validate that excitation of multiple slices with a single band RF pulse is feasible using the z-gradient array.

In chapter 6, the advantage of using nonlinear spatial encoding magnetic fields (N-SEM)s, nonlinear gradients, simultaneously with linear spatial encoding fields

(L-SEM)s, linear gradients, in B_1^+ inhomogeneity correction is investigated. Although high main magnet strength scanners ($> 1.5T$) increases SNR [27], homogeneous excitation is more difficult challenge due to the fact that wavelength of the excitation field becomes comparable with the object dimensions [28, 29]. Inhomogeneous excitation might change the contrast characteristics of the image and decreases the diagnostic quality. In addition to the methods developed for conventional linear gradients in literature [29–34], nonlinear gradients can also be used to improve the homogeneity of the RF excitation [35, 36]. We propose to use single nonlinear gradient channel simultaneously with linear gradients to improve the B_1^+ homogeneity. Using an additional nonlinear gradient simultaneously with the linear gradients breaks the conventional Fourier relation between the excitation k-space and spatial distribution of excitation. Including the nonlinear gradients as an independent k-space dimension, Fourier transform relationship is re-established again. This formulation also shows the dramatic increase in the degree of freedom while using nonlinear gradients simultaneously with linear gradient. Global optimization problems are solved for both simulations and experiments to demonstrate that simultaneous use of L-SEMs and N-SEMs in the spoke excitation can result in either B_1^+ inhomogeneity correction with the same SAR level. Lastly, details for the first experimental validation of B_1^+ inhomogeneity correction using N-SEMs and L-SEMs simultaneously is provided.

In short, z-gradient array hardware is explained in Chapter 2 in terms of both coil design and drivers. The possible advantages of dynamically optimizing the linear gradients with different specifications are formulated and simulated in Chapter 3. An example advantage of dynamic field optimization in DWI is presented in Chapter 4. Chapter 5 and 6 discusses some example applications of nonlinear gradients in multi-slice excitations and B_1^+ inhomogeneity correction respectively. Finally, practical limitations of gradient array technology, some hardware challenges and future applications are discussed in Chapter 7.

Chapter 2

Gradient Array Hardware

The gradient coil array was already presented in the 33rd Annual Meeting of European Society of Magnetic Resonance in Medicine and Biology [37] and published in Magnetic Resonance Medicine [38]. Some of the content of this chapter including figures and texts are based on these publications. The second part of this chapter related to driving mutually coupled gradient array coils was presented in the 26th Annual Meeting of International Society for Magnetic Resonance in Medicine [39].

The hardware described in this chapter have been developed by a few collaborators. RF coil and its shield have been designed and manufactured by Alireza Sadeghi-Tarakameh. Mustafa Can Delikanlı assisted with the production of the array of coils. Gradient power amplifiers and the driver is initially described in Master Thesis of Soheil Taraghinia [15]. For the studies of this chapter, some adaptation has also been performed together with Soheil Taraghinia. User interface to program the gradient waveforms are initially developed by Sercan Aydoğmuş. Hamed Mohammadi has continuously developed the user-interface until its final version.

2.1 Introduction

In conventional MRI, linear gradients are used to encode the spatial coordinates of spins onto the resonance frequency. In the last decade, gradient coil arrays with arbitrary magnetic field profiles have proven to be useful for encoding purposes [40,41] at the expense of increased hardware complexity. In this study, a 9-channel z-gradient coil array is designed and manufactured.

A high number of array elements are likely to be mutually coupled even for orthogonal spherical harmonics field profiles [42], although there have been some efforts to reduce [41] or avoid mutual coupling between the channels [43]. On the other hand, driving mutually coupled gradient array coils is possible and might even be preferable to avoid the mutual coupling constraints in the coil design.

Providing high-fidelity and high-bandwidth currents for gradient array systems becomes a challenge since high-channel-count gradient elements can couple to each other because of the nonorthogonal magnetic field profiles. Gradient array systems should be considered as multiple-input-multiple-output (MIMO) systems, because the time-varying current in one element can change the current waveforms of the other elements. If the system can be assumed to be linear and time invariant (LTI), the frequency response of the system, including the cross terms, is measured. Once the system is known, appropriate predistortions can be applied to the input waveforms [42,44] to obtain the desired gradient waveforms. Inverting the frequency response of the system at a high bandwidth might be computationally expensive for a high number of channels and lacks an analytical expression that can be used to calculate the amplifier limitations.

Here, a first-order time domain model of driving mutually coupled array elements is developed and allows analytical calculation of the required input voltages for a given set of desired output currents. This analytical expression can be used to find the minimum achievable rise time for a given current combination of the coil arrays under the amplifier voltage limitations. The self- and cross-impedances of each element according to the proposed model are compared with impedance measurements in the operating bandwidth of the amplifiers (<10 kHz). The first-order model and expression for the minimum achievable rise time is validated in bench-top experiments with three different current combinations that generate a linear z-gradient and second- and third-order z-shim fields on a nine-channel low-cost home-built gradient array system. Finally, a driving mutually coupled gradient system is demonstrated with MRI experiments.

2.2 Z-Gradient Array

2.2.1 Physical Description of the Coil Array

The coil array is designed as a 9-channel coil array. It is wound on a plastic cylindrical shell with a diameter of 25 cm such that each identical array element is directly adjacent to its neighboring element as shown in Fig. 2.1a. Each element consists of 36 turns of a 0.85 mm thick copper wire. Because of the continuous winding of the gradient coil and non-zero wire thickness, each element is essentially a helical structure with a pitch angle of less than 0.1°. The feed cables for each channel are designed to be parallel to the z direction since theoretically, current flow in the z direction does not contribute to the magnetic field in the z direction, and force is not induced due to the main magnetic field. Furthermore, a birdcage Tx/Rx RF coil with a diameter of 21 cm and a total length of 22 cm is placed concentrically with the gradient coil array inside the cylindrical shell. As an RF shield, copper tape is glued to the inner portion of the cylindrical gradient holder, and parts of the shield are removed to form slits in the z direction to prevent eddy currents on the cylindrical shell due to gradient switching. At each slit, multiple 1 nF capacitors are soldered between the separate parts of the shield to maintain its proper functioning. The gradient coil array, the RF coil and the shield are shown in Fig. 2.1b.

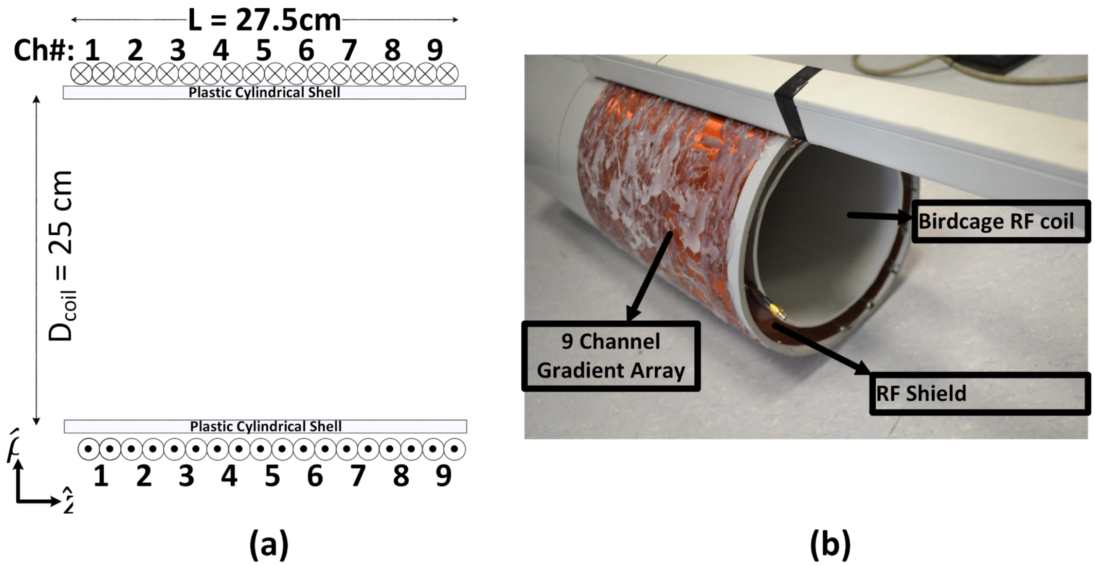

Figure 2.1: **(a)** Schematic illustration of the 9-channel z-gradient coil array, **(b)** the 9-channel z-gradient coil, the RF coil embedded inside the cylinder and the RF shield.

2.2.2 Magnetic Field Profiles

After successful construction of the 9-channel z-gradient coil array, magnetic field profile of each channel is simulated and measured for validation. The vector magnetic field profile of each channel was simulated with a 0.2 mm spatial resolution using the Biot-Savart law. Although Biot-Savart law assumes that magnetic field does not vary as function of time, it is commonly used approximation in literature [1]. Since wavelength at the operating frequency of gradients (<10kHz) is much lower than the coil dimensions, this approximation works reasonably well. However, rapid changes in the current can still produce small amount of errors in the field profile due to skin effect, proximity effect and inter-winding capacitances. Although a helical coil geometry was considered in the simulations, the field was simulated only on the coronal plane by assuming angular invariance of the three-dimensional distribution due to the very low pitch angle of the coil elements. In the experiments, the z component of the magnetic field profile of each array element was measured based on the phase difference between a reference coronal gradient-echo (GRE) image and another GRE image with the same echo time and a small blip of current applied to the corresponding array element only during phase encoding. Field maps were obtained with a 1 mm x 1 mm spatial resolution. All experiments in this thesis were conducted using a 3 T scanner (Magnetom Trio A Tim, Siemens).

In Fig. 2.2, simulated and measured magnetic field profiles per unit current for the first five channels are shown. The measurements were performed on a smaller volume determined by the sensitivity of the RF coil. The measurement locations are indicated with red boxes on the simulated profiles. The mean percentage error over all pixels of all channels is 0.6%, and the RMS percentage error is 7%.

2.2.3 Example Optimized Field Profiles

A gradient array system enables dynamic optimization of the field profile with dynamically adaptable current weightings. A least squares optimization problem is formulated to solve the optimal current weightings for a given target magnetic field profile, as shown in Eq. 2.1:

$$\min_{\mathbf{I_w},\alpha} = \|\mathbf{B_{target}} - \alpha \mathbf{B}\mathbf{I_w}\|_2 \tag{2.1}$$

where $\mathbf{B_{target}}$ is a column vector consisting of a target magnetic field at discrete locations, $\mathbf{B}$ is a matrix with column vectors consisting of measured or simulated magnetic field profiles for a unit current applied to each channel, $\mathbf{I_w}$ is a column vector representing the current weightings of all channels with unit infinity norm and α is an arbitrary scaling factor. Although one can define many other optimization problems, this optimization problem is preferred for the current weightings in this example because it provides the minimum error norm as the simple analytical solution, as shown in Eq. 2.2:

$$\mathbf{I_w^*} = \frac{\mathbf{B}^+\mathbf{B_{target}}}{\|\mathbf{B}^+\mathbf{B_{target}}\|_\infty} \tag{2.2}$$

where $\mathbf{B}^+$ is the pseudoinverse of $\mathbf{B}$.

Three example current vectors optimized for different magnetic field distributions, such as a linear z-gradient ($B_z \propto z$), second-order Z2 ($B_z \propto z^2 - 0.5(x^2+y^2)$)

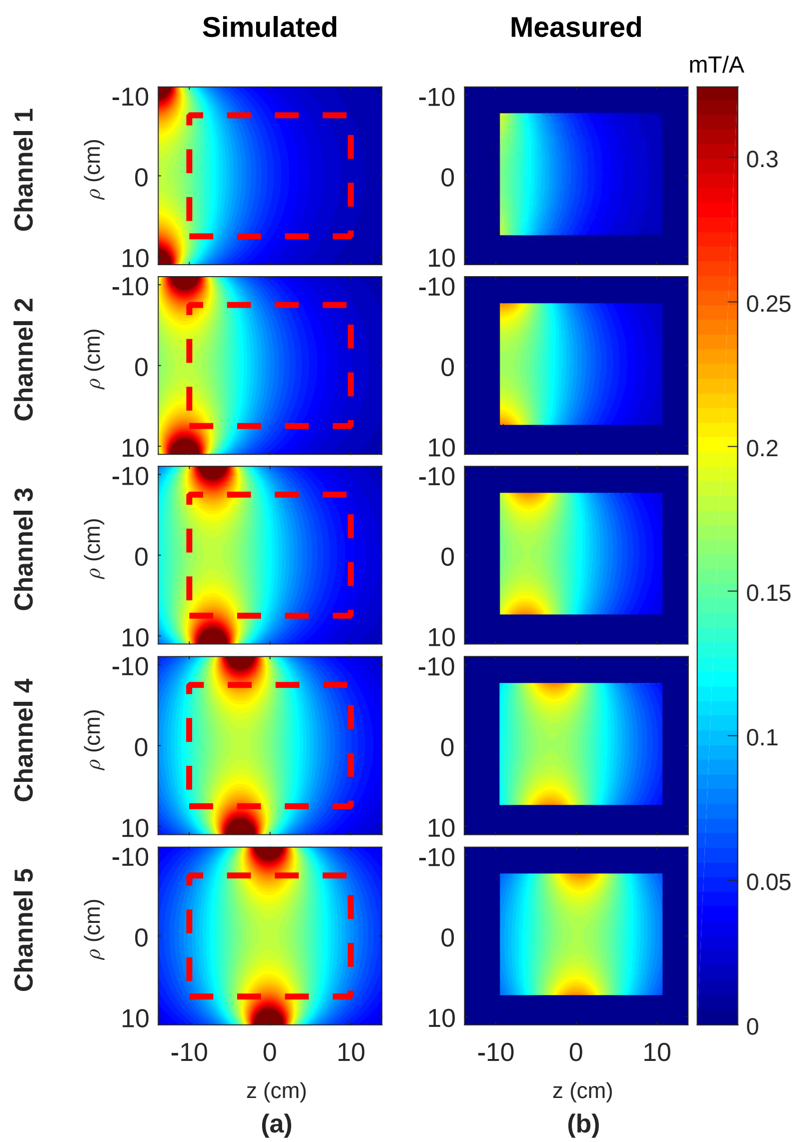

Figure 2.2: Magnetic field profiles for channels 1-5. Other channels are omitted due to symmetry and space considerations. **(a)** Simulated results for a cylindrical volume with a diameter of 22 cm and a length of 27.6 cm. The location of the phantom is indicated with a red box for ease of comparison. **(b)** Measured results, shown with a mask of 15 cm in diameter and 20 cm in length indicating the phantom boundaries.

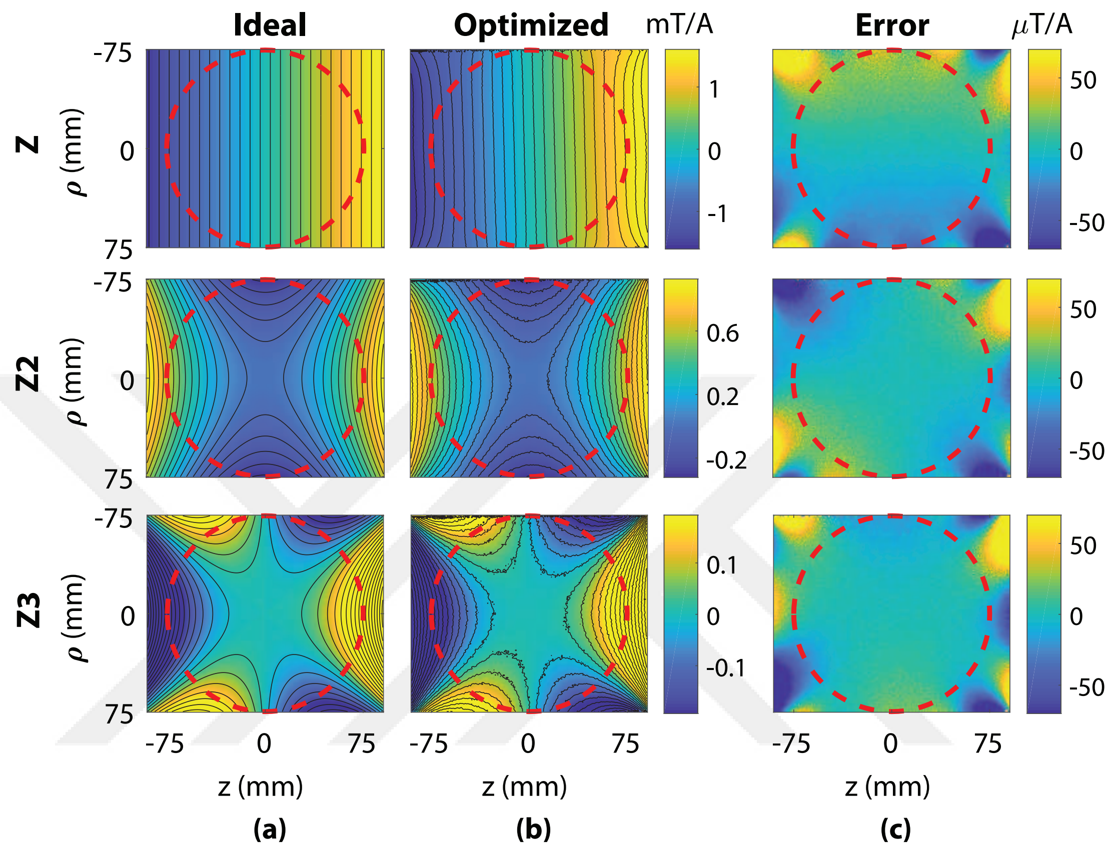

Figure 2.3: Magnetic field profiles for linear z-gradient ($B_z \propto z$), second-order Z2 ($B_z \propto z^2 - 0.5(x^2 + y^2)$) and third-order Z3 ($B_z \propto z^3 - 3z(x^2 + y^2)$) magnetic fields. **(row 1)** Target magnetic field profiles, **(row 2)** superposition of measured magnetic field profiles with optimized current weightings; that is, optimized field profiles and **(row 3)** error maps between the target and optimized magnetic field profiles. The red circle indicates the optimization box, which is a 15 cm DSV.

and third-order Z3 ($B_z \propto z^3 - 3z(x^2+y^2)$) fields inside a 15-cm-diameter spherical volume (DSV). All computations are performed in MATLAB 2017a (The MathWorks, Natick, MA). Magnetic field map measurements in Fig. 2.2 are used in the construction of $\mathbf{B}$ matrix construction.

The current weightings are optimized for three example magnetic field profiles, such as the Z, Z2 and Z3 fields, using Eq. 2.2. The optimal current weightings are scaled by 20 A assuming that maximum current limitation of the amplifiers are 20 A. The target magnetic fields and the obtained magnetic field profiles using the superposition of the previously measured magnetic field map of each channel

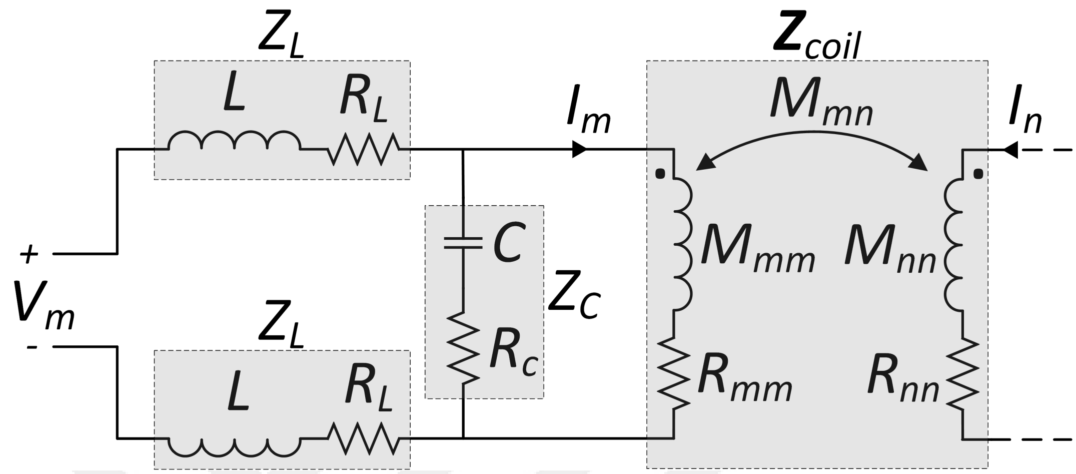

Figure 2.4: Circuit model for the single-stage LC gradient filters and mutually coupled gradient coils.

with optimized current weightings and error between the target and obtained magnetic field profiles are provided in Fig. 2.3. The optimized linear z-gradient field profile is also used as a readout gradient during the experiments.

2.3 Driving Mutually Coupled Gradient Coil Array

2.3.1 Circuit Model

Fig. 2.4 shows the LTI circuit model of the gradient coils and a single stage of the LC gradient filter, where ZL and ZC are the impedances of the series inductor and parallel capacitor of the filter, respectively. The impedance of the mutually coupled gradient coils is modeled by a series combination of a diagonal resistance matrix, **R**, and a mutual coupling matrix, **M**, in which the diagonal terms determine the self-inductance and the off-diagonal terms determine the inductive coupling between the channels [39]. The input and output characteristics of this model at a single frequency can be modeled as a multiple-input-multiple-output

(MIMO) system to account for cross couplings as in Eq. 2.3:

$$\mathbf{V}(\omega) = (\mathbf{Z_{coil}} + 2Z_L\mathbf{E} + \frac{Z_L}{Z_C}\mathbf{Z_{coil}})\mathbf{I}(\omega) \tag{2.3}$$

where $\mathbf{V}$ and $\mathbf{I}$ are the vectors for the input voltage and output current of all channels, and $\mathbf{E}$ is the identity matrix. $\mathbf{Z_{coil}}$ is the coil impedance matrix, which can be written as $\mathbf{Z_{coil}} = \mathbf{R} + j\omega\mathbf{M}$.

The output filter is designed to suppress the current ripple at the effective switching frequency of the amplifiers while having minimal influence at the band-pass frequencies. The capacitive term in Eq. 2.3 can be neglected in the low-pass regime, which leads to the definition of the first-order time domain relation between the input voltage and output current, as in Eq. 2.4. The first-order time domain expression in Eq. 2.4 is the equation that is used in the pulse width modulation (PWM) calculations throughout the study.

$$\mathbf{V(t)} = \mathbf{M_{total}}\frac{d\mathbf{I(t)}}{dt} + \mathbf{R_{total}}\mathbf{I}(t) \tag{2.4a}$$

$$\mathbf{M_{total}} = \mathbf{M} + 2Z_L\mathbf{E}\ \mathit{and}\ \mathbf{R_{total}} = \mathbf{R} + 2R_L\mathbf{E} \tag{2.4b}$$

2.3.2 Validation with Impedance Measurements

The lumped element circuit model assumes that the inductance, capacitance and resistance values are constant in the operating bandwidth of the amplifiers. However, gradient waveforms require high fidelity in the programmer's design. Therefore, the impedance of the filter components and gradient coils are measured as a function of frequency using a GW Instek LCR-B105G high-precision LCR meter (Good Will Instruments, Taiwan) for comparison with the low-frequency approximation of the lumped element circuit model.

First, the impedance of each channel is measured as a function of frequency when all other channels are open circuits. Another measurement is performed to calculate the cross-channel impedance, Z_{mn}. The impedance of the m^{th} channel is measured when the n^{th} channel is a short circuit, which is called Z'_{mn}. When measuring Z'_{mn}, the voltage induced on the m^{th} channel and current flowing through the m^{th} channel can be defined as V'_m and I'_m, respectively. The measurement of Z'_{mn} leads to two different equations at each frequency as follows:

$$\begin{bmatrix} V'_m \\ 0 \end{bmatrix} = \begin{bmatrix} Z_{mm} & Z_{mn} \\ Z_{mn} & Z_{nn} \end{bmatrix} \begin{bmatrix} I'_m \\ I'_n \end{bmatrix} \tag{2.5}$$

where I'_n is the current flowing through the n^{th} channel during the measurement. In this equation, Z_{mm} and Z_{nn} are known from previous self-impedance measurements. The ratio of V'_m and I'_m is already measured as Z'_{mn}. If simple algebraic steps are carried out, Z_{mn} can be calculated as follows:

$$Z_{mn} = \sqrt{Z_{nn}(Z_{mm} - Z'_{mn})} \tag{2.6}$$

with a phase ambiguity. This phase ambiguity can be resolved by imposing the constraint that the resistive part of the Z_{mn} should be positive. Z'_{mn} is measured for all 36 possible pairs of 9 channel array elements.

Impedance matrix is measured up to the operating bandwidth of the amplifiers ($\leq$10 kHz) with a 100 Hz step size. After calculating the $\mathbf{Z_{coil}}$, the impedances of the filter components are also measured to calculate the frequency response of the circuit, $V_m(\omega)/I_n(\omega)$, based on the impedance measurements according to Eq. 2.3.

Impedance measurements are performed to test the validity of the first-order lumped element circuit model in the low-pass frequency regime, which is expressed in Eq. 2.4. For the first-order circuit model, inductance values measured at 1 kHz are assumed to be valid over the entire frequency range, and the resistance values measured at DC are used in the entire bandwidth. The frequency response of the first-order lumped element circuit model and impedance measurements are compared in Fig. 2.5. An impedance matrix for 4 channels is shown, and similar characteristics are present for the other channels.

The impedance measurements can be used to analyze the assumptions made in Eq. 2.4. Each coil element is modeled as an inductance and a DC resistance by

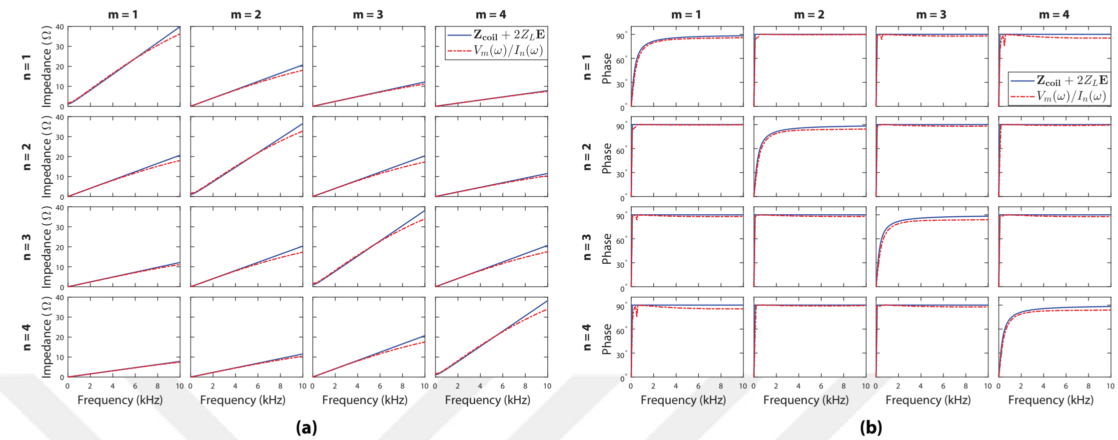

Figure 2.5: Impedance matrices are shown for **(blue)** the proposed circuit model in Eq. 2.4 assuming frequency-independent circuit elements and **(red)** the calculated ratio of the input voltage for the m^{th} channel and output gradient current for the n^{th} channel using impedance measurements of coil arrays with filters as a function of frequency. Both the **(a)** amplitude and **(b)** phase of the impedance matrices are shown.

assuming that (1) there is no AC resistance; and (2) the self-resonance frequency of the coil is at much higher frequencies than the operating bandwidth of the amplifiers; the effect of the filter capacitor in Eq. 2.3 is also neglected in Eq. 2.4. These assumptions lead to only a 1% deviation in the self-impedance on average at 5 kHz compared to the frequency response measurements. For frequencies greater than 5 kHz, the capacitive effects become notable, and the circuit model overestimates the self-impedance by nearly 12% for all channels at 10 kHz. The average phase error of the self-impedance is 4° at 10 kHz, which originates mostly from the increase in the AC resistance of the coil. Moreover, the circuit model also underestimates the amplitude of the mutual impedances at frequencies higher than 5 kHz due to capacitive effects. The average phase of the mutual coupling between any channel and the closest neighbor is 88° at 10 kHz, probably due to resistive coupling between the channels. Therefore, the purely inductive mutual coupling assumption in Eq. 2.4 causes a 2° phase error in the frequency response of the cross terms.

The impedance measurements of the self-impedance and mutual impedance of the coil alone are in good agreement with the model in which each coil is

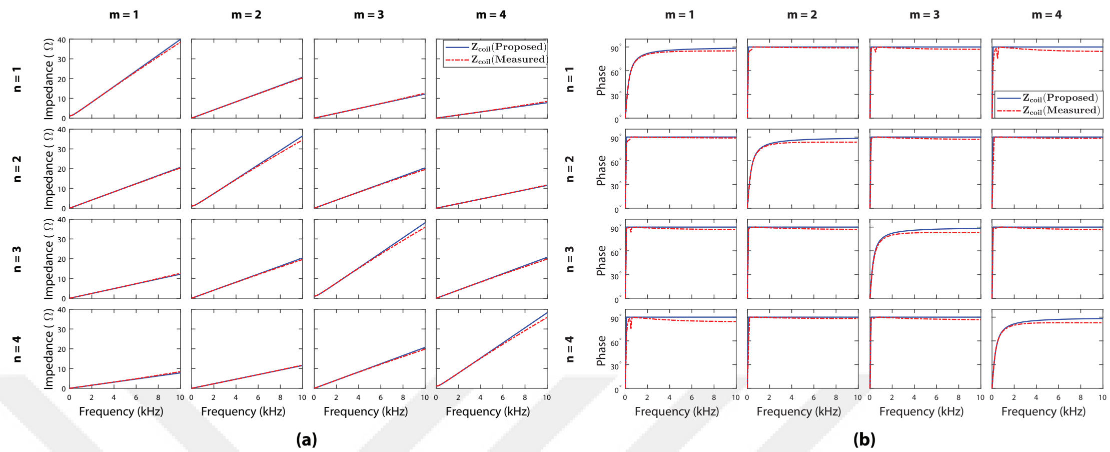

Figure 2.6: Impedance matrices are shown for **(blue)** the proposed circuit model for the gradient array coils without filters assuming frequency independent circuit elements and **(red)** measured self and mutual impedances using impedance meter measurements as a function of frequency. Both **(a)** amplitude and **(b)** phase of the impedance matrices are shown.

represented by a series RL circuit and inductively coupled with other series RL circuits as shown in Fig. 2.6. Although these results are specific to our custom-designed z-gradient array coil, the technique is proposed for general gradient coil arrays based on the fact that the self-resonance frequency of the gradient coils is designed to be much higher than the switching frequency of the amplifiers. However, the frequency response between the amplifier's output voltage and the coil current can be affected by the capacitive components of the gradient filter. Filter effects are apparent toward the end of the bandwidth, which generally contains lower power. Furthermore, higher-order filters can be designed with sharper frequency responses to be transparent in the operating bandwidth of the coil currents while providing enough suppression at the switching frequency [45,46]. In this study, a first-order filter is preferred to avoid a further increase in the complexity of the hardware. Higher-order filters might increase the physical space requirements, power dissipation and cost of the hardware.

2.3.3 Minimum Rise Time Calculations

In a mutually coupled array configuration, the maximum amplifier voltage and impedance of a single channel are not sufficient to determine the rise time for a given current value. Current flowing through each coil is highly affected by the currents flowing through the other coils, especially neighboring coils with strong coupling. Therefore, the rise times and resulting slew rates should be calculated for each current amplitude and timing. For a particular time dependence of a fixed magnetic profile, all coils should be driven by currents with different amplitudes but exactly the same time dependence. In the case of a typical trapezoidal current with equal rise and fall times, the peak voltage is required either at the end of the rise period or the beginning of the fall period. If the voltage limitations of the amplifiers are identical for each channel, there is a lower bound on the rise time determined by the coil with the highest peak voltage, which should be driven by the maximum voltage limitation of the amplifiers. Considering Eq. 2.4a, the minimum possible rise time for a trapezoidal time dependence of any magnetic field profile can be calculated as follows:

$$\Delta t_{min} = \max_{1 \leq m \leq N} \left\{ \frac{\left| \sum_{n=1}^{N} M_{mn} \cdot I_n \right|}{V_{max} - |R_{mm} \cdot I_m|} \right\} \tag{2.7}$$

where Δt_{min} is the minimum rise time, I_n is the current amplitude of the n^{th} channel during the plateau period of the trapezoidal waveform, M_{mn} is the mutual inductance between the m^{th} channel and nth channel, R_{mm} is the resistance of the m^{th} channel and V_{max} is the maximum voltage limitation of the identical amplifiers.

Since the first-order model overestimates the impedance of the system as in Fig. 2.5, the channel voltages in Eq. 2.4 and minimum rise time in Eq. 2.7 are also overestimated. Therefore, neglecting the capacitive effects in analytical models does not pose a risk of exceeding the amplifier voltage limitations.

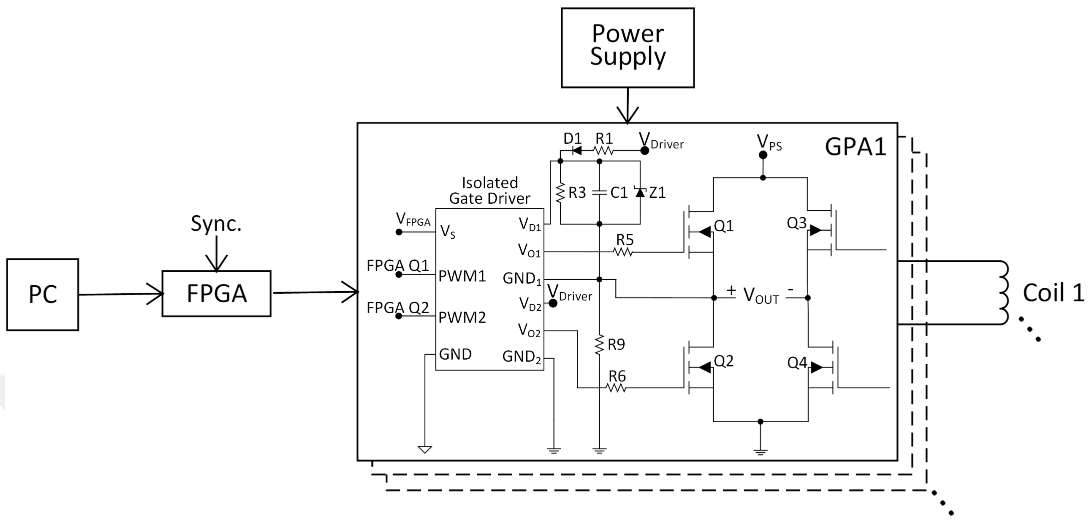

Figure 2.7: Schematic illustration of the full H-bridge gradient amplifier array (periphery components of the right side are not shown here), including a single power supply, its gate drivers, control signals provided by an FPGA and gradient coils as loads.

2.3.4 Driver System

Gradient array systems consist of multiple coils driven by individual amplifiers. In this thesis, desired current waveforms are supplied using a home-built 9 channel gradient amplifier array. Significant portion of the design of GPAs are previously designed in a M.S thesis [15]. During the experiments of this thesis, design of the GPAs are slightly reconsidered. User interface to program the GPAs are developed continuously during this thesis with the help of Hamed Mohammadi.

Overall system is also described in this thesis to ensure completeness of the hardware. Fig. 2.7 depicts the main components of the proposed gradient amplifier array setup. Each gradient power amplifier is employed in a one-stage H-bridge configuration, and a bootstrap circuit is used to drive the high side switches. An isolated gate driver (ADuM7234, Analog Devices, Massachusetts, USA) is used to switch NMOS transistors (IRFP250n, Infineon Technologies Americas Corp., California, USA), providing 50 V and 20 A at the output. A single power supply is used to feed all the GPAs, since each GPA consists of a

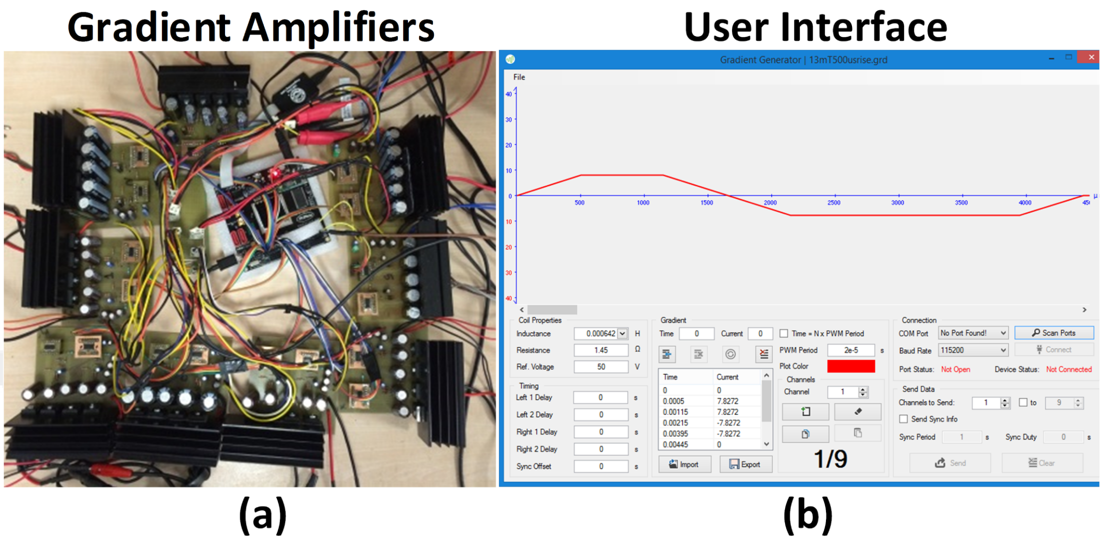

Figure 2.8: **(a)** Nine gradient amplifiers and an FPGA, **(b)** user interface to program the waveforms for all channels.

single-stage H-bridge rather than a conventional stack configuration [47]. Images of the home-built GPAs are shown in Fig. 2.8a.

The evaluation board of a Xilinx Virtex5 FPGA (XMF5, PLDkit OU) with a 100 MHz clock frequency is used to generate the PWM control signals. The PWM period is chosen as 20 μs, which leads to a 10 μs dwell time and a 100 kHz effective PWM frequency for the center-aligned PWM configuration. Considering the clock frequency, the duty cycles can be set approximately with 10 bits of resolution for all channels independently. The FPGA is programmed by a user interface in a PC via serial communication. The user interface allows programming of the channel impedance, desired current waveforms, PWM delays to prevent shoot through in the H-bridge circuitry, supply voltage, and PWM periods independently for an arbitrary number of channels. A screenshot of the user interface is provided in Fig. 2.8b.

2.3.5 Current Measurements

The PWM signals are generated based on the lumped element circuit model in Eq. 2.4. Although full mutual impedance matrix measurements of the 9-channel coil are available, self-inductances and resistances are tuned manually to include the effect of the feed cables and amplifier-related parameters, such as stray inductances and drain sources, on the resistance of the MOSFETs. Currents flowing through nine coil elements are captured for the example cases to demonstrate the effect and feasibility of compensating for the mutual coupling between channels in the bench-top experiments. Current measurements are performed outside of the MRI scanner using a current probe (LFR06/6 Rogowski Current Waveform Transducer, Power Electronic Measurements Ltd., Nottingham, UK) and a digital oscilloscope (Agilent DSOS104A, Keysight Technologies, California, USA). Current waveforms are digitized at a rate of 2 MSa/s to filter out the higher-frequency interference signals in the environment.

In highly coupled gradient array coils, the actual current waveforms might significantly deviate from the desired current waveform if mutual coupling is not compensated during the voltage calculations. The current error might be in different forms depending on the individual current amplitudes and waveforms for the mutually coupled coils, as illustrated in Fig. 2.9. When the self-inductances of two coils are comparable and the mutual coupling coefficient is positive, the current flowing in the same direction, depending on their amplitudes, might lead to an undershoot and increase the rise time of the desired current for both channels because of the opposing induced voltage (Fig. 2.9a). Similarly, reverse directed currents flowing in the two coils can cause an overcurrent in both channels (Fig. 2.9b). Moreover, even the direction of the current might change from the desired current direction if the induced voltage is greater than the applied voltage (Fig. 2.9c). In particular, the current waveforms of channels with relatively lower desired current values might be significantly influenced by the channels with higher current values, as shown in Fig. 2.9c. When the mutual coupling is considered as in Eq. 2.4, desired current waveforms can be achieved with significantly less error.

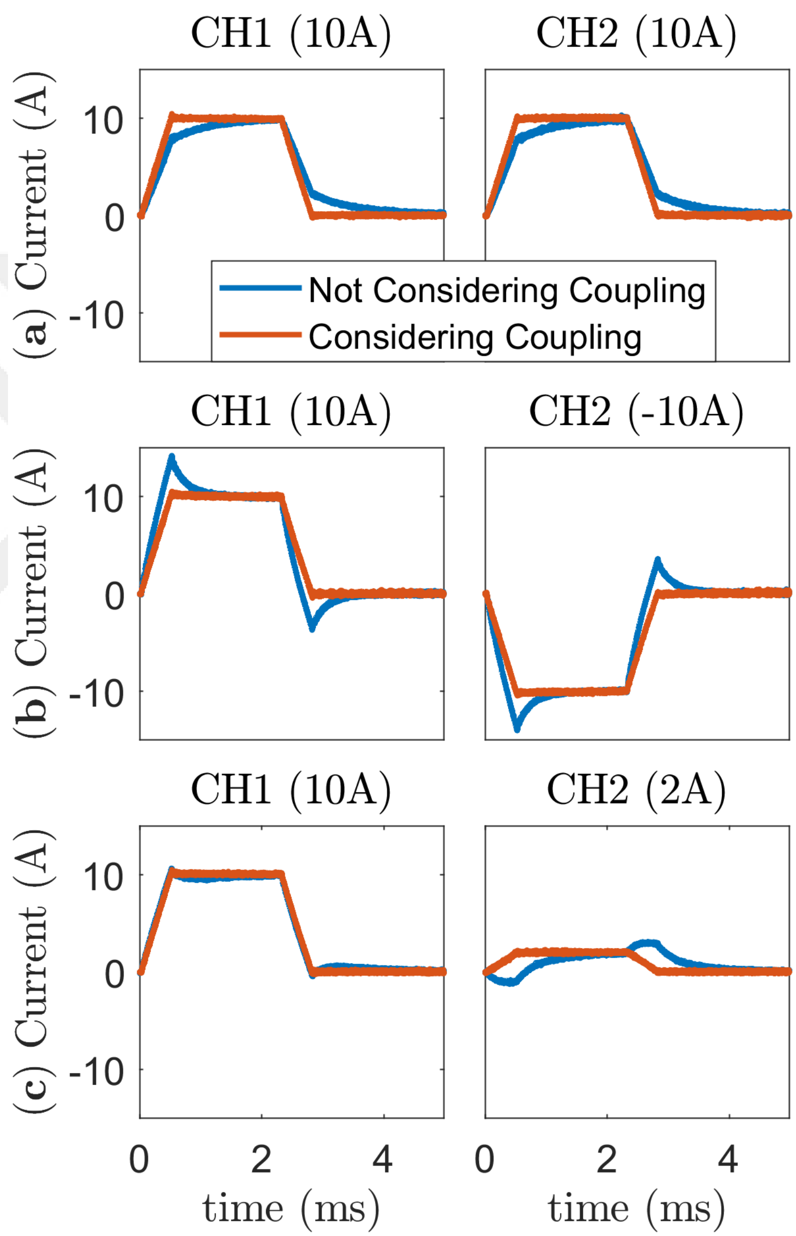

Figure 2.9: Current measurements of two channels when mutual coupling is or is not compensated during the input voltage calculations. Three example current pairs are demonstrated for Ch1 and Ch2 as **(a)** 10 A and 10 A, **(b)** 10 A and -10 A and **(c)** 10 A and 2 A.

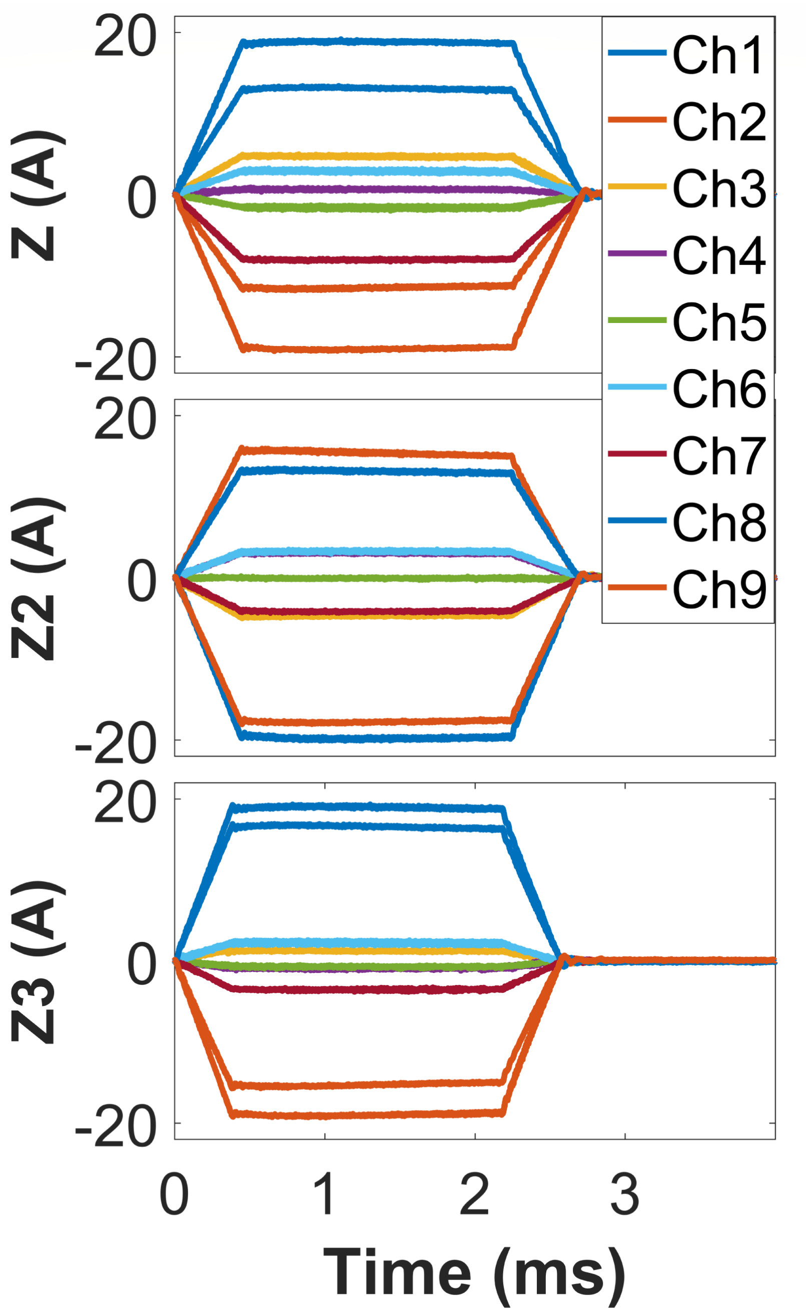

Figure 2.10: Current measurements of nine channels for the Z, Z2 and Z3 field profiles. Trapezoidal current waveforms with analytically calculated minimum rise times are applied to all channels simultaneously.

Furthermore, the minimum attainable rise times for the optimized current vectors are calculated using Eq. 2.7as 450 μs, 440 μs and 380 μs for the Z, Z2 and Z3 fields in Fig. 2.3, respectively. The user interface of the gradient amplifiers is programmed to provide trapezoidal current waveforms with minimum rise times. Fig. 2.10 shows the measured current waveforms passing through all gradient channels for the three field profiles. Small current drops were observed in the plateau region of some of the trapezoidal waveforms, most likely because of the supply voltage drops during high-demand use and the fact that there is no feedback loop in the amplifiers to compensate for the current values. However, all current waveforms increased to the desired value in the minimum possible rise time, which confirms the circuit model in Eq. 2.4 and the analytical expression in Eq. 2.7.

2.4 Validation with MRI Experiments

Furthermore, MRI experiments are conducted to image an orange as well as a home-built, homogeneous cylindrical phantom with a diameter of 10 cm that consists of CuSo4 solution at a concentration of 15 mM/L. Central coronal slices are imaged using a GRE sequence with an FOV of 150 mm, an isotropic in-slice resolution of 1 mm and a slice thickness of 5 mm. For the orange and phantom images, the TE/TR values are 10/100 ms and 7/300 ms, respectively. During the experiments, the system z-gradients are turned off. Coil elements with current weightings optimized for a linear z-gradient with a gradient strength of 13 mT/m are used as the prephaser and readout gradients. The prephaser and readout gradients take a total of 1150 μs and 2300 μs, respectively, including the rise and fall times of 500 μs. The maximum gradient amplifier voltage is limited to 40 V, and 80% of the actual specification of the amplifier increases the reliability of the system.

Fig. 2.11 shows a comparison of the coronal MRI images acquired using a conventional z-gradient system and the z-gradient generated by the array system. There are no significant spatial distortions in the images of the cylindrical

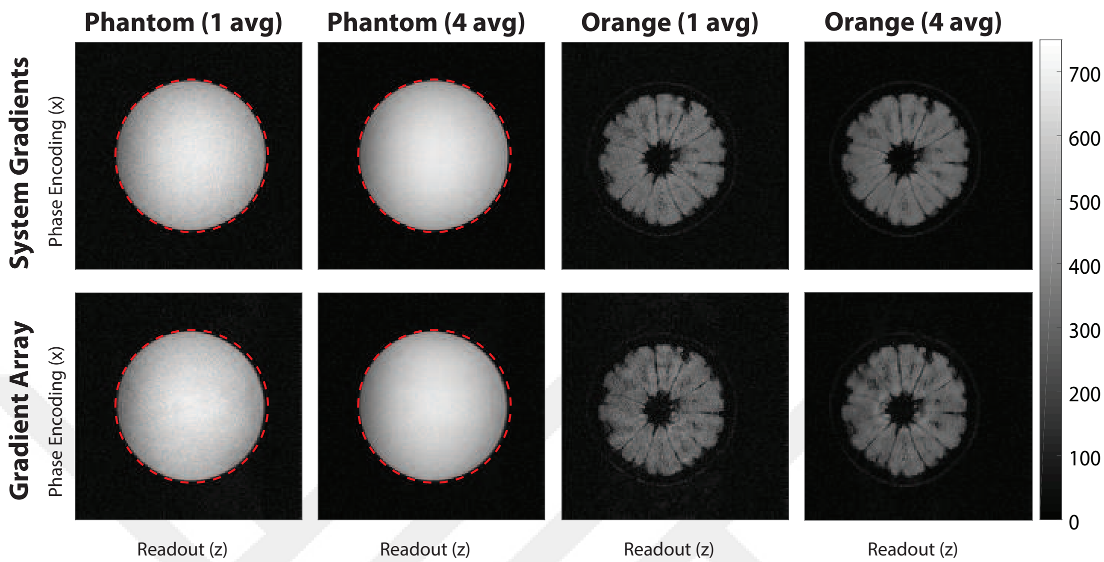

Figure 2.11: Coronal MRI images of a cylindrical phantom and an orange with 1 and 4 averages. **(row1)** The system z-gradient and **(row2)** gradient array system is used as the readout gradient for comparison. The fixed red circles indicate the boundaries of the phantom.

phantom, which validates two claims. First, the linearity of the magnetic field generated by the array system is comparable to the linearity of the conventional gradient coil. Second, the desired gradient amplitude is achieved during readout, since the dimensions of the phantoms are almost identical. Additionally, both the phantom and orange are imaged using an averaging factor of four to test the repeatability of the experiments and increase the SNR of the images. The agreement between the images taken with the system gradients and the gradient array can be considered as a proof of concept for the high time fidelity of the gradient currents, which validates the proposed method for driving mutually coupled array coils. Furthermore, using a gradient array system as a readout gradient results in some artifacts in the phase encoding direction, which can be visually inspected in Fig. 2.11.

2.5 Discussion

2.5.1 Practical Comments on the Z-Gradient Coil Array

In this thesis, home-built nine channel z-gradient array is designed and manufactured. This array of coils is only a basic prototype to demonstrate proof of concept studies; therefore, it lacks some significant practical features which are necessary in the clinical application. First of all, the coil array is only air cooled in contrast to water cooling system of conventional gradient coils. Due to the lack of a professional cooling system, high duty cycle gradient currents might cause overheating the coil. Overheating of the coils might result decrease in the current flowing through the coil due to increased resistance or even damage the coil windings. Second, although our coil array is not shielded, eddy current effects are negligible due to the small radius of the coils. For especially, larger human size gradient array coils, each element can be designed to be self-shielded [41] or a shield can be designed as an array of coils driven by independent amplifiers. Lastly, mechanical stability of the coil can be improved. Theoretically, magnetic moment of each loop in the z-gradient array is parallel with the main magnetic field; therefore, no torque is expected on the coil. However, since it is home-built and placement of the coil inside the MRI scanner has been done manually, torque can be induced on the coil. Similar to torque, force also can be induced on the wires. As a result, there might be some vibrations of the coil due to the coil depending on how fast the current waveforms are switched. As a remedy, mechanical properties of this coil should be reconsidered for a human size conventional z-gradient array.

2.5.2 Effect of the Gradient Filter

The impedance measurements of the self-impedance and mutual impedance of the coil alone are in good agreement with the model in which each coil is represented by a series RL circuit and inductively coupled with other series RL circuits (see

Fig. 2.6). Although these results are specific to our custom-designed z-gradient array coil, the technique is proposed for general gradient coil arrays based on the fact that the self-resonance frequency of the gradient coils is designed to be much higher than the switching frequency of the amplifiers. However, the frequency response between the amplifier's output voltage and the coil current can be affected by the capacitive components of the gradient filter. Since the first-order model overestimates the impedance of the system as in Fig. 2.5), the channel voltages in Eq. 2.4 and the minimum rise time in Eq. 2.7 are also overestimated. Therefore, neglecting the capacitive effects in analytical models does not pose a risk of exceeding the amplifier voltage limitations. Filter effects are apparent toward the end of the bandwidth, which generally contains lower power. Furthermore, higher-order filters can be designed with sharper frequency responses to be transparent in the operating bandwidth of the coil currents while providing enough suppression at the switching frequency [46, 47]. In this study, a first-order filter is preferred to avoid a further increase in the complexity of the hardware. Higher-order filters might increase the physical space requirements, power dissipation and cost of the hardware.

2.5.3 Feedback Requirements

In this study, the gradient array system is modeled as an LTI system. Although this model provides currents to the coils with adequate accuracy to perform the imaging, nonlinear effects such as thermal effects, power source and amplifier imperfections can still degrade the time fidelity of the coil currents [42]. Therefore, a closed loop feedback system might be required to compensate for the residual current errors. The design of the current controller for the mutually coupled coil arrays might require multivariable feedback control [48] because of the cross-talk between the channels, which requires further investigation. The first-order model in combination with a single-input-single-output (SISO) feedback loop might still provide the desired waveforms with lower computational complexity as an alternative to a full frequency response correction of the system [42, 44].

2.5.4 Eddy Current Compensation

The proposed model is very similar to the conventional eddy current compensation method, which assumes multiple couplings between the conductive surfaces and the gradient coil [49]. Eddy current compensation can be trivially included in the proposed method, accounting for the couplings with both passive eddy current surfaces and other actively driven gradient coils. Moreover, there are some programmable pre-emphasis systems that can adapt the pre-emphasis coefficient dynamically [50], which can be adapted for mutual coupling compensation dynamically as part of the spectrometer.

2.5.5 Hardware Perspective

Significant voltages can be induced on the loads due to the high change rate of the currents in the neighboring channels. Therefore, voltage isolation of the amplifier components should be considered at the design stage to ensure that no component is at risk during the worst-case coupling scenarios. As another extreme case, induced voltages might even exceed the supply voltage of the amplifiers, which might cause some unexpected current flow through the freewheeling diodes of the transistors. Furthermore, the malfunctioning of an amplifier might also damage the other amplifiers due to coupling; therefore, the safety precautions should also consider the mutual coupling between channels by monitoring the current and voltage of all amplifiers.

Although extreme couplings might be troubling in terms of the amplifier, mutual coupling might be utilized to decrease undesired current ripples originating from the switching voltages. Multistage H-bridge amplifiers can accompany phase-shifted PWM schemes [51] to increase the effective switching frequency, which results in reduced current ripples. Single-stage amplifiers cannot increase the effective switching frequency in their normal operation mode, and optimized relative phases for the PWM signals of the amplifiers along with their mutually coupled loads can decrease the energy of the current ripples by more than 90%

in some cases [52]. The PWM phase shifting strategy can be used together with gradient filters to further reduce the current ripples [53]. The advantage provided by the relative phases of the PWM control signals for an amplifier array might also be exchanged for simpler gradient filters with lower series inductance, smaller physical size, lower power dissipation or lower phase delays.

2.5.6 Shimming Applications

Previously, it was demonstrated that nonorthogonal field profiles can overcome conventional orthogonal spherical harmonic fields for dynamic shimming purposes using a high number of shim array coils [54–57] or RF coils as shim coils with dedicated hardware [58, 59]. Although the gradient field demands in terms of switching rates and field amplitudes are higher than in shim coils, the effect of mutual coupling can still affect the shimming performance of shim coil arrays. More importantly, shim coil arrays are generally used simultaneously with conventional linear gradients, which might induce undesired currents in the shim coils due to mutual coupling between the system gradients and shim arrays. Moreover, shim coil arrays can also generate linear gradient profiles [40] and can be used for combined imaging and shimming applications [60]. In this case, mutual coupling should also be considered, because the shim array current should be switched at faster rates for imaging purposes.

2.5.7 Mutual Coupling Considerations During the Coil Design

Nonorthogonal field profiles generated by arbitrary coil geometries are likely to cause mutual coupling between the channels. Mutual coupling might be reduced in the design stage by physically shifting the coil elements [41]. Coil arrays can also be designed by constraining the field orthogonality of the channels; however, discretization of the surface currents might still cause some residual mutual coupling [43]. For both strategies, the aim of avoiding mutual coupling results in more constraints and fewer degrees of freedom in the system design. Furthermore, coil manufacturing, the scarcity of available space on the coil surfaces, the feed cables of the coils and the high number of coil elements can still cause mutual coupling even if it is avoided in the design process. Therefore, the proposed method of modeling and controlling the mutual coupling of gradient array systems might be preferable.

2.5.8 Field Design Flexibility

Driving each coil element independently enables dynamic gradient design. For conventional gradients, design parameters such as volume of VOI, gradient linearity, gradient strength, and the inductance of the coils are specified during the design stage and cannot be changed after manufacturing the coils. In contrast, some tradeoffs between the design parameters can be dynamically utilized depending on the target volumes and imaging sequences for array systems. The proposed formulation in Eq. 2.7 can be included in the optimization problems for better utilization of hardware slew rate limits (i.e., voltage ratings) in exchange for sacrificing other field parameters. However, physiological slew rate limits due to peripheral nerve stimulation (PNS) are still an open question for gradient coil arrays because the vector E-field distribution generated by each element is dynamically superposed when coil currents are dynamically changing. Therefore, the proposed study enables the analysis and optimization of the slew rate limits in terms of hardware capabilities, while physiological slew rate limits require further investigation.

As a result, z-gradient array prototype are used for proof of concept studies; however, further investigations are required to fully adapt this technology to the clinical scanners.

Chapter 3

Dynamic Optimization of Gradient Field Performance Using a Z-Gradient Array

3.1 Introduction

Conventional gradient coils are designed to satisfy some performance parameters such as size of the linearity volume, linearity error, inductance, power dissipation, gradient strength per unit current [1]. As an example tradeoff, there is an inverse relation between the size of the gradient VOI and PNS thresholds [61]. Another example is the increased efficiency of insert gradient coils compared to whole body gradient coils [62] due to their smaller linearity volume.

Although different applications might require different target volumes and gradient performance metrics, performance of the conventional coils cannot be altered after manufacturing. On the contrary, gradient array coils driven by independent amplifiers can generate flexible field profiles dynamically. Available types of the gradient field with varying performance parameters might affect the image SNR, post-processing requirements, scan time, power dissipation and PNS

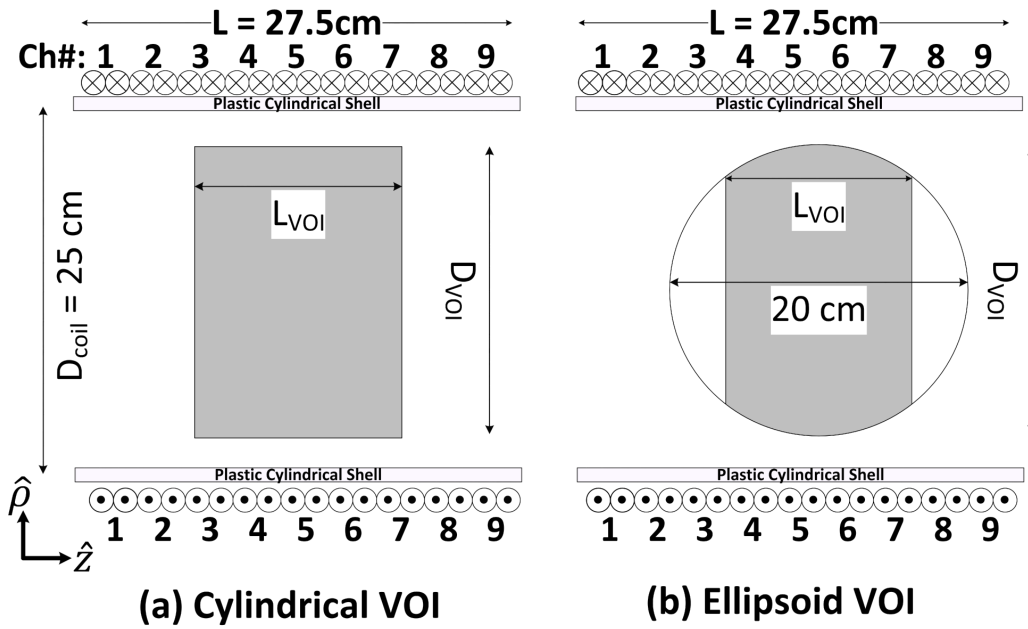

Figure 3.1: Illustration of nine channel z-gradient array (diameter = 25 cm, total length = 27.5 cm), **(a)** cylindrical VOI with free parameters of length (L_{VOI}) and diameter (D_{VOI}) of cylinder and **(b)** Ellipsoid VOI with longitudinal diameter of 20 cm and transversal diameter of D_{VOI} is truncated in z-direction with length of L_{VOI}.

thresholds. In this study, nine channel z-gradient array in Chapter 2 is used to optimize various cost functions: (1) minimum linearity error, (2) maximum gradient strength, (3) maximum hardware slew rate, (4) current norm and (5) maximum vector B-field for VOIs with different sizes. Gradient array's capability to dynamically optimize the field profiles and performance metrics are shown with simulations.

3.2 Methods

Gradient array performances are analyzed and optimized for two types of volume of interest such as cylindrical and truncated ellipsoid volumes with free parameters of length (L_{VOI}) and transverse diameter (D_{VOI}) of VOI as shown in Fig. 3.1a and Fig. 3.1b respectively.

5 different optimization problems are defined to measure the performance metrics of the z-gradient array. For all of the optimization problems, peak value of the gradient linearity error over the entire VOI, α, is defined as follows:

$$\alpha = \max_{\rho,z} \left| \frac{G_z(\rho,z) - G_z(0,0)}{G_z(0,0)} \right| \tag{3.1}$$

where $G_z(\rho,z)$ is the gradient strength at a specific location and $G_z(0,0)$ is the gradient strength at the center. In all of the optimization problems in this section, time dependency of the gradient fields and currents are not considered assuming that gradient fields are spatiotemporally separable.

3.2.1 Minimum Peak Linearity Error

Nonlinearity in gradient fields might result in undesired encoding of the object and image artifacts. Even in basic sequences, gradient nonlinearity cause variations in the voxel size. Although there are post-processing algorithms to homogenize the image resolution [63, 64], SNR becomes nonuniform on the image after these algorithms. In the excitation part, gradient nonlinearity can cause excitation of curved slices which is more challenging to correct in the post-processing stage. Therefore, gradient linearity is a desirable parameter inside the VOI for most of the conventional sequences. However, some gradient linearity might be sacrificed to gain performance advantage from other parameters. Dynamically arranging the gradient linearity enables to optimize the tradeoff between gradient linearity and other gradient performance metrics depending on the sequence requirements.

When gradient strength at the center is defined as unity, the denominator in Eq. 3.1 can be removed. Since *alpha* is independent of the scaling of **I**, this algebraic manipulation can be performed without loss of generality. A linear programming problem can be formulated to minimize the α inside the VOI as in Eq. 3.2:

$$\begin{aligned} &\min_{\mathbf{I}} \left\| \mathbf{G}^T\mathbf{I} - \mathbf{1} \right\|_\infty \\ &\mathbf{G}_{cent}^T\mathbf{I} = 1 \end{aligned} \tag{3.2}$$

where **I** is the column vector of coil currents, **1** is a column vector of ones, **G** is a matrix of normalized gradient strength with at N observation point for 9 channel with dimension of $9 \times N$ and $\mathbf{G}_{cent}$ is the column vector for the normalized gradient strength at the center for unit coil currents. Both $\mathbf{G}$ and $\mathbf{G}_{cent}$ are normalized with same normalization factor such that their infinity norm is 1. $\mathbf{G}_{cent}^T\mathbf{I}$ is the summation of gradient strengths provided by each channel at the center weighted by the current vector and similarly $\mathbf{G}^T\mathbf{I}$ is the summation of gradient strengths provided by each channel at N observation point weighted by the current vector.

This optimization problem is designed to be consistent with the definition of α by assuming that gradient strength at the center is unity since scaling of $\mathbf{I}$ does not influence the α. Optimization problem of minimizing the infinity norm with linear constraints can be expressed as in Eq. 3.3 with inserting a dummy variable ϵ. Since optimization problem aims to minimize the peak linearity error at all pixels, same optimization problem can be converted to minimization of the dummy variable that acts as an upper bound for linearity error. Therefore, more conventional structure of a linear programming problem can be obtained.

$$\begin{aligned} &\min_{\mathbf{I},\epsilon} \epsilon \\ &\left\|\mathbf{G}^T\mathbf{I} - \mathbf{1}\right\|_\infty \leq \epsilon \\ &\mathbf{G}_{cent}^T\mathbf{I} = 1 \end{aligned} \tag{3.3}$$

From Eq. 3.3, new set of variables and constraints can be defined to define an appropriate linear programming problem as in Eq. 3.4. Inequality constraint is reordered to get rid of the absolute value and to obtain a proper inequality constraint.

$$\begin{aligned} &\min_{\mathbf{I},\epsilon} \begin{bmatrix} \mathbf{0} & 1 \end{bmatrix} \begin{bmatrix} \mathbf{I} \\ \epsilon \end{bmatrix} \\ &\begin{bmatrix} \mathbf{G}^T & -\mathbf{1} \\ -\mathbf{G}^T & -\mathbf{1} \end{bmatrix} \begin{bmatrix} \mathbf{I} \\ \epsilon \end{bmatrix} \leq \begin{bmatrix} \mathbf{1} \\ -\mathbf{1} \end{bmatrix} \\ &\begin{bmatrix} \mathbf{G}_{cent}^T & 0 \end{bmatrix} \begin{bmatrix} \mathbf{I} \\ \epsilon \end{bmatrix} = 1 \end{aligned} \tag{3.4}$$

3.2.2 Maximum Gradient Strength

Higher gradient strengths are generally desirable in MRI since it can provide higher phase or frequency variation throughout the object. They might be used for increased image resolution, decreased scan time, decreased RF pulse durations, decreased TE, robustness to some image artifacts such as B_0 inhomogeneity and motion artifacts.

Another linear programming problem is defined to maximize the gradient strength at the center of the VOI while constraining the α with α_0 over entire VOI for a unit amplifier current.

$$\begin{aligned} &\min_{\mathbf{I}} -\mathbf{G}_{cent}^T\mathbf{I} \\ &\begin{bmatrix} (1-\alpha_0)\mathbf{1}\mathbf{G}_{cent}^T - G^T \\ \mathbf{G}^T - (1+\alpha_0)\mathbf{1}\mathbf{G}_{cent}^T \end{bmatrix} \mathbf{I} \leq 0 \\ &\|\mathbf{I}\|_\infty \leq 1 \end{aligned} \tag{3.5}$$

3.2.3 Maximum Slew Rate

Slew rate limits are generally determined by amplifier voltage limitations and PNS due to fast gradient switching. In this section, hardware slew rate limits are studied. High slew rates are desirable in MRI especially. Most important example is that echo-spacing in echo planar imaging (EPI) is generally determined by the slew rate limits of the gradient system. Lower echo spacing decreases time interval for each echo which provides decreased TE as well as increased robustness to B_0 inhomogeneity and patient motion. For a required gradient strength, slew rate can be maximized by minimizing the rise time of the current vector. Rise time of a gradient coil current is limited by the amplifier voltage. In an array configuration, a channel with maximum voltage demand determines the minimum attainable rise for the same gradient waveform for all channels except the amplitude of the waveform.

In this optimization problem coil resistances are ignored for simplicity since peak voltage required for the gradient coils are generally dominated by the inductive part of the impedance. Therefore required coil voltage vector of each channel for a given current amplitude vector, rise time (Δt) and mutual coupling matrix, M, can be expressed as $\mathbf{V} = \mathbf{MI}/\Delta t$. Therefore, optimization problem is formulated to minimize the maximum value of the rise time among the channels for a given current vector (Eq. 2.7) for a unit amplifier voltage and a unit gradient strength at the center. Peak linearity error is also limited by α_0.

$$
\begin{aligned}
&\min_{\mathbf{I}} \Delta t_{min} = \min_{\mathbf{I}} \|\mathbf{MI}\|_\infty \\
&\left|(\mathbf{G}^T - \mathbf{1G}^T_{cent})\mathbf{I}\right| \leq \alpha_0 \left|\mathbf{1G}^T_{cent}\mathbf{I}\right| \\
&\mathbf{G}^T_{cent}\mathbf{I} = 1
\end{aligned}
\tag{3.6}
$$

The optimization problem in Eq. 3.6 is also converted to a formal linear programming problem similar to the minimum linearity error by inserting a dummy variable Δt_{min} as follows

$$
\begin{aligned}
&\min_{\mathbf{I},\Delta t_{min}} \begin{bmatrix} \mathbf{0} & 1 \end{bmatrix} \begin{bmatrix} \mathbf{I} \\ \Delta t_{min} \end{bmatrix} \\
&\begin{bmatrix} \begin{bmatrix} (1-\alpha_0)\mathbf{1G}^T_{cent} - \mathbf{G}^T \\ \mathbf{G}^T - (1+\alpha_0)\mathbf{1G}^T_{cent} \end{bmatrix} & \mathbf{0} \\ \mathbf{M}_{9\times 9} & -\mathbf{1} \\ -\mathbf{M}_{9\times 9} & -\mathbf{1} \end{bmatrix} \begin{bmatrix} \mathbf{I} \\ \Delta t_{min} \end{bmatrix} \leq \mathbf{0} \\
&\begin{bmatrix} \mathbf{G}^T_{cent} & 1 \end{bmatrix} \begin{bmatrix} \mathbf{I} \\ \Delta t_{min} \end{bmatrix} = 1
\end{aligned}
\tag{3.7}
$$

3.2.4 Minimum Current Norm

Conventional gradient coils are generally water cooled which requires strong cooling system. Coil temperature can still vary depending on the duty cycle and amplitude of the gradient coils despite the cooling system. There are efforts to reduce and optimize the gradient coil temperature [65] to avoid increase in the resistance to protect the gradient coil as well as to maintain the time dependency of the desired gradient waveform. Resistive power dissipated on the coil is one of the possible causes of increased temperature. Sometimes, it might be preferable to decrease the power loss on the coil by sacrificing some other gradient performance parameters. Surely, gradient strength can be used to decrease the power dissipation; however, it might no be preferable in some cases due to decreased imaging performance. Therefore, dynamic optimization of power dissipation for a unit gradient strength can be used to protect the overheating the coil. In an array of identical coils similar to our prototype, DC resistance matrix can be ignored and square of the current norm becomes directly proportional to power dissipation. Moreover, decreased current norm might also result in less mechanical stress on the coil and less acoustic noise depending on the geometry due to less induced force; although relation between them is not direct.

Square of the current norm is minimized for a unit gradient strength by also limiting the peak linearity error with α_0. Convex quadratic programming problem to minimize the current norm is formulated in Eq. 3.8. A resistance matrix, **R**, may also be inserted in the optimization problem to minimize the power dissipation for an arbitrary set of coils without complicating the optimization problem.

$$\begin{aligned} &\min_{\mathbf{I}} \|\mathbf{I}\|_2^2 \\ &\begin{bmatrix} (1-\alpha_0)\mathbf{1}\mathbf{G}_{cent}^T - \mathbf{G}^T \\ \mathbf{G}^T - (1+\alpha_0)\mathbf{1}\mathbf{G}_{cent}^T \end{bmatrix} \mathbf{I} \leq \mathbf{0} \\ &\mathbf{G}_{cent}^T \mathbf{I} = 1 \end{aligned} \tag{3.8}$$

3.2.5 Minimum Peak B-Field

As mentioned earlier in this chapter, higher slew rates are desirable in MRI. In recent day scanners, slew rate is mostly limited by a physiological effect called PNS. Switching gradient fields produces E-field and resulting induced voltage on the nerves. Although a comprehensive PNS threshold analysis should calculate E-field distribution inside the patient as well as neurodynamic properties [66], there are models that predicts PNS threshold that relates time rate of change in the vector magnetic field , dB/dT, to the PNS thresholds [67]. Similar to this relation, gradient fields generated in larger VOIs cause decrease in the PNS thresholds due to the increased E-field inside the geometry [61,68]. Therefore, it is expected that minimizing the maximum amplitude of the vector B-field would result in improved PNS thresholds. Minimization of the E-fields with a similar technique could be more effective; however, E-field generated by each coil should be calculated separately and they also depend on the electromagnetic properties of the subject. For simplicity, maximum amplitude of the vector B-field is minimized to show that dynamic optimization of gradient field might be expected to increase the PNS thresholds and increase the attainable slew rates.

Maximum amplitude of the vector B field inside a cylindrical volume with a diameter of 20 cm and length of 27.5 cm is defined B_{max} as in Eq. 3.9

$$B_{max} = \max_{\mathbf{r}} \left| \sum_{i=1}^{9} \mathbf{B}_i(\mathbf{r})\mathbf{I}_i \right| \tag{3.9}$$

where $\mathbf{r}$ is the all points inside the cylindrical volume and $\mathbf{B}_i(\mathbf{r})$ is a three dimensional magnetic field vector produced by the i^{th} channel. Please note that linear gradients are optimized in a certain VOI with parameters L_{VOI} and D_{VOI}. However, B_{max} calculations are performed in a bigger cylindrical volume independent of the target VOI since maximum magnetic field outside of the imaging region might still be effective in terms of PNS. A convex optimization problem is also formulated to minimize the B_{max} as follow:

$$\begin{aligned} &\min_{\mathbf{I}} B_{max} \\ &\begin{bmatrix} (1-\alpha_0)\mathbf{1}\mathbf{G}_{cent}^T - \mathbf{G}^T \\ \mathbf{G}^T - (1+\alpha_0)\mathbf{1}\mathbf{G}_{cent}^T \end{bmatrix} \mathbf{I} \leq \mathbf{0} \\ &\mathbf{G}_{cent}^T \mathbf{I} = 1 \end{aligned} \tag{3.10}$$

3.2.6 Simulations

The linear programming problem for minimum peak linearity error, maximum gradient strength and maximum slew rate are solved using "linprog" function of MATLAB-2017a. "Dual-simplex" algorithm is used to solve the linear programming problems. Conventional linear programming problem is defined as in

Eq. 3.11 where $\mathbf{x}$ is the free optimization variable, $\mathbf{f}$ is an arbitrary vector that its dot product with $\mathbf{x}$ is minimized, $\mathbf{A}$ and $\mathbf{b}$ are the matrix and vector for the inequality constraint, $\mathbf{A_{eq}}$ and $\mathbf{b_{eq}}$ are the matrix and vector for equality constraint. Last constraint defines the lower and upper bounds on the free parameter. All linear programming problems are already formulated to be compatible with this syntax.

$$\begin{aligned} &\min_{\mathbf{x}} \mathbf{f}^T \mathbf{x} \\ &\mathbf{A} \cdot \mathbf{x} \leq b \\ &\mathbf{A_{eq}} \cdot \mathbf{x} = b_{eq} \\ &lb \leq \mathbf{x} \leq ub \end{aligned} \tag{3.11}$$

Since optimization problems for minimum norm and minimum peak B-field are not linear but convex, they are solved using a local solver called "fmincon" using the "interior point method" which is another bulit-in function of MATLAB.

The achievable minimum linearity error is solved for both cylindrical and ellipsoid VOIs. L_{VOI} and D_{VOI} are swept between 2 to 20 cm with 2 cm step sizes to understand the effect of VOI on the peak linearity error. For other optimization problem types (2-5), spherical VOI with D_{VOI} of 20 cm is chosen, limit on the peak linearity error is swept between 1% to 51% and L_{VOI} is swept from 2 to 20 cm as in the previous cases.

3.3 Results

Fig. 3.2 shows the minimum possible α for both cylindrical and ellipsoid VOIs with variable diameters and lengths. Expectedly, dimension reduction in all directions can provide lower peak α. In the extreme cases, linearity error of the smallest simulated volume is more than millions time of the linearity error of largest simulated volume. Moreover, ellipsoid VOIs provides better gradient linearity than cylindrical VOIs with similar parameters. The volume difference between the cylindrical and ellipsoid VOIs are the edges of the cylinder which are

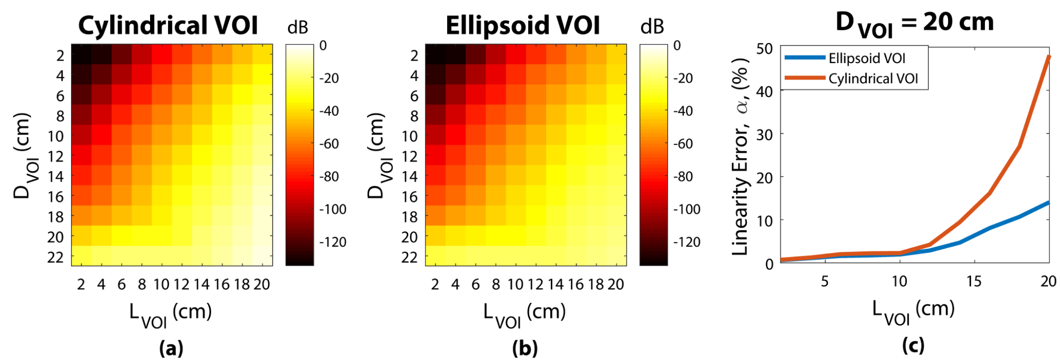

Figure 3.2: Optimization results to minimize the linearity error (α) for **(a)** Cylindrical VOI and **(b)** Truncated Ellipsoid VOI. α values are provided in dB calculated as $20log_{10}\alpha$) in (a) and (b) to represent the minimum α value of 0.02×10^{-5} (-134dB) and maximum α value of 0.52 (-5.6dB). **(c)** Comparison of minimum possible α for cylindrical and ellipsoid VOIs with diameter of 20 cm.

the most challenging parts to maintain gradient linearity.

Optimization results of (2-5) are shown in Fig. 3.3 which confirms that higher linearity error and/or smaller VOI can result in higher performance parameters in terms of maximum gradient, maximum slew rate, minimum current norm and minimum peak vector B-field. In most of the cases, 2 cm decrease in L_{VOI} or 2% increase in α can result in performance dramatic performance changes. On the contrary, performance parameters are less sensitive to changes in L_{VOI} and α, especially for the edges of the simulation domain. Therefore, these results can be used as lookup table to better utilize the tradeoffs between performance parameters for a specific application.

Fig. 3.4 shows example magnetic field profiles generated by optimized currents for constraint pairs of (L_{VOI} = 16 cm, 9 cm) and (α = 9% and 31%). The field distributions in Fig. 3.4 suggest that dependency of the performance parameters are as function of L_{VOI} and α are similar. It might be because of the fact that specifying maximum tolerable α and minimum required L_{VOI} might be enough to obtain near optimal solutions for all other performance parameters.

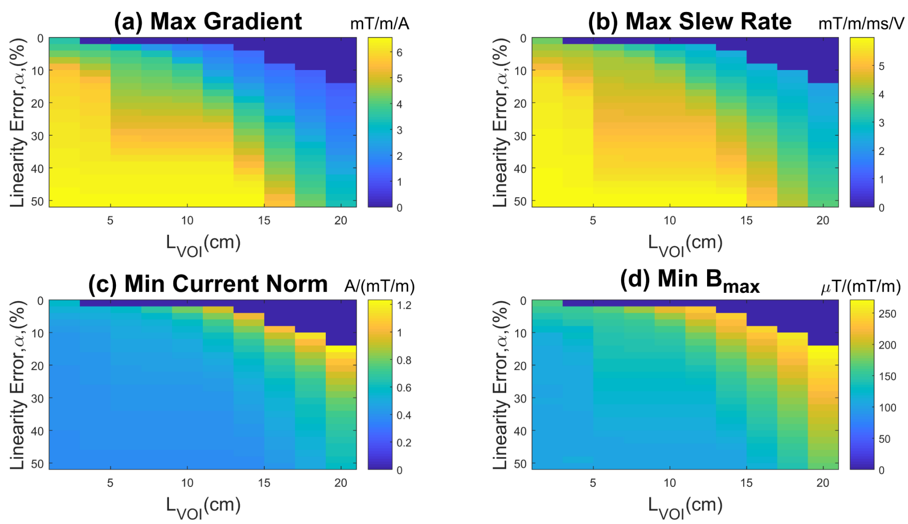

Figure 3.3: Optimization results for four different optimization problem that maximizes **(a)** gradient strength per unit amplifier current limit, **(b)** slew rate per unit amplifier voltage limit and minimizes **(c)** norm the gradient array currents per 1 mT/m gradient strength at the center, **(d)** the maximum amplitude of the vector B-field inside a B_{max} computation domain in Fig. 3.1 per 1mT/m gradient strength at the center of the VOI.

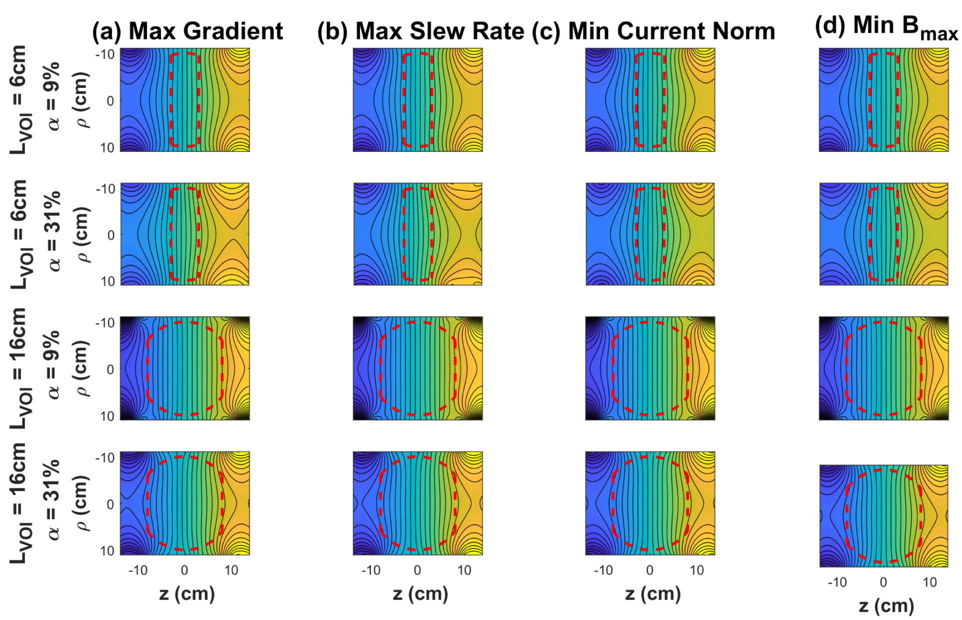

Figure 3.4: Example magnetic field profiles for optimization problems (2-5) with different L_{VOI} and α parameters.

3.4 Discussion

It is demonstrated that current of z-gradient array can be optimized for different performance parameters for a given allowed peak linearity error and size of the VOI dynamically. In this study each performance parameter is optimized separately; however, weighted average of these parameters can be optimized. In general, all performance parameters can be used in either constraints or in the cost function. For each specific sequence, demand on these parameters might change; therefore, optimization problems with fast and accurate solutions can be developed to address the need for fast computation of gradient waveforms during the sequence preparation.

First of all, optimization of gradient only in the current VOI does not affect the spins or imaging technique; therefore, optimization of VOI does not cause any disadvantage for the imaging. When the VOI is too small, some nonbijective regions of the gradient field distribution might overlap with the excited parts of the objects and cause alliasing for the imaging. Transmit or receive array RF coils can be used to suppress the signal coming from these overlapping parts. Another option is to force bijectivity of the fields inside some specified regions as part of the optimization problem.

Secondly, gradient linearity error can be post-corrected in most of the applications if the spatial dependency of the error is well known. Some disadvantages such as nonuniform SNR for each voxel might be observed despite the post-correction. Therefore, determining a tolerable limit for α required an investigation for each specific sequence. However, it would provide significant increase in the performance parameters as shown in Fig. 3.3 which might dominate the disadvantages remaining after post-correction.

Continuously wounded characteristics of z-gradient array enables more flexible z-gradient field profiles because it is similar to sampling a continuous current density as a function of z-coordinate. Some of the coil parameters might also improve or degrade the tradeoffs. Most important parameters are the total length of the coil as well as the number of channels distributed on the coil surface. For example, higher number of channels for a fixed coil length can provide more rapidly changing field profiles and opens up more space for improvement. However, increase in the performance might probably saturate after certain number of channels; therefore, required number of channels should be analyzed to utilize the performance tradeoffs more efficiently in exhange of increased hardware complexity.

Chapter 4

Local Optimization of Diffusion Encoding Gradients for TE Reduction in DWI

The content of this chapter was already presented in the 26th Annual Meeting of International Society for Magnetic Resonance in Medicine [69]. Some figures and text from this conference abstract are used in this chapter.

4.1 Introduction

Diffusion MRI is highly sensitive to diffusion of water molecules. Together with Diffusion Tensor Imaging (DTI), it provides information about micro structures such as tissue boundaries and membranes [70]. In addition to the capability of diagnosis of many diseases, diffusion MRI is also a strong tool to map the structural connectivity of the brain

Long diffusion encoding gradients are necessary to obtain high b-values. Increased diffusion duration cause increase in TE and T2 decay, which decreases the SNR and diagnostic quality of the MR images. In recent years, one of the technically leading efforts to map structural connectivity in the human brain is custom designed split gradient coils driven by separate amplifiers. Therefore, current flowing through gradient coils are increased without affecting the gradient field profile. These coils can achieve gradient strengths of 300 mT/m and slew rates up to 200 mT/m/ms as part of the Human Connectome Project (HCP) [16]. The increase in the available gradient strength enables shorter diffusion gradient durations for a desired b-value. In turn, the TE are reduced, which increases image SNR and allows room for higher spatial resolution or higher b-values [16].

Gradient array systems with multiple coils and amplifiers enables dynamic optimization of the spatial encoding magnetic field distribution as studied in Chapter 3. In this study, a 9 channel z-gradient array system described in Chapter 2 is used to maximize the gradient field strengths only in the target slice instead of the entire VOI to achieve shorter diffusion gradients for a fixed b-value. Reduction in TE for optimized gradient fields for a single slice instead of the entire VOI is validated with a phantom experiments. It is also validated with simulations that allowing more nonlinearity of the gradient field might increase attainable gradient strength in which b-value becomes spatially inhomogeneous.

4.2 Methods

Gradient array hardware described in Chapter 2 is also used in this chapter. A cylindrical volume with a diameter and length of 15 cm is determined as the general VOI as an example scenario. Two types of target volumes are defined as the entire VOI (B_{VOI}) and central slice (B_{slice}) in z-direction, as shown in Fig. 4.1.

A linear programming problem (2) in Chapter 3 is used to solve for the optimal current weights of the array elements that maximize the gradient strength given limitations of the amplifier (I_{max}) for predefined peak percentage gradient linearity error (α).

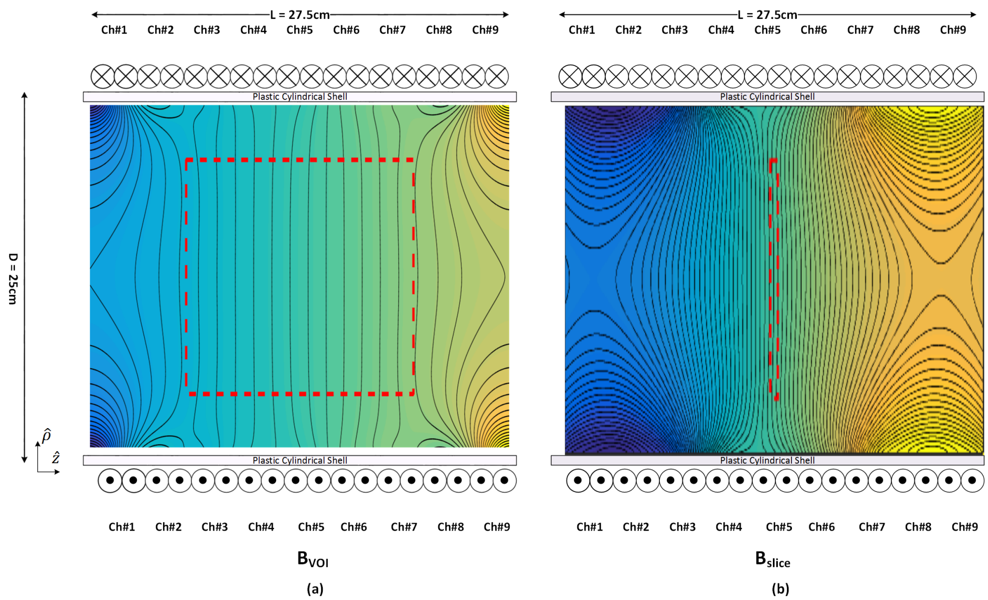

Figure 4.1: **(a)** Channel currents are optimized to create linear gradients inside a cylindrical VOI with a length and diameter of 15 cm. **(b)** Channel currents are optimized to create linear gradients only inside the central slice (z=0) with a thickness of 5mm and diameter of 15 cm. Red boxes indicate the corresponding VOI. Magnetic field difference between isocontours are same for both plots.

Additionally, the effect of the α inside the target slice is investigated for additional increase in the G_{max}. The effect of the α on the b-value can be post-corrected [71]. G_{max} is simulated for various slice locations and α.

A cylindrical homogenous phantom with a diameter of approximately 11 cm, and isotropic diffusion coefficient of 2200 μm^2/s is used in the experiments. T2 of the phantom is 75 ms, which is similar to T2 of the white matter. Although our custom-designed gradient amplifiers are designed as 50V and 20A, the maximum current is chosen as 7.5A to reduce the phase errors that might occur due to mechanical vibrations and possible instability of the amplifiers. Due to low current of the amplifiers, b-values are chosen as 175 s/mm^2 for both B_{VOI} and B_{slice} to demonstrate the proof of principle. T2 weighted spin echo images are acquired with 100% phase oversampling and averaging factor of 4 in a 150×150 mm FOV using a 3T MRI scanner (Magnetom Trio A Tim, Siemens Medical Solutions, Erlangen, Germany). Diffusion gradients in the z-direction are applied with the array coil and all other imaging gradients are applied with the system gradient

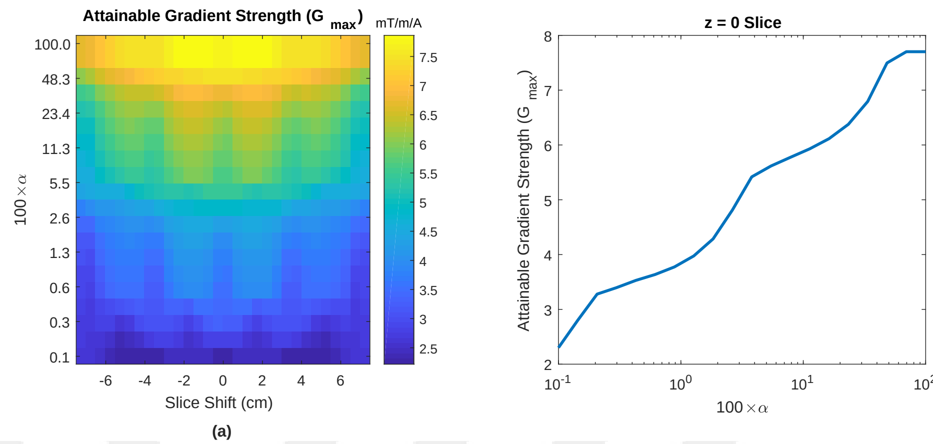

Figure 4.2: **(a)** Simulation results for the effect of the slice location and allowed gradient deviation on the G_{max}. Simulations are performed for every possible slice location inside the entire VOI. Gradients are optimized for 5mm slice thickness for each data point. α is swept between 0.1% and 100% logarithmically. Maximum and minimum attainable gradient strength among all cases are 7.9 mT/m and 2.2mT/m. **(b)** G_{max} is plotted against α for the central slice location.

coils.

4.3 Results

Optimized gradient field distributions for B_{VOI} and B_{slice} with $\alpha = 6\%$ are shown in Fig. 4.1. G_{max} values are 1.4mT/m/A and 5.5mT/m/A for B_{VOI} and B_{slice} respectively. In Fig. 4.2, G_{max} is reported for various α values at every possible single slice location inside the VOI. Fig. 4.2 validates that slice locations can be shifted within the VOI with approximately equal G_{max}. Furthermore, higher G_{max} can be achieved by sacrificing field linearity.

Attainable maximum gradient strength for B_{slice} is 4 times higher which shortened the diffusion gradients almost 3 times in our sequence timing. Diffusion gradient durations are 28.9 ms and 10.9 ms respectively for B_{VOI} and B_{slice} to obtain the same b-value at the center of the phantom. Fig. 4.3 shows the diffusion weighted images acquired using B_{VOI} (TE=75ms) and B_{slice} (TE=37ms). Such a TE difference causes nearly 66% increased signal level for B_{slice}, considering

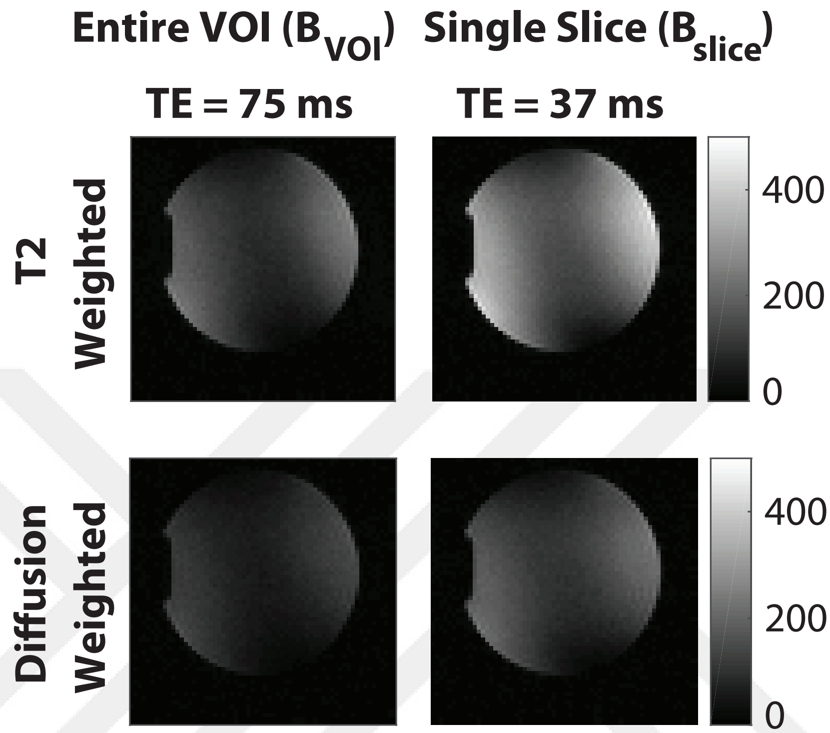

Figure 4.3: Diffusion weighted transverse MR images and calculated ADC map. **(First column)** Gradient field optimized for entire VOI (Fig. 4.1a) is used as a diffusion gradient with duration 28.9 ms and gradient strength of 10.3 mT/m. **(Second column)** Gradient field optimized only for the excited slice (Fig. 4.1b) is used as a diffusion gradient with duration 10.9 ms and gradient strength of 41.5 mT/m. **(First and second row)** shows the acquired transverse images with simulated central b-values of 0 and 175 s/mm^2. (All images are shown with the same color scaling.)

T2=75 ms for the phantom. In Fig. 4.4, b-value is calculated at each voxel separately using current weighted superposition of the previously measured magnetic field maps as in Fig. 2.2. This spatial map of b-value is used to correct the ADC maps. Inside a target region of 55mm diameter ROI, the ADC is 1900±400 $\mu m^2/s$ for B_{VOI}, which is lower than expected due to low SNR of DWI images [72]. The ADC map acquired using B_{slice} provides more accurate values of 2200±300$\mu m^2/s$ with reduced standard deviation.

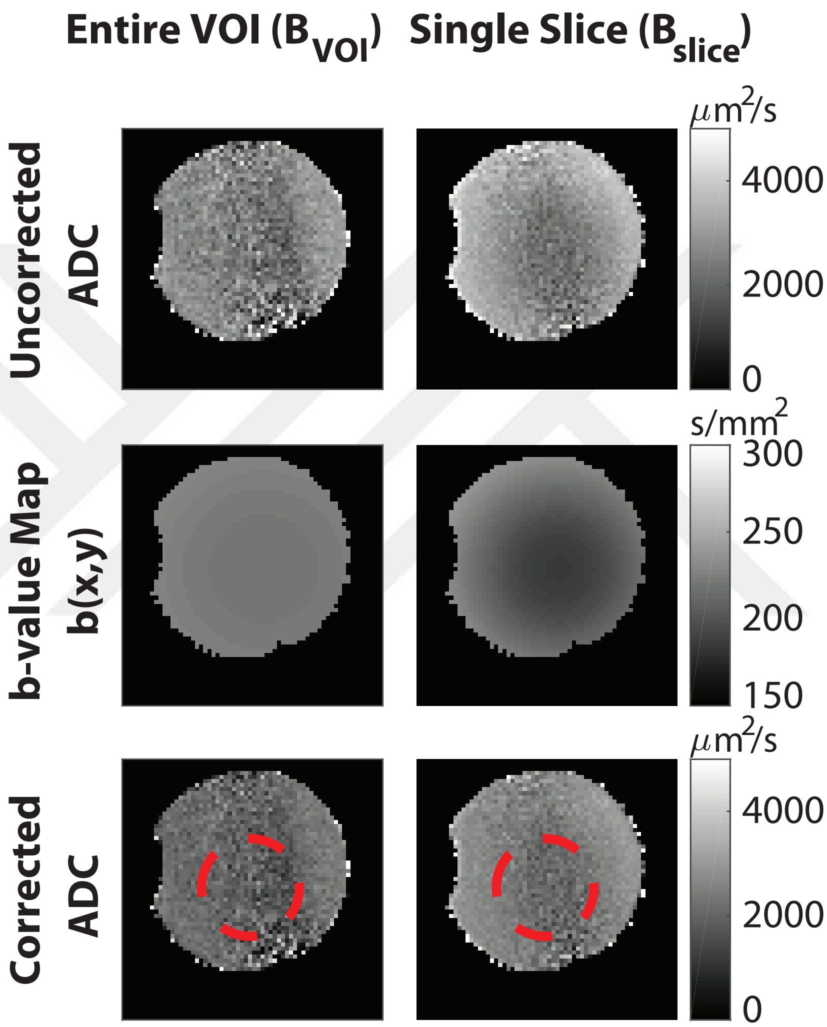

Figure 4.4: Correction of the ADC maps considering the spatial distribution of the b-value. Results are shown for the gradient field optimized for **(first column)** the entire VOI (Fig. 4.1a) and **(second column)** single slice (Fig. 4.1b). **(First row)** shows the reconstructed ADC maps for the two cases assuming a spatially constant b-value. **(Second row)** shows the calculated spatial dependency of the b-value using a previously measured, manually located field maps and assuming angular invariance. **(Third row)** shows the reconstructed ADC maps considering the spatial dependency of the b-values. (Red circle indicates a region of interest with 55mm diameter used in the mean and standard deviation calculations.)

4.4 Discussion

Preliminary experiments and simulations suggests that both local optimization of gradient fields only inside the target volume and/or more relaxed α limitations provides increased G_{max}, which leads to shorter diffusion durations and shorter TE. The method is validated for z-gradient due to the geometry of our windings. More generalized array of loops coils [41, 56]such as multi-coil or matrix coil, can be used to extend this work to arbitrary directions. Proposed method is also applicable for both whole body gradient coils and head insert gradient coils [62,73] and can be used to further increase the G_{max} in reduced target volumes.

Chapter 5

Simultaneous Multi-Slice Excitation with a Single-Band RF Pulse

The studies in this chapter related to multi-slice excitation with a single band RF pulse was published in Magnetic Resonance in Medicine [38]. Extension of this method for the excitation of multi-slab or doubling the number of excited RF pulses with a multi-band RF pulse was also presented in the 25th Annual Meeting of International Society for Magnetic Resonance in Medicine [74]. Content from both publications [38, 74] are utilized in this chapter.

5.1 Introduction

In MRI, SMS imaging is an effective method of accelerating image acquisition. SMS techniques have been applied for turbo spin-echo imaging [75], EPI-based fMRI [76] and diffusion sequences [77]. Notably, the excitation, refocusing or inversion of multiple slices requires demanding RF pulse designs. The simplest technique for designing such RF pulses is to superpose multiple single-slice RF pulses with different frequencies. However, the SAR and peak B1 amplitude are limiting factors for this technique, especially for a large number of slices, since the SAR and peak B1 amplitude increase linearly with the number of slices [17] and the peak RF power increases quadratically with the number of slices. Various techniques have been developed to overcome the limitations of multi-slice RF pulses, such as phase optimization [18], time shifting [19], PINS [20], MultiPINS [21], root flipping [22], optimal control theory [23] and parallel transmission [24–26]. All of these RF pulse design methods were developed for conventional linear gradient systems, which provide one-to-one mappings of different slice locations to different frequencies. Therefore, the multi-slice RF pulses must have either longer durations or higher SARs than single-slice RF pulses.Additionally, Multiband-Multislab technique has been recently proposed to combine the advantages of SMS with a 3D readout [78]. Although multislab excitation is less demanding than multislice excitation, RF pulses are always desired to be as short as possible due to B_0 robustness and shorter echo times.

Alternatively, multiple slice locations can be excited by a single-slice RF pulse if each slice location is mapped to the same frequency. Thus, a single-slice RF pulse can also be used for multi-slice excitation without modifications, thereby avoiding increases in the duration, SAR or peak RF power. Previously, Parker et al. [79] showed that linear gradients can be designed in multiple regions of interest to map multiple regions to the same frequency. In this study, field design methods are presented to dynamically map multiple slice locations or slab locations in the z direction to the same resonance frequency, and the resulting field profiles are used to excite multiple slices with a single-band RF pulse. These methods were validated using a z-gradient array in simulations and phantom experiments.

5.2 Theory

Mapping multiple slice locations to the same frequency requires nonlinear spatial encoding magnetic fields (N-SEMs), which are different from conventional linear gradient profiles. Additionally, the slice locations should be dynamically shifted during the sequence to span the entire VOI. Each shifted set of slice locations requires a different N-SEM distribution. To dynamically change the magnetic field distribution, an array of gradient coils is required, and each element should be driven independently with different current weightings to realize a dynamically changing N-SEM profile. In this section, two algorithms for designing N-SEMs oscillating in the z direction for a given set of slice locations and hardware constraints are presented.

5.2.1 Field Design Methods

Field design methods are formulated to excite M slices with a single-band RF pulse using N independent gradient channels, as shown in Fig.. 5.1. For ease of illustration, each gradient element is wound on the same cylindrical shell with an equal number of sequential turns without separation. The magnetic field generated by each gradient element is angularly invariant. For a given ρ and z, the total magnetic field or the first and second derivatives of the magnetic field with respect to the z direction produced at location (ρ, z) can be written as a linear combination of the contributions from each channel weighted by the current applied to each channel, as shown in Eq. 5.1:

$$B_z(\rho, z) = \mathbf{P}(\rho, z)^T \mathbf{I} \tag{5.1}$$

where $B_z(\rho, z)$ is the total perturbation magnetic field in the z direction at (ρ, z). The magnetic field is a function of z and the radial distance, ρ. $P(\rho, z)$ is an N-element column vector of functions containing single elements P_n that represent the magnetic field at (ρ, z) produced by the n^{th} channel when a unit current is applied. $\mathbf{I}$ is an $Nx1$ column vector containing the currents applied to each channel.

To excite multiple slices with a single-band RF pulse, the magnetic field B_z must be designed by optimizing the current weightings of the array elements. The desired magnetic field must map the resonance frequencies of the spins inside the desired slices to the bandwidth of the RF pulse, and all other spins outside the slices should be mapped out of the band of the RF pulse. We propose to use

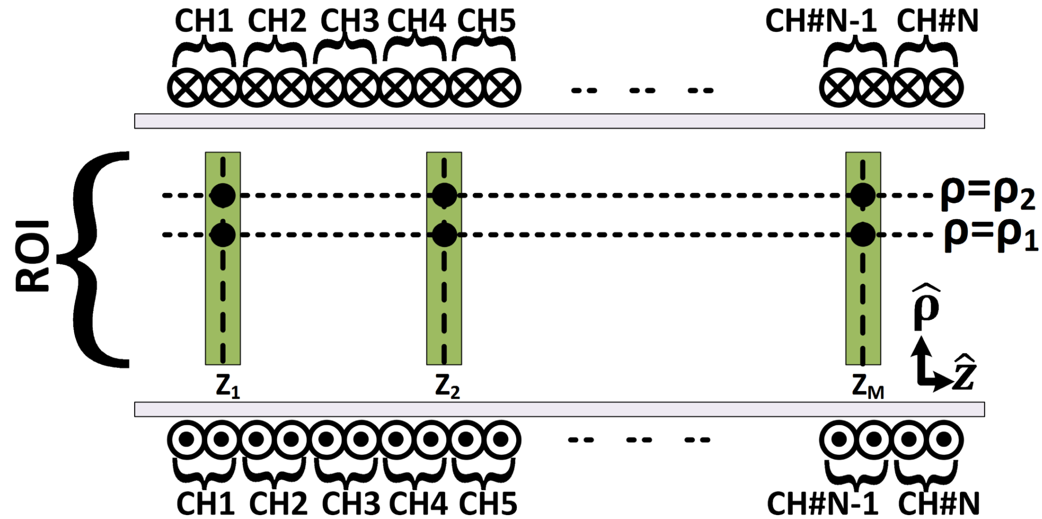

Figure 5.1: Schematic illustration of the z-gradient array for multi-slice selection. N-channel coil elements with no angular magnetic field variations are used to excite M different slice locations. One or two design points can be selected in each slice to determine the weightings of the currents that are applied to each array element to obtain the desired magnetic field distribution.

one or two design points in each slice, referred to as the 1PPS (one point per slice) and 2PPS (two points per slice) methods, respectively. In our approach, the magnetic field distribution at each slice location is similar to a linear gradient profile.

5.2.2 1 Point per Slice (1PPS)

In the 1PPS method, a single design point is determined at the center of each slice location, as in Fig.. 5.1. At each design point, three conditions must be satisfied. First, the magnetic field values at each slice location are equal; therefore, the resonance frequencies of the spins at all design points are forced to be equal. Second, the local gradient strength should be equal at each design point to obtain a constant slice thickness. The gradient strengths at neighboring slice locations are set with alternating polarity. Otherwise, there would be at least one other location with the same magnetic field value as the actual desired slice location, which would cause excitation of an additional undesired slice. Even so, alternating polarity of the gradients is necessary but not sufficient condition to avoid undesired excitation between the slices. Third, the second z-derivative of the magnetic fields is set to zero at the design points. Since the magnetic field distribution is angularly invariant and its Laplacian can be assumed to be zero [80], the second derivative with respect to the radial dimension vanishes at the center point. Considering the fact that first derivative with respect the ρ is zero by default due to angular symmetry, zero second derivative helps to extend the designed magnetic field distribution in the slice plane. Moreover, zero second derivative provides locally constant gradient strength in the slice direction. All three conditions are formulated as follows:

$$B_z(\rho = 0, z_i) = B_z(\rho = 0, z_{i+1}), \quad i = 1, ..., M - 1 \tag{5.2a}$$

$$\frac{\partial B_z(\rho = 0, z_i)}{\partial z} = -\frac{\partial B_z(\rho = 0, z_{i+1})}{\partial z} \quad i = 1, ..., M - 1 \tag{5.2b}$$

$$\frac{\partial^2 B_z(\rho = 0, z_i)}{\partial z^2} = 0 \quad i = 1, ..., M \tag{5.2c}$$

where M is the total number of slices and i is the slice index. In Eq. 5.2, there are a total of $3M-2$ independent linear equations. Note that even if the magnetic field satisfies these equations, this method does not guarantee a constant magnetic field and a constant magnetic field gradient at all locations in each slice of interest. The performance of this method needs to be investigated through simulations and experiments. Additionally, design point is selected at the center of each slice location throughout the study. However, design point radius can be used as another design parameter without changing the formulation of the method and some performance parameters depend on the design point radius.

5.2.3 2 Point per Slice (2PPS)

Similar to the 1PPS method, in the 2PPS method, the weightings of the currents applied to each gradient element are adjusted to generate magnetic fields that satisfy the following set of equations.

$$B_z(\rho_a, z_i) = B_z(\rho_b, z_j), \quad i, j = 1, ..., M \ and \ a, b = 1, 2 \tag{5.3a}$$

$$\frac{\partial B_z(\rho_a, z_i)}{\partial z} = (-1)^{i-j}\frac{\partial B_z(\rho_b, z_j)}{\partial z}, \quad i, j = 1, ..., M \; and \; a, b = 1, 2 \tag{5.3b}$$

Eq. 5.3a ensures that the magnetic field value is constant at all design points in all slice planes. The second set of equations (Eq. 5.3b) has two purposes. First, the local gradient strengths at different slice positions are equated up to alternating polarities to ensure a constant slice thickness, as in the 1PPS method. Second, within the same slice, the local gradient strengths at the two design points are equated and assigned the same polarity to extend the constant-slice-thickness region on the slice plane. The first and second sets of equations contribute to the homogeneity of the magnetic field over the transverse plane. Since the magnetic fields are designed at two design points in each slice, the profile deviation as a function of radius inside each slice is expected to be lower than in the 1PPS method. The 2PPS method requires $4M-2$ equations. This method can be generalized to an arbitrary number L of design points in each slice (LPPS) at the expense of an increased number of linear equations ($2 \times L \times M - 2$). Other possible design parameters include the radial coordinates of the design points ($\rho = \rho_1$ and ρ_2); however, these parameters are considered fixed at 40% and 95% of the imaging radius, respectively, throughout this study. Similar to the 1PPS method, the 2PPS method does not ensure a constant slice thickness throughout the entire slice plane. The performance of this method should also be evaluated through simulations and experiments.

5.2.4 Analytical Solution

The current weightings for each channel can be obtained by solving the equations of the 1PPS or 2PPS method. The number of gradient channels is assumed to be greater than the number of equations; therefore, the field equations are always solvable. However, the solution is not unique and has $N-3M+2$ or $N-4M+2$ degrees of freedom for the 1PPS and 2PPS methods, respectively. One way to use the degrees of freedom is to minimize the L2 norm of the current for a given gradient system:

$$\begin{aligned}
&min_{\mathbf{I}} \left\|\mathbf{I}\right\|_2 \ s.t. \\
&\mathbf{C}^T\mathbf{I} = 0 \\
&\mathbf{P}^{'}(\rho_a, z_i)^T\mathbf{I} = G_z \\
&\left\|\mathbf{I}\right\|_\infty \leq I_{max}
\end{aligned} \tag{5.4}$$

where $\mathbf{C}$ is a field constraint matrix with dimensions of either $N \times (3M-2)$ or $N \times (4M-2)$, depending on whether the 1PPS or 2PPS method is used. Each column in $\mathbf{C}$ represents a single field equation, determined by inserting Eq. 5.1 into Eq. 5.2 for the 1PPS method or into Eq. 5.3 for the 2PPS method. $\mathbf{P}^{'}(\rho_a, z_i)$ is the first z derivative of the previously defined vector $\mathbf{P}(\rho, z)$ at any design point, and G_z is the target gradient strength at the design points. The final constraint in Eq. 5.4 ensures that the maximum current that can be applied to the amplifiers, I_{max}, is not exceeded. Minimization of the L2 norm of the current can also be interpreted as minimization of the total power dissipation if the resistances of the gradient channels are equal.

Eq. 5.4 is a convex quadratic programming problem and can be easily solved using numeric techniques. This problem also has an analytical solution under certain conditions. Because of the field constraints, $\mathbf{I}$ must be in the null space of the field constraint matrix $\mathbf{C}^T$, which is full rank for non-identical slice locations. Another matrix $\mathbf{K}$ with dimensions of $9 \times D$ can be constructed: $\mathbf{K} = [\mathbf{e_1}\ \mathbf{e_2}\ ...\mathbf{e_D}]$, where $\mathbf{e_j}$ is an orthonormal basis for $null(\mathbf{C^T})$ and D is the dimensionality of $null(\mathbf{C^T})$. Therefore, $\mathbf{I}$ can be written as $\mathbf{I} = \mathbf{K}\boldsymbol{\lambda}$, where $\boldsymbol{\lambda}$ is a row vector of length D. The optimization problem in Eq. 5.4 can thus be converted into another optimization problem with the free parameter $\boldsymbol{\lambda}$:

$$\begin{aligned}
&\min_{\boldsymbol{\lambda}} \left\|\boldsymbol{\lambda}\right\|_2 \ s.t. \\
&\mathbf{P}^{'}(\rho_a, z_i)^T\boldsymbol{\lambda} = G_z \\
&\left\|\mathbf{K}\boldsymbol{\lambda}\right\|_\infty \leq I_{max}
\end{aligned} \tag{5.5}$$

If the amplifier limitation constraints are ignored, an analytical solution for $\boldsymbol{\lambda}$ can be found using the pseudo-inverse of $\mathbf{P}^{'}(\rho_a, z_i)\mathbf{K}$ that results in an optimal current solution to Eq. 5.4 as follows:

$$\mathbf{I} = G_z \frac{\mathbf{K}\mathbf{K}^{\mathbf{T}}\mathbf{P}'(\rho_a, z_i)}{\|\mathbf{K}^{\mathbf{T}}\mathbf{P}'(\rho_a, z_i)\|_2^2} \tag{5.6}$$

The analytical minimum norm solution expressed in Eq. 5.6 is feasible only for G_z values less than a certain limiting gradient strength, G_{lim}, which is analytically expressed as

$$\mathbf{G_{lim}} = I_{max} \frac{\left\|\mathbf{K}^{\mathbf{T}}\mathbf{P}'(\rho_a, z_i)\right\|_2^2}{\|\mathbf{K}\mathbf{K}^{\mathbf{T}}\mathbf{P}'(\rho_a, z_i)\|_\infty} \tag{5.7}$$

Otherwise, the amplifier current limitations are exceeded. For higher desired gradient strengths, numerical optimization should be performed. In this study, the analytical solution in Eq. 5.6 is primarily considered. The minimum norm solution has the advantage that the current vector is only scaled for different gradient strengths for gradient strengths less than G_{lim}. Additionally, this solution enables an analytical definition of a performance measure, g, defined as the gradient strength per unit norm current:

$$g = \frac{G_z}{\|\mathbf{I}\|_2} = \left\|\mathbf{K}^{\mathbf{T}}\mathbf{P}'(\rho_a, z_i)\right\|_2 \tag{5.8}$$

Since there is more than a single current flowing in the system, g is defined as the ratio of the gradient strength to the norm of the current; this definition differs slightly from the gradient strength per unit current defined for conventional gradient coils but can nevertheless be intuitively useful. The analytical expression in Eq. 5.8 is only valid for $G_z < G_{lim}$; when G_z is greater than G_{lim}, g begins to decrease and becomes dependent on G_z. The additional degrees of freedom can also be used to maximize $\mathbf{P}'(\rho_a, z_i)\mathbf{I}$ under similar conditions for the maximum attainable gradient strength using constraints similar to those in Eq. 5.4.

5.2.5 Multi-Slab Field Design

For the multi-slice excitation, magnetic fields are designed only at the center of the slice in z-direction. However, wider slices; in other words; slabs might require different approach. To extend the field design methods to multi-slab excitation, magnetic fields should be designed at multiple z-location inside a slab.

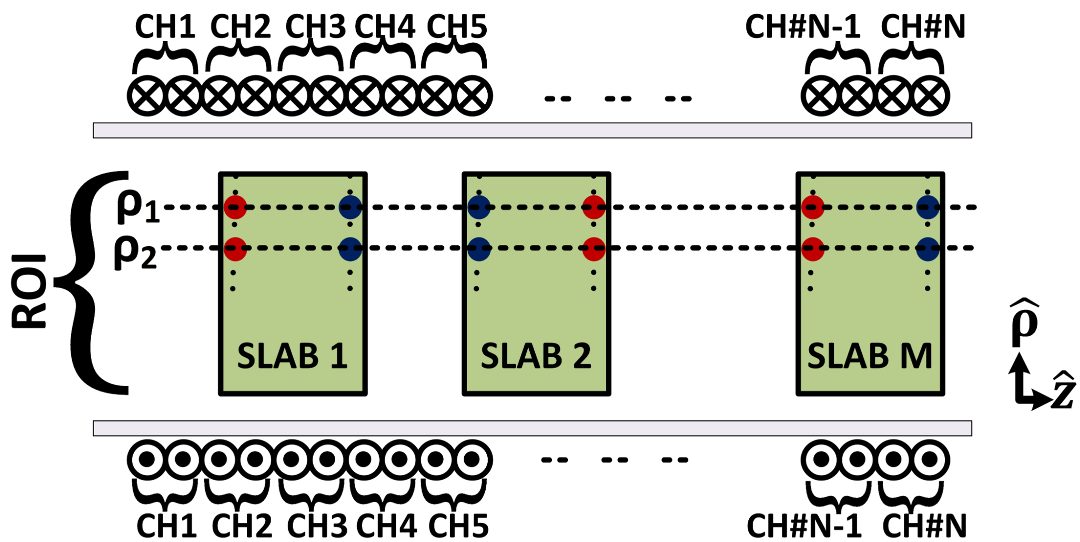

Figure 5.2: Field design technique for arbitrary number of channels (N) and arbitrary number of slab (M). First, two radial distances from the center of the coil are determined according to radius of interest. Afterwards, 4 points are specified as design points at the left and right edges of the slab location. Then, design points should be classified as red and blue points such that points with the same color will have the same magnetic field. At each z coordinate, the color should be the same and the order of the color should alternate between the slabs.

As explained in Fig. 5.2, two sets of design points have to be determined, and designing magnetic fields at only design points can produce linear gradients in the slab volume. Magnetic field of design points at each set should be equal. If two design points in the constant z plane are close enough, their first radial derivative vanishes. Due to zero Laplacian assumption of low frequency magnetic fields and angular symmetry of the coil, second z derivative also vanishes. After maximizing field difference between the two sets, linear gradient distribution is the only field distribution satisfying zero second derivative. Method requires at least 4M-2 channels where M is the number of slabs. After constructing the z matrix according the above equalities, optimization problem (Eq. 5.4) and optimal solution (Eq. 5.6) are also valid for multi-slab excitation scenario.

5.3 Methods

5.3.1 Simulation and Parameters

The slice locations are defined in terms of slice separation and shift. The slice separation is defined as the distance between the centers of adjacent slice locations. The shift is defined as the offset applied to the $z = 0$ line. A cylindrical volume with a 27 cm length and 15 cm diameter (60% of the coil diameter) is used as the VOI to determine the boundaries of the slice locations.

The 1PPS and 2PPS methods were simulated for several cases with varying slice shifts, slice separations, numbers of slices, and design point locations using MATLAB 2016b (Mathworks Inc., Natick, MA). Since the magnetic fields are designed only at the design points, z component of the magnetic field and the gradient strength as a function of the transverse radial distance is not constant. Two parameters are adopted as a measure of the slice profile accuracy. First parameter, σ_{center}, is the center location variation indicating the standard deviation of the z coordinates determined by the level set of magnetic field value at the design point as a function of the radius. In other words, σ_{center} quantifies the curvature of the slice shape as a deviation from an ideal central line of the slice. Center location variation is calculated at each slice separately and σ_{center} is reported as mean of the standard deviation across all slices in a multi-slice scenario. Second parameter is the percentage error of the normalized slice thickness at each radial coordinate on the line determined by the z coordinate of the slice location is defined with respect to the slice thickness at the design point. To obtain a single performance measure, the RMSE of the normalized slice thickness can be determined by calculating the root mean square (RMS) of this value for all points on all slices. Both parameters are not affected by the scaling of the current vector, $\mathbf{I}$; therefore, they provide a measure of the magnetic field profile independent of the gradient strength and amplifier specifications. Furthermore, the gradient strength per unit current, g, is used to analyze the performance of the design method and the coil geometry independent of the amplifier specifications. Furthermore, the dissipated power, P_{diss}, is calculated as $\mathbf{I^T R I}$ using the calculated current vector. The maximum amplitude of the B field inside the VOI, B_{max}, is calculated by superposing the simulated 3D vector magnetic field distributions of each channel using the weightings specified by $\mathbf{I}$.

5.3.2 Experiments

Experiments of this is conducted using a 9 channel z-gradient array prototype which is described in Section 2.2. This coil is also driven by 9 home-built GPAs and custom-designed user-interface as described in Section 2.3.

In the experimental validations, measured magnetic field maps were used as inputs to the 1PPS and 2PPS methods. The first and second spatial derivatives of the measured magnetic field distributions are not directly used in the proposed field design methods since any noise in the measured field maps will be amplified by the derivative operation. Instead, the measured magnetic fields are fitted to the simulated magnetic fields along a single line. Fitting is performed for three parameters, namely, the amplitude of the magnetic field (A), the spatial shift (Δz) and the spatial scaling (W), as follows:

$$\min_{A,\Delta z,k} \int \left(\tilde{B}_z - AB_z\left(\frac{z}{W} + \Delta z\right)\right)^2 dz \tag{5.9}$$

where $B_z(z)$ is the simulated magnetic field along a line and $\tilde{B}_z(z)$ is the measured magnetic field along the same line. In the final step, the fitted magnetic field distributions are used to calculate the spatial derivatives of the magnetic fields to prevent noise amplification. Since fitting is performed only to suppress spatial noise, other parameters, such as coil rotation, are neglected.

The current weightings for each channel are calculated using Eq. 5.6 for a gradient strength of 12.5 mT/m. To obtain a slice thickness of 5 mm, an RF pulse is applied with a Hanning-windowed sinc pulse envelope with a duration of 1.5 ms and a time-bandwidth product equal to 4. The gradient amplitudes and the current waveforms, including the refocusing lobe, are specified using the control interface. The slice selection gradient of the original scanner sequence is turned off. RF spoiled 3D GRE sequence was used to validate the design methods.

Readout was performed in the z direction to decrease the spatial resolution in the slice direction to 0.2 mm, whereas the in-plane resolution was 5 mm. The flip angle and TR were 40° and 100 ms respectively. At the beginning of the experiment, a reference 3D image was obtained without any slice selection. All images were normalized to the reference image to avoid any misleading influence from the Tx/Rx sensitivities of the RF coil on the slice profiles.

5.4 Results

5.4.1 Simulation of Slice Profiles

Since our gradient coil array has nine elements, a single-band RF pulse can excite a maximum of three or two slices using the 1PPS and 2PPS methods, respectively. Gradient magnetic fields were designed for two and three slice locations with 13.5 cm and 9 cm slice separations using the 1PPS method. The 2PPS method is used to design magnetic fields for two slices with a 13.5 cm separation. (see Fig. 5.3). The slice separations were selected such that with the shifting of all slices as shown in the following measurements, the entire 27 cm length of the cylindrical volume could be covered. In Fig. 5.3, the slice locations are centrally symmetric for simplicity, and the slice profiles for multi-slice excitation with a single-band RF pulse are shown. In Figs. 5.3d-5.3f, the magnetic field profiles along the lines are examples of spatially oscillating N-SEM distributions. The dashed lines and red boxes indicate the center frequency of the RF pulse and the corresponding mapping to the spatial domain for a given slice thickness. Figs. 5.3a-5.3c show that the slice profiles exhibit a curvature, especially for the 1PPS method. In Figs. 5.3g-5.3i, the percentage errors of the slice thickness as a function of ρ are presented. The slice profiles become thinner near the edges. Specifically, for the 1PPS method, the slice thickness is 45% (2-slice) or 76% (3-slice) lower at the boundary of the VOI than at the center. By contrast, for the 2PPS method, the slice thickness error is less than 5%.

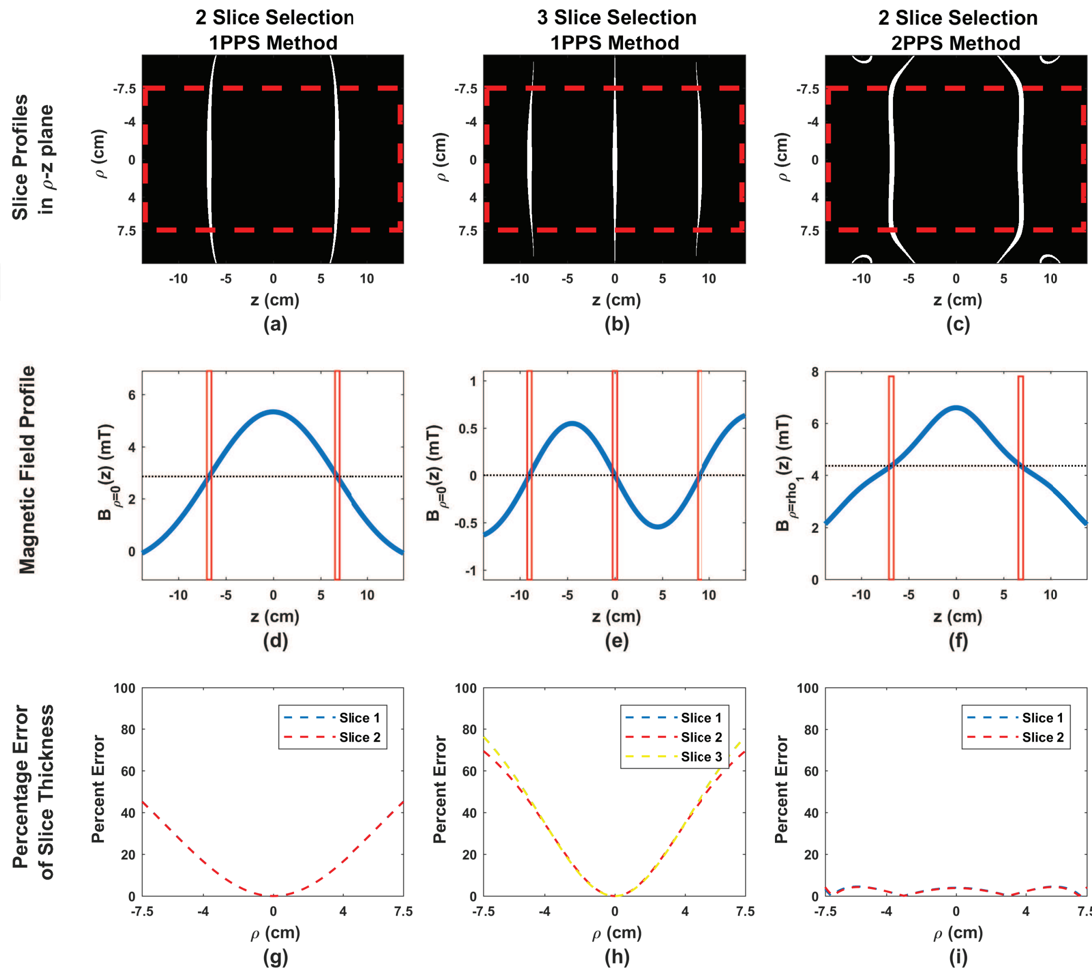

Figure 5.3: Simulated results for 2-slice (left column) and 3-slice selection (middle column) with the 1PPS method and 2-slice selection with the 2PPS method (right column). **(a-c)** Slice profiles excited by a single band RF pulse. The slice profiles were determined by assuming an ideal RF pulse with a perfectly rectangular slice profile corresponding to a slice thickness of 5 mm at the design points. The red boxes encompass the entire VOI. **(d-f)** As examples of spatially oscillating magnetic fields, the one-dimensional magnetic field profiles on the lines $\rho = 0$ and $\rho = \rho_2$ are shown for the 1PPS and 2PPS methods, respectively. The dashed line corresponds to the RF excitation frequency. The red boxes indicate the multiple slice locations corresponding to the bandwidth of a single-band RF pulse. **(g-i)** The percentage errors of the slice thickness at all slice locations as a function of radius.

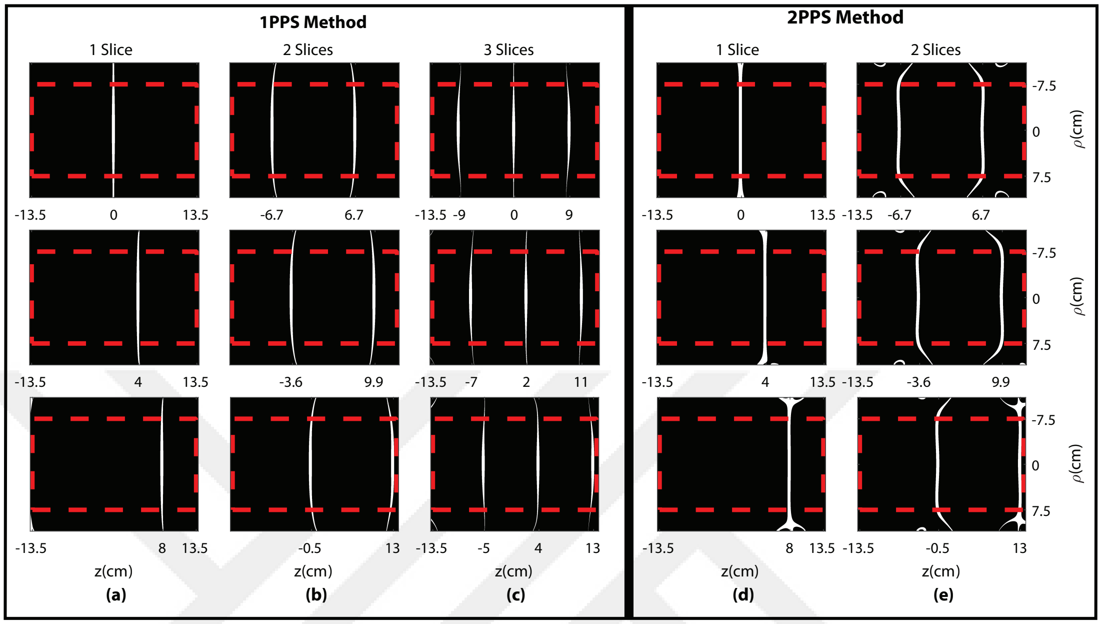

Figure 5.4: Example slice profiles. **(a)** 1PPS – 1 slice: on the center and shifted by 8 cm. **(b)** 1PPS – 2 slices with 13.5 cm separation: on the center and shifted by 6.4 cm. **(c)** 1PPS – 3 slices with 9 cm separation: on the center and shifted by 4 cm. **(d-e)** 2PPS – 1 slice (d) and 2 slices (e). The slice shifts and separations for the 2PPS method are the same as those for the 1PPS method with the same number of slices. (Slice locations are indicated with labels, and the red dotted window corresponds to the entire VOI.)

The 1PPS and 2PPS methods can similarly be applied for shifted slice locations, as demonstrated in Fig. 5.4. Figs. 5.4a-5.4c show the results of using the 1PPS method for the excitation of one, two and three slices, respectively. Similarly, the use of the 2PPS method to excite a single slice and two slices is demonstrated in Figs. 5.4d and 5.4e, respectively. The first row shows centrally symmetric excitation, and the second row shows shifted slice locations with various shifts, as indicated in the figure. Furthermore, the proposed methods are not only valid for multi-slice excitation but also useful for single-slice excitation. Note that multiple-slice locations can be shifted to cover the entire VOI with consecutive multi-slice acquisitions.

There are possible problems in 3D imaging such as overlaps and gaps between the slices as slices are shifted to cover the entire VOI since slice thickness and the center location of the slice varies as a function of radius. Total volume coverages

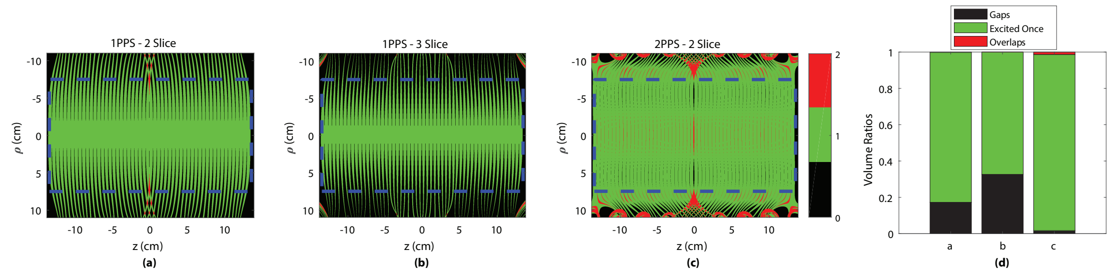

Figure 5.5: Representation of total excitation when the set of shifted slices are excited evenly to cover the entire VOI. **(a)** 1PPS - 2 Slice **(b)** 1PPS – 3 Slice **(c)** 2PPS – 2 Slice. Blue rectangle represents the VOI. Volume is classified into three sub-volumes such as (black) gaps that are not excited by any of the excitations, (green) properly excited once, (red) overlaps that are excited more than once during the set of shifted slice excitations. **(d)** Bar graph representation for percentages of sub-volume for (a-c). 2D images are integrated to calculate the volume fractions in 3D.

of the methods are displayed in Supporting Fig. 5.5a-5.5c when each excitation is the one slice thickness shifted version of the previous excitation. The bar graph in Fig. 5.5d shows that 1PPS method can excite 74% and 54% of the VOI properly for 2 and 3 slices respectively. The 2PPS method for 2 slice excitation can excite 97% of the VOI. Remaining volumes can be considered as gaps between the shifted slices because overlapping volumes are less than 1% for all cases.

5.4.2 Effect of Slice Separation and Shift

The performance of the proposed methods significantly depends on the slice separation and shift. In Fig. 5.6, the simulated RMSE of the normalized slice thickness, center location variation and the simulated gradient strength per unit norm current are shown for two- and three-slice excitation with the 1PPS method and two-slice excitation with the 2PPS method.

The slice thicknesses obtained using the 1PPS method show larger variations in the slice plane compared with the 2PPS method. On the contrary, 1PPS method shows slightly lower center location variation compared to 2PPS method on the average. Additionally, the RMSE of the normalized slice thickness and the

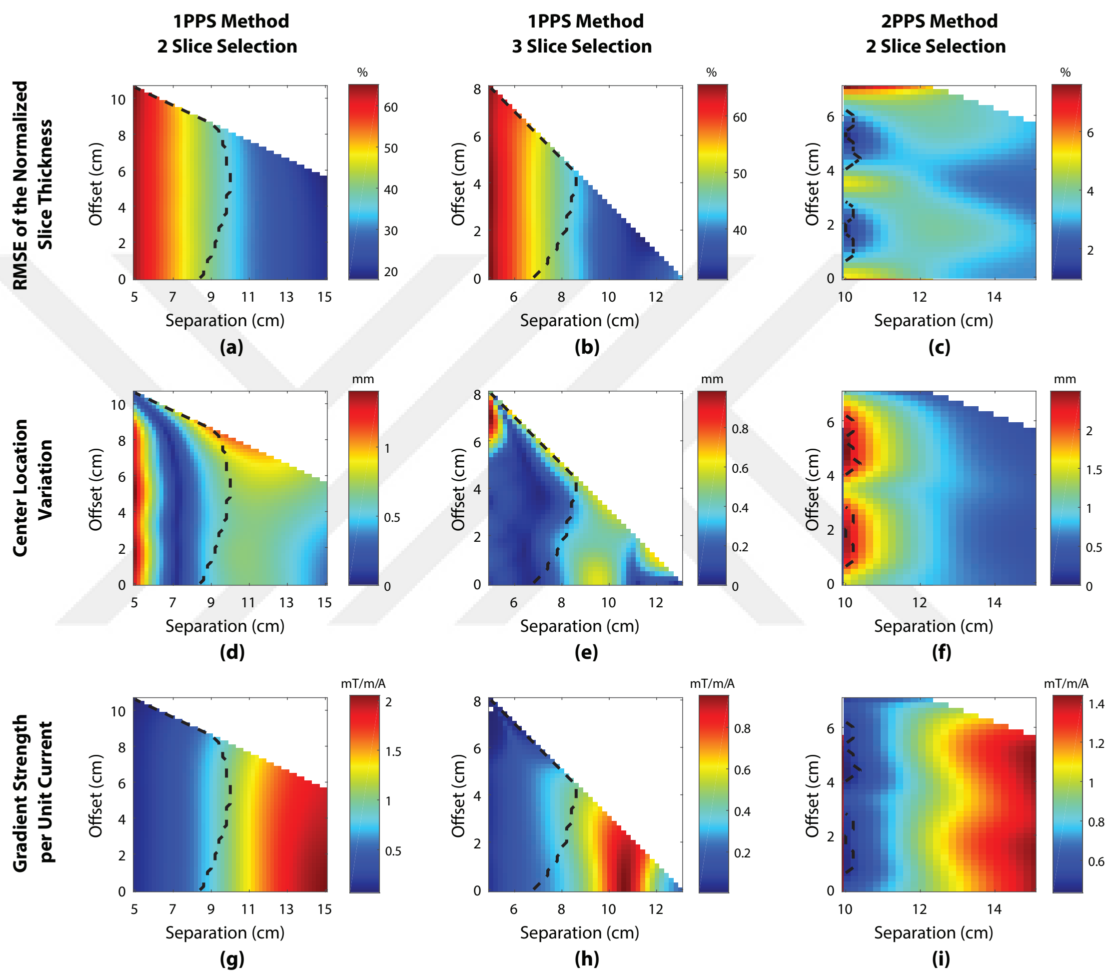

Figure 5.6: Effects of slice separation and shift on system performance. **(First row)** RMSE of the normalized slice thickness over all excited slices. **(a)** 1PPS – 2 slices (min = 18%, max = 65%). **(b)** 1PPS – 3 slices (min = 25%, max = 66%). **(c)** 2PPS – 2 slices (min = 1%, max = 8%) **(Second row)** Center Location Variation (σ_{center}) **(d)** 1PPS – 2 slices (min = 0.0, max = 1.4 mm). **(e)** 1PPS – 3 slices (min = 0.0, max = 1.0 mm). **(f)** 2PPS – 2 slices (min = 0.3, max = 2.5 mm) **(Third Row)** Gradient strength per unit norm current for the minimum norm solution at the design points (g). **(g)** 1PPS – 2 slices (min = 0.1, max = 2.1 mT/m/A). **(h)** 1PPS – 3 slices (min = 0.003, max = 1.0 mT/m/A). **(i)** 2PPS – 2 slices (min = 0.4, max = 1.4 mT/m/A). The left side of the dashed boundaries corresponds to undesired excitation of a sub-volume inside the VOI.

gradient strength per unit current primarily depend on the slice separation; the effect of the shift may be ignored for both the 1PPS and 2PPS methods, except for smaller slice separations in the case of the 2PPS method. In general, the effect of the shift on the center location variation can still be neglected unless some of the slices are near the edge of the coil. For the 1PPS and 2PPS methods, closer slice locations cause a significant increase in the RMSE of the slice thickness, increased center location variation and a decrease in the gradient strength per unit norm current. Therefore, the minimum simulated slice separations are 5 cm for the 1PPS method and 10 cm for the 2PPS method. For 2-slice excitation with the 1PPS and 2PPS methods, the performances in terms of the RMSE of the slice thickness, the center location variation and the gradient strength per unit current do not deviate for slice separations greater than 15 cm. The 1PPS method results in a higher gradient strength per unit norm current and lower center location variation than the 2PPS method for the excitation of 2 slices with the same separation, at the expense of greater slice thickness variation.

5.4.3 Effect of Design Point Selection

Effects of the location of design points are also investigated. Performance evaluations of 1PPS method and 2PPS methods for a set of design point locations are presented in Fig. 5.7 and Fig. 5.8.

5.4.4 Comparison of Methods

The performances of the proposed 1PPS and 2PPS methods are compared in Table 1 in terms of the RMSE of the normalized slice thickness, center location variation (σ_{center}), G_{lim}, the gradient strength per unit norm current (g), the power dissipation per unit gradient strength and the maximum magnetic field value per unit gradient strength. The magnetic field distributions are designed for various numbers of simultaneously excited slices for shift values of 0 cm and 3 cm. A greater number of slices results in decreased (g), decreased G_{lim}, an increased

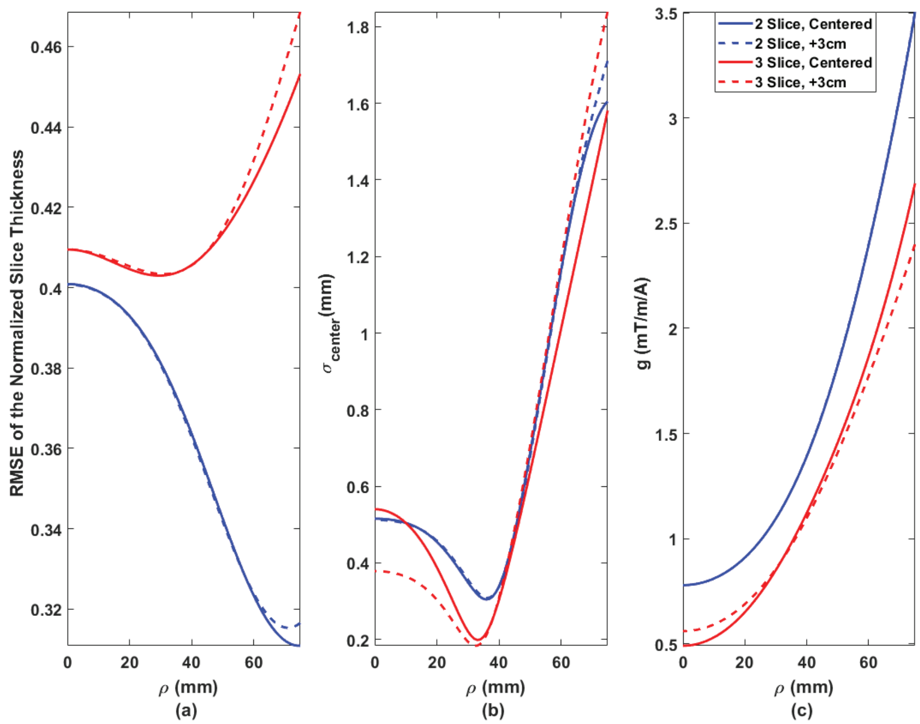

Figure 5.7: Performance evaluation of design point selection in the 1PPS method for excitation of 2 and 3 slices with a separation of 9 cm including both centrally symmetric and 3 cm shifted slices. **(a)** RMSE of the normalized slice thickness **(b)** center location variation (σ_{center}) **(c)** gradient strength per unit norm current, (g), as a function of design point radius are plotted.

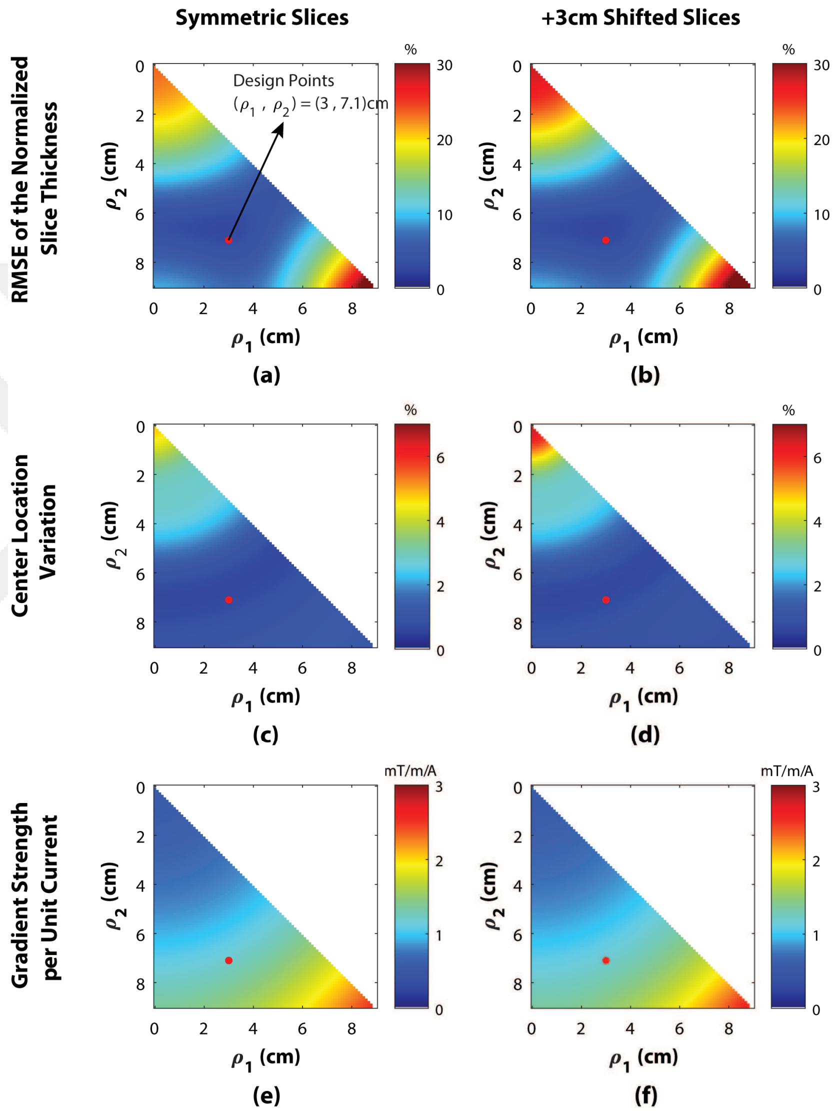

Figure 5.8: Performance evaluation of design point selection in the 2PPS method for excitation of 2 slices with a separation of 13.5 cm. **(a)** RMSE of the normalized slice thickness for symmetric placement of slices around the center. **(b)** RMSE of the normalized slice thickness for slice locations as shifted +3 cm according to the previous case. **(c)** Center location variation for symmetric slices. **(d)** Center location variation for shifted slices. **(e)** Gradient strength per unit current norm for symmetric slices. **(f)** Gradient strength per unit current norm for shifted slices. (Red dot indicates the choice of the design points used in the entire study.)

Table 5.1: Comparison of the 1PPS and 2PPS methods for different numbers of slices and different shifts in terms of the RMSE of the normalized slice thickness, center location variation (σ_{center}), G_{lim}, the gradient strength per unit norm current (g), and the power dissipation (P_{diss}) and maximum amplitude of the magnetic field (B_{max}) for a gradient strength of 1 mT/m.

	1PPS Method						**2PPS Method**			
	Shift = 0 cm			**Shift = 3 cm**			**Shift = 0 cm**		**Shift = 3 cm**	
Slice#(N)	N=1	N=2	N=3	N=1	N=2	N=3	N=1	N=2	N=1	N=2
RMSE (%)	17	23	41	17	23	41	2	3	2	3
$\boldsymbol{\sigma_{center}}$**(mm)**	0.0	0.5	0.5	0.1	0.6	0.4	0.0	0.6	0.1	0.6
$\mathbf{G_{lim}}$**(%)**	125	57	19	121	55	20	99	28	95	27
g(mT/m/A)	2.8	1.9	0.5	2.7	1.9	0.6	2.3	1.2	2.2	1.2
$\mathbf{P_{diss}}$**(mW)**	170	360	5390	180	390	4170	250	980	260	1010
$\mathbf{B_{max}}$**(**$\boldsymbol{\mu T}$**)**	80	136	107	88	156	137	98	244	114	272

RMSE of the normalized slice thickness, increased σ_{center}, increased dissipated power and an increased maximum magnetic field. Furthermore, the 1PPS method results in magnetic fields with slightly lower center location variation, higher gradient strength, less dissipated power, and a lower B_{max} than the magnetic fields generated using the 2PPS method, but the slice thickness error increases with the 1PPS method.

5.4.5 Experimental Validation

To validate the proposed design methods, the 1PPS and 2PPS methods were applied to both single-slice and multi-slice excitation with a single-band RF pulse, as shown in Fig. 5.9 and Fig. 5.10 respectively. The 1PPS method is demonstrated for one, two and three slices in Figs. 5.9a – 5.9c. The 2PPS method is demonstrated for single-slice and two-slice excitations in Figs. 5.10a and 5.10b. The first row in the figure shows the designed magnetic field for each case and the magnetic field distribution obtained by superposing the field maps of all channels weighted by the optimized current values. The second row shows the expected small-tip-angle slice profiles for a thickness of 5 mm at the design points under the application of an RF pulse. The third row shows experimental central coronal images to validate the expected slice profiles in the second row. In the last row, two example coronal and sagittal images are shown in 3D views to validate the slice homogeneity in both planes.

Slice profiles for two-slice excitation with the 2PPS method are plotted in Fig. 5.11. The central coronal image shown in Fig. 5.10b is plotted again to present the slice profiles at different radii in Fig. 5.11a. In Fig. 5.11b, measured and expected slice profiles at the center, at the design points and along arbitrary lines from both the upper and lower half planes are provided. Furthermore, the slice thickness and center location of the slice profile at each radius were calculated by finding the full width at half maximum (FWHM) of the slice profile using cubic interpolation. From the experimental data, the standard deviation of the normalized slice thickness and the center location variation across all radii were calculated to be 11% and 1 mm, respectively. For the simulations with an ideal coil, the standard deviation of the normalized slice thickness and the center location variation were calculated to be 3% and 0.6 mm, respectively.

5.4.6 Excitation of Simultaneous Multi-slab

The first column of Fig. 5.12 shows the simulations of the designed SOMFs for each shifted case. Second column indicates the design points on top of the excited slab profiles with a single band RF pulse. Third column in Fig. 5.12 shows the slice profiles excited with superposition of 3 RF pulse with different frequencies, i.e. multi-band RF pulse. Maximum attainable gradients and RMSE of the slab thickness are around 25 mT/m and 5%, respectively.

Magnetic field profile is obtained with a summation of measured field profiles of each channel weighted by the optimized current for 4 cm slab thickness and 9.5cm slab separation. Fig. 5.13a is the expected magnetic field distribution obtained with measured field profiles. Fig. 5.13b shows the coronal image of a phantom to demonstrate the slab excitation with a single-band Hamming-windowed sinc pulse. Fig. 5.13c shows 6 slices excited with a superposition of 3 RF pulses with

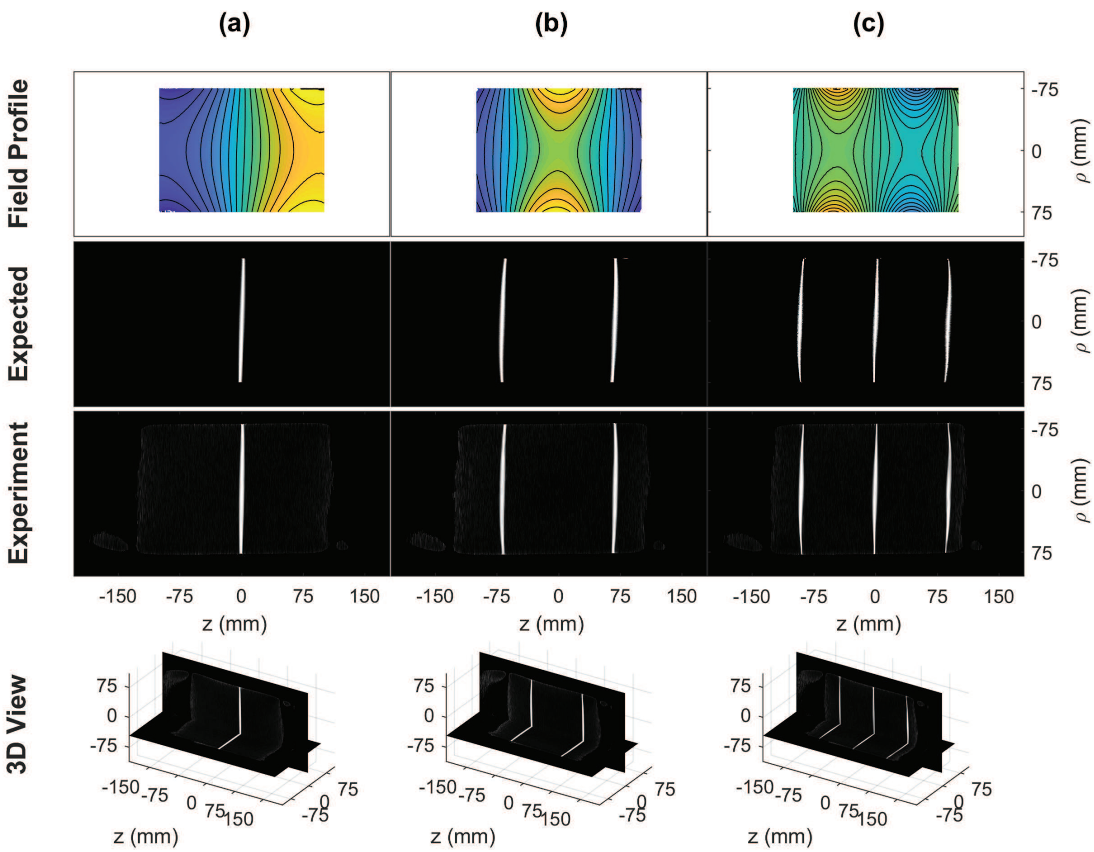

Figure 5.9: Experimental validation of the 1PPS method: **(a)** 1 slice, **(b)** 2 slices, **(c)** 3 slices. **(First row)** The magnetic field distribution for each case, obtained by superposing the magnetic field profiles of all channels with the current weightings. **(Second row)** The expected slice profiles in the small-tip-angle regime based on the magnetic field distributions in the first row, obtained by simulating the RF pulse applied in the experiments. **(Third row)** Experimental central coronal images, acquired to validate the design methods and the expected slice profiles. **(Fourth row)** Experimental coronal (y = -30 mm) and sagittal (x = -46 mm) images shown in 3D views. (All experimental images are normalized with respect to the reference scan without any slice selection.)

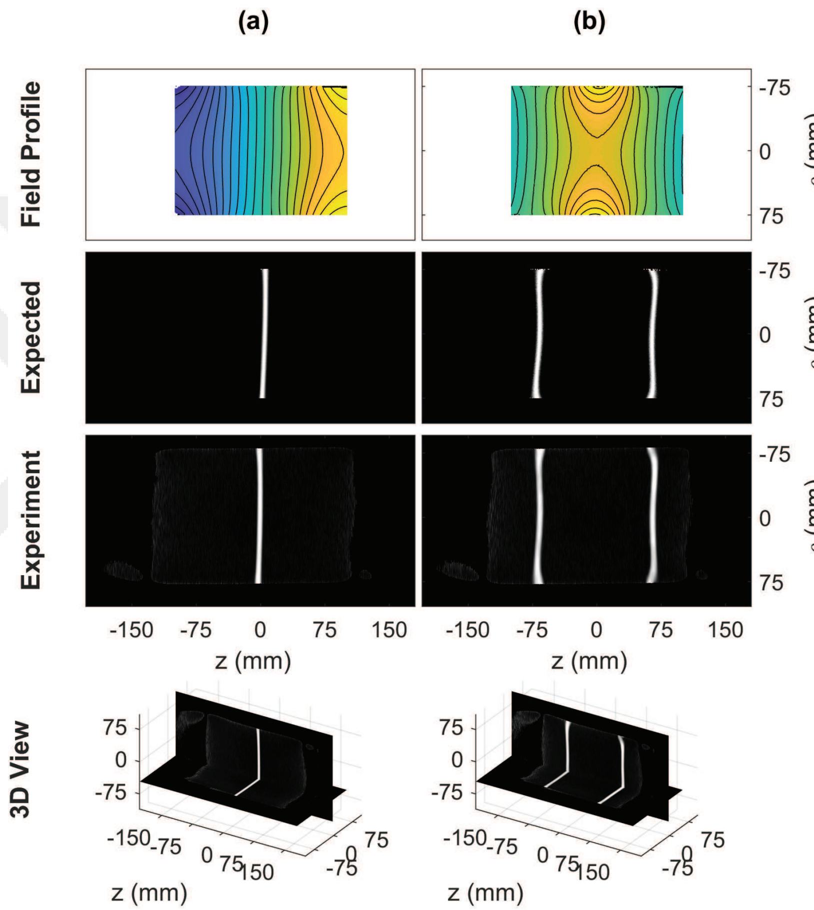

Figure 5.10: Experimental validation of the 2PPS method: **(a)** 1 slice, **(b)** 2 slices. **(First row)** The magnetic field distribution for each case, obtained by superposing the magnetic field profiles of all channels with the current weightings. **(Second row)** The expected slice profiles in the small-tip-angle regime based on the magnetic field distributions in the first row, obtained by simulating the RF pulse applied in the experiments. **(Third row)** Experimental central coronal images, acquired to validate the design methods and the expected slice profiles. **(Fourth row)** Experimental coronal (y = -30 mm) and sagittal (x = -46 mm) images shown in 3D views. (All experimental images are normalized with respect to the reference scan without any slice selection.)

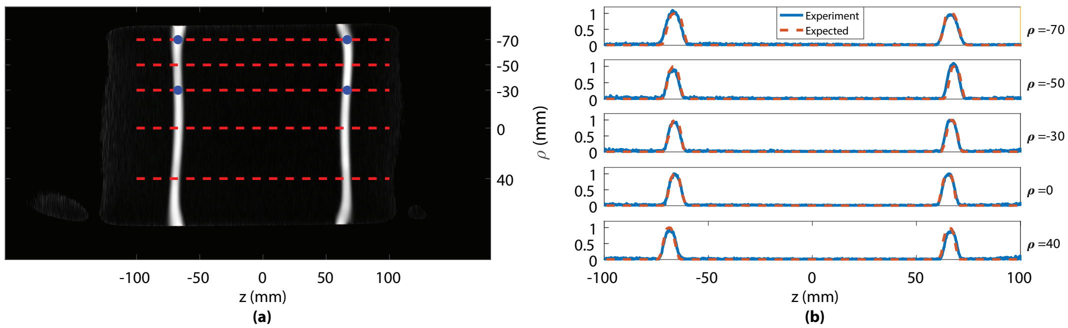

Figure 5.11: Experimental validation of the 2PPS method: **(a)** Slice profiles measured under excitation using the 2PPS method (blue dots indicate the design points). **(b)** Line plots of the expected and measured slice profiles at different radii for two-slice excitation with the 2PPS method.

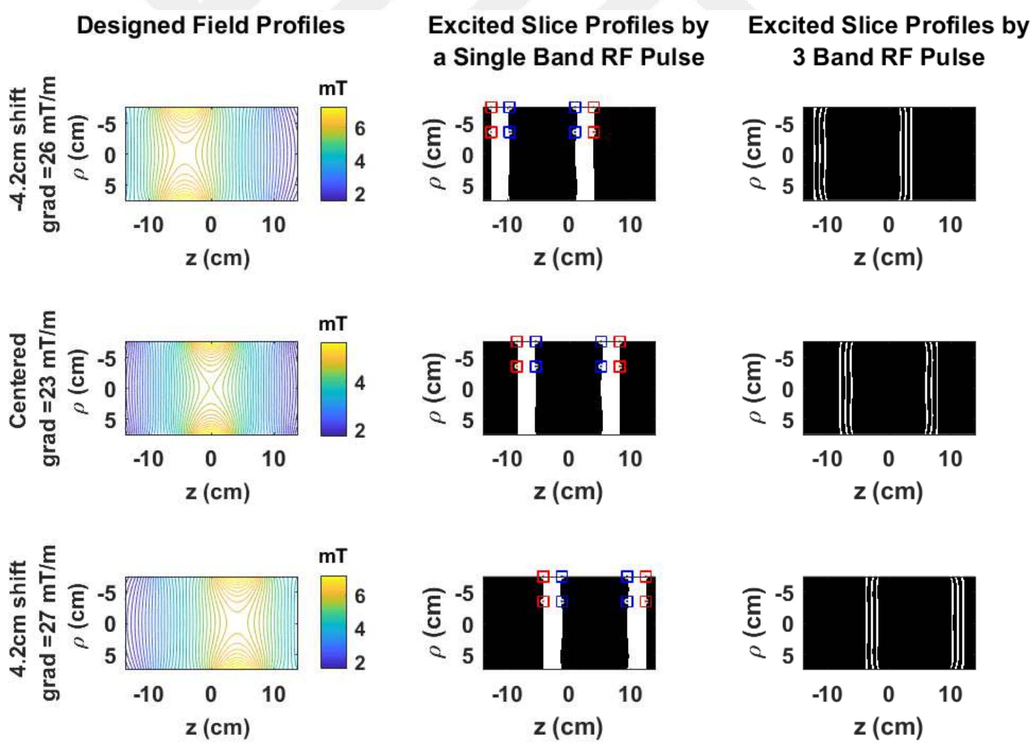

Figure 5.12: Each row shows the shifted slab locations to cover the whole volume. Slabs are shifted for +4.2 0 and -4.2cm according to z center of coil. Different currents are applied to elements at each case and attained gradient strengths are reported. **(First column)** Obtained magnetic field distributions for 3cm slab thickness and 10.5cm slab separation. **(Second column)** Slab profiles and design points in Fig. 5.2 **(Third column)** 6-slice profiles excited with a 3 band RF pulse. Slice thickness is 3mm and slice separation is 9mm.

different frequencies.There are intensity variations due to B0 field inhomogeneity, RF transmit and receive sensitivity inhomogeneity and averaging in the y direction.

5.5 Discussion

5.5.1 RF Pulse Design

One of the advantages of the proposed methods is that any pulse sequence design algorithm for single-slice excitation, such as the SLR algorithm [81], can be used without any increase in duration, peak power or SAR as in the case of multi-band RF pulses. Single-slice inversion, refocusing, small-tip-angle and large-tip-angle RF pulses can be directly used for multi-slice excitation without any modifications since the field profile is designed to produce locally linear gradient fields at the slice locations. Furthermore, techniques for improving single-slice pulse design, such as the VERSE algorithm [82], can be used in combination with the proposed methods for SAR reduction or time optimization.

The number of slices that can be excited with a single-band RF pulse, M, is limited by the number of gradient channels. For the 1PPS method, at least 3M-2 elements are necessary, whereas for the 2PPS method, 4M-2 elements are needed. Another option is to design a magnetic field such that multiple, spatially oscillating and wider linear gradient volumes can be obtained using a slightly modified field design method used in this study. Spatially oscillating, wider linear gradient fields can be combined with the multi-band RF pulses to increase the number of slices without increasing the number of channels. Moreover, the proposed method is valid only for thin slices (<5 mm) because the gradient fields are designed only at the center of the slice and the slice thickness error increases more rapidly for thicker slices. Spatially oscillating gradient fields in wider regions may be a solution for exciting multiple thicker slices with a single-band RF pulse or doubling the number of slices excited by a N-band RF pulse.

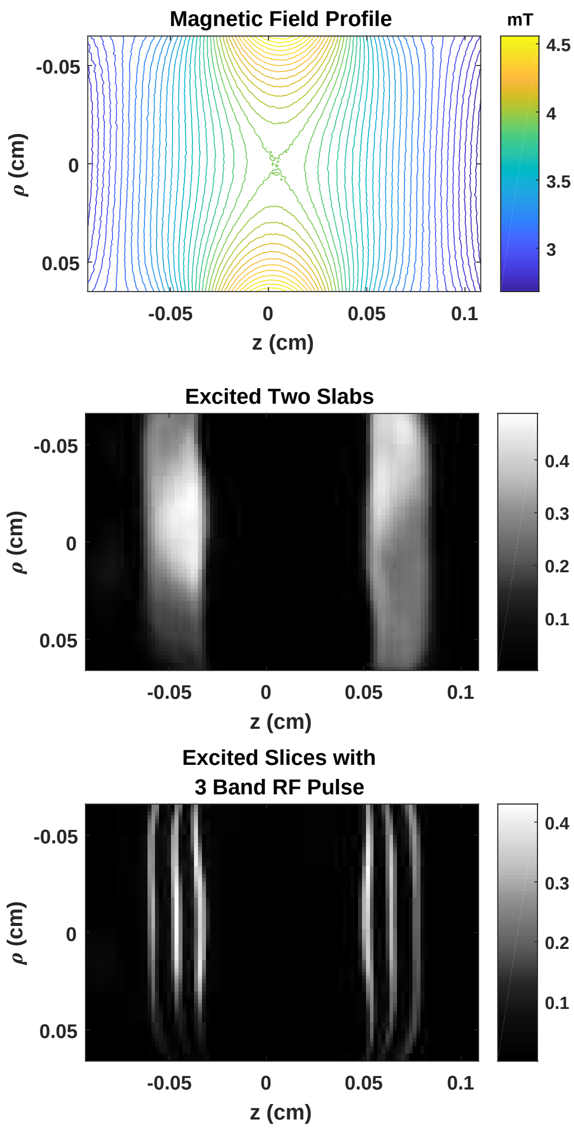

Figure 5.13: Experimental Results. **(a)**Magnetic field profiles **(b)** Coronal image demonstrating two slab excitations with a single band RF pulse. **(c)** 6-slice excitation with a 3 band RF pulse. 3 Hamming windowed sinc pulses with slightly different frequencies are superposed and applied.

5.5.2 Slice Profile Discrepancy

The 1PPS and 2PPS methods both have advantages and disadvantages. The slice thickness variation of the 1PPS method is greater compared with the 2PPS method for the same number of slices. The slice profiles become thinner with increasing radius, and the slice thickness variation is less in the center of the slice. In the case of a 3 slice excitation, only 53.5% of the overall volume can be covered by regularly shifted slices due to large variation near the edges. In order to cover the entire VOI, approximately three times more number of slice shifts are required which offset the advantages of SMS. Instead, this variation can be considered as tolerable for a centrally located region of interest. For example, 1PPS method can excite 95% of the VOI if diameter of the VOI is reduced to 5 cm. Region of interest does not have to be necessarily centrally located. Off-center design point selection as in Fig. 5.7 might help to obtain lower thickness variation in the smaller off-center volumes. This drawback of the 1PPS method is compensated for by its superior performance in G_{lim}, g, P_{diss} and B_{max} compared with the 2PPS method. In addition, the 1PPS method can achieve closer slice separations than the 2PPS method, as shown in Fig. 5.6. Therefore, the 1PPS method may be beneficial for the design of ultra-short RF pulses in exchange for increased slice thickness error and/or a reduction in the useful FOV in radial direction. In summary, 1PPS method is weak and not suitable for overall volume imaging; however, it can be preferred for VOIs with smaller radius considering its advantages over 2PPS method.

The simulated slice thickness variation for the 2PPS method is generally less than 5%, which is similar to the variation obtained with conventional gradients. Although it is possible to further decrease the slice thickness variation by using more design points per slice (higher L) and an increased number of channels, the overall system performance decreases dramatically with higher L. Slice thickness variations, overlaps and gaps between shifted slices can cause problems in covering the entire VOI. Accurate reconstruction strategies for overcoming slice discrepancies should be further investigated. For instance, algorithms considering slice profiles similar to SEMAC [83] might be adapted to the proposed method.

The agreement observed here between the expected and measured slice profiles validates the experimental procedure. There are possible reasons for the higher slice thickness variations in the experiments compared with the simulations. Firstly, flip angle was selected as 40° for a phantom. Steady state longitudinal magnetization before the RF pulse decreases to 86% of its initial value considering the T1 of the phantom and TR of the sequence; therefore, saturation effects can slightly increase the apparent slice thickness. Other possible reason is the imperfections in the home-built gradient coil array. In both the 1PPS and 2PPS methods, angular symmetry of the coils is assumed in the equations; however, the measured magnetic field maps of the manufactured coils are slightly tilted due to manufacturing imperfections. Consequently, the thickness variations in the lower half plane were not well controlled in these experiments since both design points were chosen to lie in the upper half plane. However, such thickness variations might still be acceptable.

5.5.3 Dynamic Adaptation of the Field Profile

Independent control of each array element enables the dynamic adaptation of the field profile. The 1PPS and 2PPS methods lead to 3M-2 and 4M-2 field constraints, respectively. The remaining degrees of freedom are utilized to minimize the norm of the current which also minimizes the P_{diss} in case of identical resistances. However, they can also be used to reduce the B_{max}, or the slice thickness variation or to increase the G_{max}. A lower B_{max} may result in less stored inductive energy and might better respect PNS limitations due to lower E fields and potentially higher slew rates. Additionally, the design point locations, which are important parameters affecting the slice thickness variation, center location variation and g, can be independently optimized for each slice location and VOI (see Fig. 5.7 and Fig. 5.8). Moreover, combination of constraints for the equal magnetic fields, first and second derivative of the fields can be used separately for different design points which can utilize the tradeoff between slice thickness variation, center location variation, and g according to design specifications. Although such optimizations have not been studied in detail, a higher number of degrees of freedom is promising for greater adaptability of the possible field profiles.

Unlike for a coil array, for conventional linear gradient coils, the specifications for the VOI, linearity error and gradient strength per unit current are determined at the beginning of design. The field profile cannot be changed after coil manufacture. However, there is a tradeoff between the VOI, the linearity error and the gradient strength specifications that may vary dramatically with different sequences, different target organs, or other factors. Furthermore, another advantage of dynamic adaptation of the field profile is to extend the useful VOI of the coil. For instance, if a conventional gradient coil were to be designed with the same physical dimensions and the same aspect ratio, reasonable homogeneity could be achieved in a volume of 15-20 cm in length in the z direction, whereas our coil array can excite slices even at the edge of the coil in a 27 $\times$ 15 cm cylindrical VOI.

5.5.4 Limitations

In addition to slice thickness variations, another significant limitation of our methods is the dramatic decrease in performance for smaller slice separations. Although the 1PPS method can achieve the excitation of closer slices than the 2PPS method, its performance decreases. The radius of the VOI is an important parameter affecting both the minimum slice separation and the tolerable slice thickness variation. Perhaps, a different hardware geometry would be required to further reduce the slice separation while maintaining performance. The target field method [84] might provide intuition for the required current density on the coil for a target magnetic field distribution specified on a cylindrical surface. For the angularly symmetric coils, current density and the magnetic field profile on a cylindrical surface are related by the spatial Fourier transform in the z-direction [84]. Application of our method for smaller slice separations forces desired field to contain higher spatial frequency content which implies higher spatial frequency content for the current density on the coil. Such a current distribution requires shorter array elements to realize rapidly varying, high frequency current distribution. Such a rapid variation in the current density also decreases the strength of the generated field inside the VOI; therefore, current requirement of the amplifiers would be increased significantly. Excitation of the closer slices can be considered as the main weakness of the study and requires further investigation.

There are also practical limitations regarding the extension of this work to clinical whole-body coil arrays. First, the current study needs to be extended to the excitation of slices in arbitrary orientations. This might be achieved with a more generalized array of coils. The angular symmetry assumption will fail for the generalized array of coils; therefore, more general formulations will be required. The generalized array of coils might also provide lower slice thickness variation and center location variation due to the increased degree of freedom in the system in all directions.

Chapter 6

Simultaneous Use of Linear and Nonlinear Gradients for B_1^+ Inhomogeneity Correction

The content of this chapter was published in NMR in Biomedicine [85]. The figures and tables in this paper is also used in this chapter. Some concepts involved in this chapter was also presented in the 22th Annual Meeting of International Society for Magnetic Resonance in Medicine [86] as well as the 32nd Annual Meeting of ESMRMB [87].

6.1 Introduction

In MRI, spatially selective excitation aims to excite the desired transverse magnetization distribution. For this purpose, the design of the RF pulse and gradients requires an inverse solution to the Bloch equation, which is still an open problem. In [88], the small tip angle approximation overcomes this problem by introducing the excitation k-space concept. In a reasonable design with L-SEMs, a k-space trajectory should cover significant energy in the Fourier transform of the target transverse magnetization distribution. Furthermore, high main field strengths (>1.5 T) have become desirable due to their high SNR [27]; however, B_1^+ inhomogeneity can degrade the image quality significantly [27,28]. RF shimming [29] and parallel transmission [30, 31] were proposed to mitigate B_1^+ inhomogeneity. Another method is to use a 3D RF pulse. In the excitation k-space framework, mitigation of B_1^+ inhomogeneity leads to a 3D target excitation pattern, which can be excited with a 3D excitation k-space approach. In a multi-dimensional target transverse magnetization scenario, energy in the excitation k-space spreads to multiple dimensions. Therefore, a reasonable excitation trajectory should cover most of the energy in the excitation k-space and should be dense enough to avoid aliasing, which results in an impractical RF pulse with very long durations. However, because the Fourier transform of the target transverse magnetization is unique, the selection and design of a reasonable k-space trajectory have only limited flexibility. In the literature, spoke excitation is generally used for slice selective B_1^+ inhomogeneity with either fixed spoke locations [32] or optimized spoke locations [33,34]. Although various trajectory choices exist, these trajectories are similar in terms of length, dimension and frequency weightings, which limits the degrees of freedom in the RF pulse optimization. Possible solutions for increasing the degrees of freedom in the multi-dimensional RF pulse design problem should be investigated. Additional degrees of freedom can lead to more homogeneous excitation profiles and shorter RF pulse durations for more off-resonance robustness and shorter echo times.

One way of obtaining additional degrees of freedom is by using N-SEMs and L-SEMs in RF pulse design problems. The Fourier transform relationship between the excitation k-space and transverse magnetization distribution is broken with the addition of an independent N-SEM channel since N-SEMs and L-SEMs are coupled via spatial variables. Some studies that include the phase accumulation due to N-SEM channels in the RF pulse design problem already exist [89, 90]. Some other studies explicitly define the excitation k-space variables for N-SEMs, which satisfies the Fourier transform relationship between the excitation k-space and transverse magnetization distribution under special conditions [35, 91]. In our study, the independent excitation k-space dimension for each N-SEM is defined when they are simultaneously used with L-SEMs. Furthermore, the Fourier transform relation between the excitation k-space in higher dimensions (>3) and transverse magnetization distribution is re-established with the formulations in the general case of the simultaneous use of L-SEMs and N-SEMs. It is also shown that an increase in the dimension of the excitation k-space can lead to an infinite number of different trajectories.

This chapter provides an excitation k-space formulation for the simultaneous use of L-SEMs and N-SEMs in the RF excitation problem. The proposed formulation demonstrates the increase in the degrees of freedom with higher dimensional Fourier transform. An increase in the degrees of freedom is demonstrated for a slice selective B_1^+ inhomogeneity correction problem using 3 spoke locations. Comparisons of the use of only L-SEMs, the use of only N-SEMs and their simultaneous use are presented for slice selective 1D and 2D (RF power unlimited and limited) simulations, as well as for slice selective 2D experiments.

6.2 Theory

In [88], an analytical expression for the excitation profile for a given RF and gradient waveforms is provided as follows:

$$M_{xy}(\mathbf{r}) = i\gamma M_0 \int_0^T B_1(t) e^{-i\gamma \mathbf{r}\cdot\int_t^T \mathbf{G}(s)ds} dt \tag{6.1}$$

Here, definitions of various variables are adapted to be consistent with N-SEMs. $\mathbf{r} = [x/x_{VOI}\ \ y/y_{VOI}\ \ z/z_{VOI}]$ is a unitless vector of the normalized spatial coordinates, which are the physical spatial coordinates divided by the length $(x_{VOI}, y_{VOI}, z_{VOI})$ of the VOI in the respective dimensions. $\mathbf{G}(s) = [G_x(s)x_{VOI}\ G_y(s)y_{VOI}\ G_z(s)z_{VOI}]$ is a vector of gradient temporal dependencies multiplied by the VOI in the respective dimension. M_0 is the initial longitudinal magnetization, γ is the gyromagnetic ratio, $B_1(t)$ is the time envelope of the transmit signal, and T is the duration of the RF pulse. Although Eq. 6.1 assumes that B_1^+ is spatially homogeneous, the spatial dependency of B_1^+ will later be included by assuming spatiotemporal separability. Further algebraic steps in reference [88] establish a Fourier transform relationship between the RF pulse and excitation profile as in Eq. 6.2:

$$M_{xy}(\mathbf{r}) = i\gamma M_0 \int_K W(\mathbf{k}) S(\mathbf{k}) e^{i2\pi r\cdot\mathbf{k}} d\mathbf{k} \tag{6.2a}$$

$$S(\mathbf{k}) = \int_0^T {}^3\delta(\mathbf{k}(t) - \mathbf{k}) \left|\dot{\mathbf{k}}(t)\right| dt \tag{6.2b}$$

$$\mathbf{k}(t) = -\frac{\gamma}{2\pi}\int_0^T \mathbf{G}(s) ds \tag{6.2c}$$

$$W(\mathbf{k}(t)) = 2\pi B_1(t) / \left|\gamma \mathbf{G}(t)\right| \tag{6.2d}$$

where $W(\mathbf{k}(t))$ is the spatial frequency weighting function and $S(\mathbf{k})$ is the sampling function. The excitation k-space concept is introduced for only L-SEMs by assuming that the k-space trajectory does not cross itself. The k-space variables are also unitless because normalized spatial coordinates are used in this study.

N-SEMs can be included in the above equations with a slight manipulation of the derivation. To simplify the equations for better visualization, only one additional N-SEM is considered in the formulation; however, generalization to multiple N-SEMs is trivial. Under the assumption of spatiotemporal separability, the $\hat{z}$ component of the magnetic field produced by the nonlinear gradient coil can be written as $u(r)G_u(t)$. To be consistent with the L-SEMs, $u(r)$ is also a unitless, normalized spatial dependency of the N-SEM, such that the difference between the maximum and minimum values is 1 within the field-of-view. $G_u(t)$ is the temporal dependency of the magnetic field strength. Addition of the N-SEM together with the small tip angle approximation results in:

$$M_{xy}(\mathbf{r}) = i\gamma M_0 \int_0^T B_1(t) e^{-i\gamma \mathbf{r}\cdot\int_t^T \mathbf{G}(s)ds + u(r)\int_t^T G_u(s)ds} dt \tag{6.3}$$

Here, because $u(r)$ is a function of the other spatial variables, a completely independent k-space variable for N-SEM cannot be introduced. Inserting a delta function into Eq. 6.3 and introducing an independent dummy space variable, u, leads to Eq. 6.4.

$$M_{xy}(\mathbf{r}) = i\gamma M_0 \int_{-\infty}^{-\infty}\int_0^T \delta(u(r) - u) B_1(t) e^{-i\gamma\tilde{\mathbf{r}}\cdot\int_t^T \tilde{\mathbf{G}}(s)ds} dt \tag{6.4}$$

In Eq. 6.4, $\tilde{r} = [x/x_{VOI}\ y/y_{VOI}\ z/z_{VOI}\ u]$ is a vector of regular normalized Cartesian coordinates concatenated with the dummy space variable u. $\tilde{G}(s) = [G_x(s)x_{VOI}\ G_y(s)y_{VOI}\ G_z(s)z_{VOI}\ G_u(s)]$ is the vector of temporal dependencies for both L-SEMs and the N-SEM. Application of the same algebraic procedure in the derivation of Eq. 6.2 from Equation Eq. 6.1 yields:

$$M_{xy}(\mathbf{r}) = i\gamma M_0 \int_{-\infty}^{-\infty} \delta(u(r) - u) \int_K W(\tilde{\mathbf{k}}) S(\tilde{\mathbf{k}}) e^{i2\pi\tilde{\mathbf{r}}\cdot\tilde{\mathbf{k}}} d\tilde{\mathbf{k}} du \tag{6.5a}$$

$$S(\tilde{\mathbf{k}}) = \int_0^T {}^4\delta(\tilde{\mathbf{k}}(t) - \tilde{\mathbf{k}}) \left|\dot{\tilde{\mathbf{k}}}(t)\right| dt \tag{6.5b}$$

$$\tilde{\mathbf{k}}(t) = -\frac{\gamma}{2\pi} \int_0^T \tilde{\mathbf{G}}(s) ds \tag{6.5c}$$

$$W(\tilde{\mathbf{k}}(t)) = 2\pi B_1(t) / \left|\gamma \tilde{\mathbf{G}}(t)\right| \tag{6.5d}$$

In Eq. 6.5, the addition of an N-SEM channel increased the dimension of the excitation k-space to four, while the conventional excitation k-space is three-dimensional in Eq. 6.2. Eq. 6.5 further suggests that the k-space variable corresponding to the N-SEM channel can be treated as an independent k-space variable. Therefore, design can be performed for the four-dimensional spatial frequency weighting function, $W(\tilde{\mathbf{k}}(t))$, sampled at the four-dimensional trajectory, $S(\tilde{\mathbf{k}})$.

Eq. 6.5 can be utilized in two different ways. Firstly, if the RF and gradient waveforms are known, the four-dimensional excitation k-space can be constructed. Clearly, a 4D inverse Fourier transform of the excitation k-space is a function of the three conventional spatial variables x, y, z and the additional dummy space variable u. In this case, the resulting transverse magnetization will be the 4D inverse Fourier transform of the excitation k-space, calculated only at the points lying on $\delta(u(r) - u)$, which is an expression of the 3D object in a 4D space.

The second and more beneficial approach would be to design an excitation k-space for a desired transverse magnetization distribution. In a 4D space, a 3D target excitation distribution can be mapped onto $\delta(u(r) - u)$. Afterwards, the 4D space can be filled freely at all points except the ones on $\delta(u(r) - u)$ since

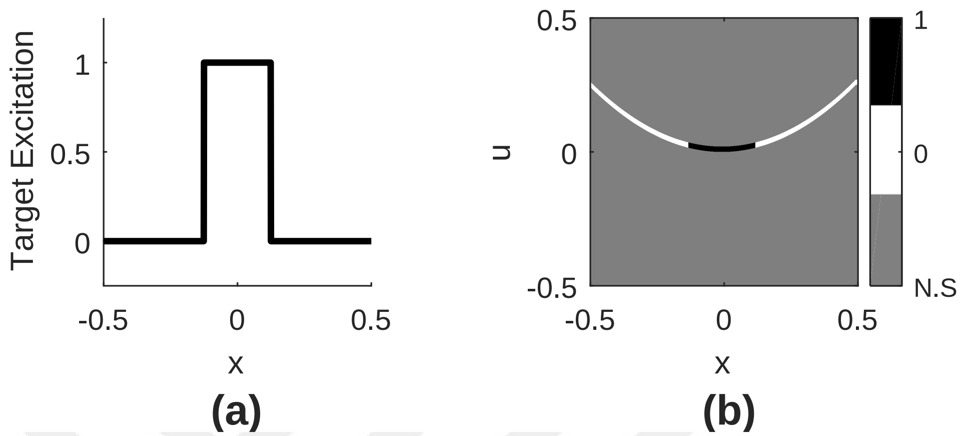

Figure 6.1: An example target excitation demonstrating a regular slice selection with simultaneous use of x and x^2 gradients. (a) 1D normalized target excitation profile. (b) Target excitation profile mapped onto $\delta(u-x^2)$. Gray regions in the $u-x$ plane are not constrained by the excitation profile. N.S stands for "not specified".

only the values on the object, $\delta(u(r)-u)$, determines the actual excitation profile. Depending on how the 4D space is filled, its Fourier transform, which determines the multiplication of $W(\tilde{\mathbf{k}}(t))$ and $S(\tilde{\mathbf{k}}(t))$, can be manipulated to better fit the design criteria. Therefore, the ability to change the Fourier transform of the 4D space can lead to infinitely many different k-space trajectories and spatial frequency weighting functions with the same excitation profile. Smart design of the 4D space might fulfill different excitation criteria, such as short k-space trajectories or low RF power excitation pulses.

To explain the freedom, a target excitation problem is considered in 1D. Fig. 6.1a shows the target excitation profile for a line object. One linear gradient (x-SEM) and one nonlinear gradient (x^2-SEM) are considered to excite the target excitation profile on the line object. Notably, although the x^2-gradient is not suitable for the Maxwell equations in the 3D volume, it is physically realizable on the y=z=0 line. In Fig. 6.1b, the target excitation profile is mapped onto a parabola defined by $\delta(u-x^2)$. For the design goals, only the values on the parabola in the u-x plane are specified, and the values on the rest of the plane can be chosen freely without altering the target excitation. In Fig. 6.2a,

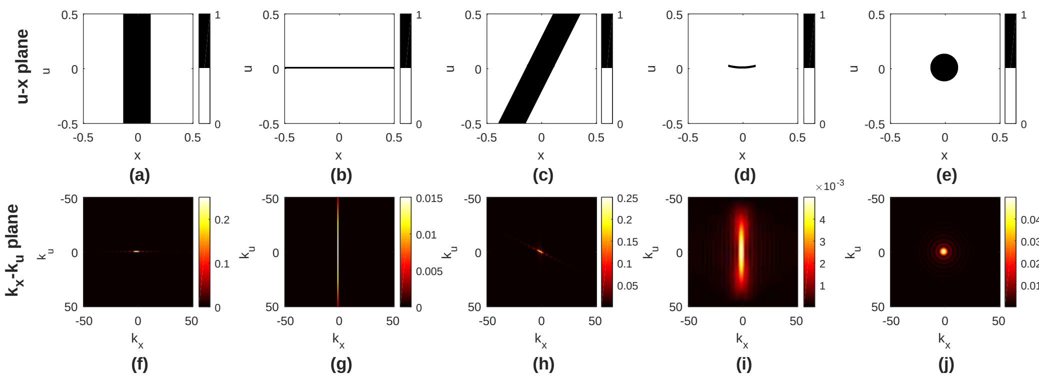

Figure 6.2: $u - x$ plane approach to demonstrate that many different excitation k-spaces (second row) can be used to excite same transverse magnetization distribution in Fig. 6.1a. **(a-e)**: The gray region in Fig. 6.1b is filled freely with different distributions that vary as a function of only linear variable (a), only nonlinear variable (b), or specific combination of linear and nonlinear variables. (c) The entire gray region in Fig. 6.1b is set to 0 (d), and only the circular region at the center is set to 1. **(f-j)**: Fourier transformations of the constructed $u - x$ plane distributions to demonstrate the excitation k-spaces in the increased dimension.

the $u - x$ plane is constructed using this freedom such that it does not have any variation in the nonlinear axes. The corresponding excitation k-space in Fig. 6.2f contains samples only on the kx-axis, which demonstrates the use of only L-SEM. Alternately, the u-x plane in Fig. 6.2b does not have any variation in the linear direction, which results in 1D excitation k-space samples only on the ku-axis (Fig. 6.2g) while using only the N-SEM. In Fig. 6.2c and Fig. 6.2h, the $u - x$ plane is constructed such that it does not vary in the direction of a specific axis. Therefore, the Fourier transform is again squeezed into one dimension, which allows the use of a 1D k-space trajectory and requires the use of both x and x^2-SEMs. In Fig. 6.2d, all of the unspecified regions are set to 0, resulting in a Fourier transform in Fig. 6.2i that requires a longer trajectory but with lower frequency weightings. Similarly, Fig. 6.2e and Fig. 6.2j show an example design that is suitable for a concentric ring-shaped trajectory. Thus, Fig. 6.2 demonstrates that the Fourier transform of the target transverse magnetization can be altered by filling the unrestricted regions in the $u - x$ plane. This freedom can lead to various excitation k-space trajectories that differ in dimensionality, energy or length, which lead to exactly the same excitation profile in space.

To extend the previous example to a multi-dimensional excitation problem, B_1^+ inhomogeneity correction as well as slice selection are investigated using L-SEMs and an N-SEM together. Spoke excitation is a suitable choice for such a design purpose. In the conventional spoke excitation, the best spoke locations can be optimized in a 2D excitation k-space to correct the 2D B_1^+ inhomogeneity. On the contrary, spoke excitation with the simultaneous use of L-SEMs and an N-SEM provides a 3D excitation k-space to correct 2D B_1^+ inhomogeneity, which increases the degrees of freedom in the design problem. Assuming a small tip angle and spatiotemporally separability of the B_1^+ field, the optimization problem can be written as:

$$min\left(\int\int_{ROI}\left|1-\left|b_1(x,y)\sum_{n=1}^{N}a_n e^{j2\pi(k_{xn}x+k_{yn}y)+k_{un}u(x,y))}e^{-j\gamma(N-n)\Delta B_0(x,y)\Delta T}\right|\right|^2 dxdy\right) \tag{6.6a}$$

$$b_1(x,y)=B_1(x,y)/\int\int_{ROI}|B_1(x,y)|\,dxdy \tag{6.6b}$$

where $b_1(x,y)$ is the normalized B_1^+ distribution in the slice, an is the normalized amplitude of the n^{th} spoke, $\Delta B_0(x,y)$ is the B_0 inhomogeneity term, ΔT is the time between the consecutive RF pulses, $u(x,y)$ is the magnetic field profile of the nonlinear channel, and k_{xn}, k_{yn}, and k_{un} are the k-space location coordinates for the n^{th} spoke. Even if the field profile of the nonlinear gradient coil is a three-dimensional function, it can be considered as a two-dimensional function by assuming thin slice selection with the spoke excitation.

Although SAR is not considered in the optimizations except for a set of 2D simulations, a parameter P is defined as the sum-of-squares normalized spoke amplitude to evaluate the SAR performance. Because SAR is proportional with the time integral of the squared RF pulse amplitude and identical RF pulse waveforms are used for all spokes independent of the spoke number, P is also proportional with the SAR.

$$P=\sum_{1}^{N}|a_n|^2 \tag{6.7}$$

No flip angle compensation corresponds to one spoke with amplitude 1 ($a_1 = 1$). This is called the uncorrected case and leads to a P value of 1. When multiple spokes are used to correct the excitation profile, P also indicates the ratio of the SAR for uncorrected and corrected sequences for the same average flip angle. Because RF pulse waveforms and durations are considered to be identical for all spokes independent from the spoke number, the P parameter does not consider the tradeoff that SAR would decrease if an RF pulse for the one-spoke excitation was allowed to have the same duration in a multiple-spoke excitations. In RF power-limited 2D simulations, P is bounded by 1, which ensures that RF power does not increase for the corrected excitation profile with respect to the uncorrected excitation.

6.3 Methods

To demonstrate the advantage of using an additional N-SEM for B_1^+ inhomogeneity correction, 3 cases are compared: L-SEMs alone, the N-SEM alone and both sets of fields simultaneously. This comparison is performed using 1D and 2D simulations as well as an experimental study on a phantom.

6.3.1 Optimizations

Optimizations use the structure in Eq. 6.6. In all of the optimization problems, the number of spokes, N, is chosen as 3 to limit the duration of the excitation pulse. Because inhomogeneity correction is only performed for the amplitude of the excitation, relative positions of the spokes are not important, and therefore one spoke location can be chosen arbitrarily. In our design, the first spoke is placed at the origin. 2 spoke locations and the complex weightings of the 3 RF pulses are optimized. The B_0 inhomogeneity is ignored in the simulations but considered in the experiments. As a performance measure for each case, a reduction in the flip angle inhomogeneity is defined as $(1 - \sigma_{corrected}/\sigma_{uncorrected})$, where $\sigma_{corrected}$ and $\sigma_{uncorrected}$ indicate the standard deviations of the normalized flip angle map for uncorrected and corrected cases, respectively.

In 1D simulations, a B_1^+ inhomogeneity profile is generated as a quadratic function of x, as in Fig. 6.1, to demonstrate the advantage of simultaneous use of L-SEM and N-SEM. The only available gradients are x and $u(r) = x^2$ gradients. Therefore, while using only the L-SEM, the spoke locations are optimized on only the k_x line. Similarly, while using only the N-SEM, spoke locations are optimized on the k_u line; however, while simultaneously using L-SEM and N-SEM, spoke locations are optimized in a plane defined by the k_x and k_u lines.

For 2D simulations, the N-SEM dependency is assumed to be x^2+y^2. For only L-SEM, spoke locations are determined in the plane defined by k_x and k_y. For only N-SEM, spoke locations are on the k_u line. For simultaneous use, spokes are placed on a three-dimensional volume defined by k_x, k_y and k_u. For RF power-constrained simulations, P values are limited by 1, which corresponds to the same RF power as for one-spoke excitation. In the experiments, free optimization parameters are the same as those in 2D simulations except that B_0 inhomogeneity is also accounted for.

Optimizations are performed in MATLAB 2014b (Mathworks Inc., Natick, MA). The built-in MATLAB function "GlobalSearch" has been used. The algorithm uses the "Scatter Search Algorithm" to select multiple starting points at different basins of attraction from the given initial value. A predefined local solver operates on each starting point to find the global optimum. Further details on the algorithm are explained in [92]. Another built-in function, "fmincon", is used with the "interior point algorithm" as a local solver. In the optimizations, an initial point that is chosen as zero is used as an initial guess for the first local solver call. The performance of the method is sensitive to the initial guess; however, the generation of many trial points decreases its effect. In the simulations, the amplitude of each RF pulse is limited to 5, and normalized k-space locations are bounded between -10 and 10. The maximum number of trial points is defined as 1000, which is also the stopping criterion. In the experiments, the maximum duration of the optimization is limited to 100 seconds as an additional stopping criterion.

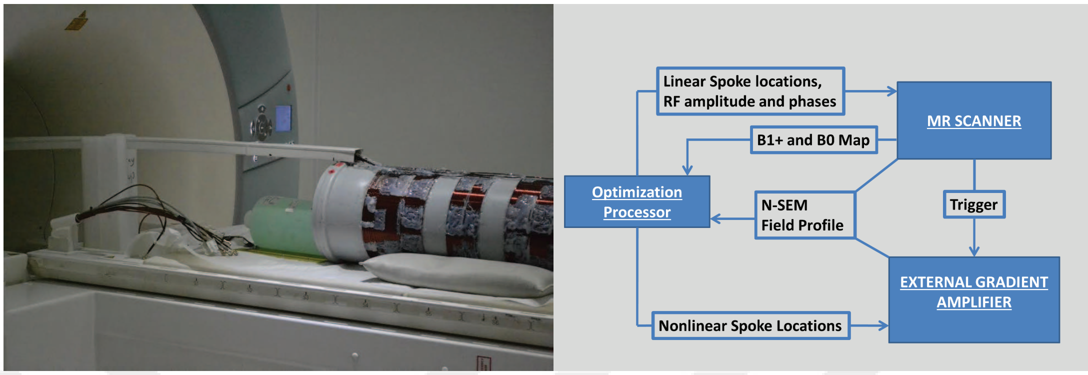

(a) (b)

Figure 6.3: Experimental setup and procedure.**(a)** Placement of the Siemens phantom and the nonlinear gradient coil. The nonlinear gradient coil has 3 independent channels with 60, 30 and 60 turns; however, only the closest channel to the phantom is used. **(b)** Schematic diagram for the experimental procedure.

6.3.2 Experiments

Experiments are conducted using a 3T scanner (Magnetom Trio A Tim, Siemens) with a Siemens phantom. For the experiments, a custom-made nonlinear gradient coil is manufactured. Although the nonlinear gradient coil has 3 independent channels as in Fig. 6.3a, only one channel with 60 turns is used since the aim of the paper is to demonstrate the increase in the degree of freedom even with the addition of one N-SEM. However, extension to multiple channels can be trivially considered by increasing the computational cost of the optimization. The nonlinear gradient coil is wound on a plastic cylinder with a diameter of 20 cm, and the wire diameter is 2.1 mm. The loops are in the circumferential direction, which cancels the net torque. The phantom is placed next to the coil, as in Fig. 6.3a. The nonlinear gradient coil is driven with an external gradient amplifier (GA-300 amplifier, Performance Controls Inc., Montgomeryville, PA), which is controlled by a signal generator. The feed cables for the gradient coil are connected to the Faraday cage with a 10-nF filter capacitor to shield the RF noise. Inside the scanner bore, feed cables are kept parallel to B0; therefore, there is no force experienced by the feed cables, and the current on these wires does not contribute to the magnetic field in the z-direction.

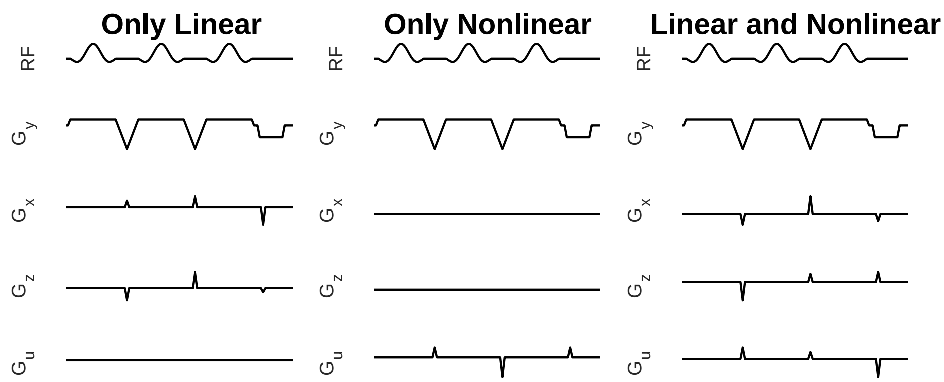

Figure 6.4: Sequence diagrams for 3 cases. Each has 3 apodized sinc pulses (3 spokes) with slice selection in the y-direction. Slice selection is always performed with a positive gradient (flyback trajectory). Between the RF pulses, other linear and nonlinear gradients are used for the multi-dimensional excitation trajectory. For all cases, the phase and amplitude of the RF pulses as well as gradient blips are optimized. The proposed technique in this study is the simultaneous use of linear and nonlinear gradients (3rd row).

Considering the experimental procedure in Fig. 6.3b, some pre-scans are required at the beginning of the experiment. First, a B_0 map is acquired using the phase difference between two GRE images with different echo times. A custom-built RF transmit and receive coil with rectangular shape is tuned and matched with distributed capacitors. The B_1^+ map of the RF coil is acquired with a Bloch-Siegert-shift based sequence [93]. The magnetic field profile of the nonlinear gradient coil is measured from the phase difference between a reference GRE image and another GRE image with the same echo time and small blip of current applied to the nonlinear gradient coil during the phase encoding. Alternatively, if the object location relative to the coil is known, the spatial dependency of the magnetic field produced by the nonlinear gradient coil can be calculated using the Biot-Savart law. After obtaining the required B_0, B_1 and gradient coil field maps, the RF and spoke parameters are optimized. The amplitudes and phases of the RF pulses, together with the linear gradient moments for spoke locations, are used by the scanner. The control circuit of the external gradient amplifiers is programmed according to the required nonlinear gradient waveform, which is determined by the k_u component of the spoke locations.

For the comparison of the three different cases, corresponding pulse sequences in Fig. 6.4 are used. Between the RF pulses, x, z and u gradients are used to realize the required spoke locations. As in previous work [94], the slice selection gradients are always positive during the RF pulse, orienting the spokes in the same direction and making the excitation robust to B0 inhomogeneity and eddy current effects during the RF pulses. The duration of each RF pulse is 1.5 ms, and the time between the RF peaks is 2.94 ms. All input maps and resulting sequence maps are acquired with 128 x 128 resolution in a 2.5-mm-thick coronal slice with a FOV of 25 cm for both dimensions. Flip angle maps are obtained by using the double angle method with average flip angles of 35° and 70° and a TR of 2.5 seconds.

6.4 Results

The results of this study are presented in subcategories: 1D simulations, 2D simulations and experimental results. Detailed information about the standard deviation of the resulting excitation profiles, P, k-space locations and RF parameters are provided in Table 1 for all of the simulations and the experiment.

6.4.1 1D Simulations

In Fig. 6.5f, the yellow plot shows an example B1 inhomogeneity profile in one dimension. An ideal excitation profile with perfect homogeneity is shown with the dashed line. After optimization for 3 different cases, corrected excitation profiles are also provided in Fig. 6.5f. As previously explained, the u-x plane approach can provide another interpretation of the results. The target excitation profile, which is the inverse of the B_1 profile, is mapped onto $\delta(u - x^2)$ in Fig. 6.5a. All other values except the parabola in the $u - x$ plane are not constrained by the actual problem. However, using only L-SEMs or the N-SEM leads to spoke locations only at the k_x line or the k_u line, respectively, as shown in Fig. 6.5e. This situation causes one-dimensional variations in the $u - x$ plane for the respective

Table 6.1: The standard deviation (σ), P, optimized RF parameters and k-space locations for all spokes are provided. S1, S2 and S3 represent the first, second and third spokes, respectively.

	Only linear				Only nonlinear				Linear + nonlinear			
1D	σ		0.021		σ		0.128		σ		0.005	
	P		1.03		P		0.95		P		2.34	
		S1	S2	S3		S1	S2	S3		S1	S2	S3
	$\|a_n\|$	0.13	1	0.11	$\|a_n\|$	0.94	0.18	0.19	$\|a_n\|$	1.02	0.81	0.8
	$\angle a_n$	0	1.79	0.44	$\angle a_n$	0	1.36	1.80	$\angle a_n$	0	2.06	2.78
	k_x	0	−1.62	−4.34	k_x	0	0	0	k_x	0	−1.00	−0.49
	k_{x^2}	0	0	0	k_{x^2}	0	4.39	−3.98	k_{x^2}	0	−0.96	−2.10
2D (RF power unlimited)	σ		0.097		σ		0.329		σ		0.021	
	P		1.09		P		15.17		P		2.53	
		S1	S2	S3		S1	S2	S3		S1	S2	S3
	$\|a_n\|$	0.55	0.67	0.58	$\|a_n\|$	2.48	1.06	2.81	$\|a_n\|$	1.33	0.13	0.86
	$\angle a_n$	0	1.43	1.35	$\angle a_n$	0	3.43	3.38	$\angle a_n$	0	5.75	4.50
	k_x	0	−0.72	−0.29	k_x	0	0	0	k_x	0	−0.16	0.28
	k_y	0	0.33	0.89	k_y	0	0	0	k_y	0	0.77	−0.25
	$k_{x^2+y^2}$	0	0	0	$k_{x^2+y^2}$	0	−2.67	−0.18	$k_{x^2+y^2}$	0	0.29	−0.59
2D (RF power limited)	σ		0.097		σ		0.329		σ		0.035	
	P		1.00		P		1.00		P		1.00	
		S1	S2	S3		S1	S2	S3		S1	S2	S3
	$\|a_n\|$	0.61	0.60	0.52	$\|a_n\|$	0.77	0.33	0.55	$\|a_n\|$	0.60	0.47	0.64
	$\angle a_n$	0	5.75	4.50	$\angle a_n$	0	1.07	0.00	$\angle a_n$	0	5.15	6.06
	k_x	0	−0.41	−0.75	k_x	0	0	0	k_x	0	0.59	0.16
	k_y	0	−0.55	0.32	k_y	0	0	0	k_y	0	−0.59	−0.27
	$k_{x^2+y^2}$	0	0	0	$k_{x^2+y^2}$	0	2.07	−1.55	$k_{x^2+y^2}$	0	−1.36	−0.55
Experiment	$\sigma_{expected}$		0.119		$\sigma_{expected}$		0.142		$\sigma_{expected}$		0.095	
	$\sigma_{measured}$		0.143		$\sigma_{measured}$		0.158		$\sigma_{measured}$		0.120	
	P		1.11		P		1.31		P		1.25	
		S1	S2	S3		S1	S2	S3		S1	S2	S3
	$\|a_n\|$	0.16	1.02	0.21	$\|a_n\|$	0.41	0.92	0.54	$\|a_n\|$	0.20	0.20	1.08
	$\angle a_n$	0	3.68	2.75	$\angle a_n$	0	2.45	0.40	$\angle a_n$	0	2.70	2.48
	k_x	0	−1.62	−0.13	k_x	0	0	0	k_x	0	0.34	−0.78
	k_z	0	−3.54	−0.65	k_z	0	0	0	k_z	0	−1.47	−1.63
	k_u	0	0	0	k_u	0	−0.09	−0.43	k_u	0	0.06	−0.65

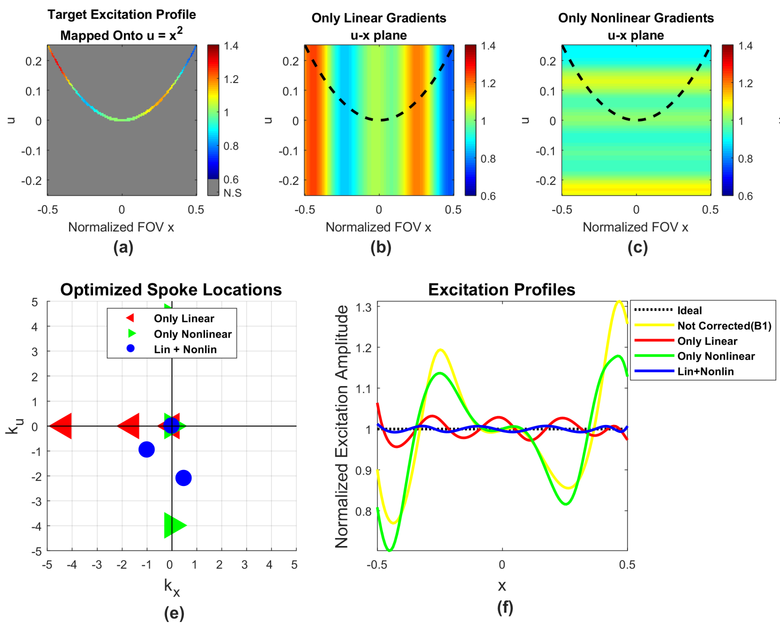

Figure 6.5: 1D Simulation Results **(a)** 1D Target excitation profile is mapped onto $\delta(u - x^2)$. N.S stands for "Not Specified". **(b-d)**: The resulting distributions in the $u-x$ plane after optimization for only linear, only nonlinear and simultaneous use of both, respectively. Only the values on the dashed parabolas correspond to actual correction. **(e)** Spoke locations for three different cases, including the central spoke for each case. **(f)** Uncorrected excitation profile due to B1 inhomogeneity (yellow), ideal perfectly homogeneous excitation profile (black-dashed), corrected with only L-SEMs (red), corrected with only the N-SEM (green), and corrected with simultaneous use of L-SEMs and the N-SEM (blue).

cases in Fig. 6.5b and Fig. 6.5c, which is possibly suboptimal. In contrast, the simultaneous use of L-SEM and N-SEM allows arbitrary variation in the entire $u-x$ plane, as in Fig. 6.5d. Another approach using the same degrees of freedom is shown in Fig. 6.5e, where spoke locations for the simultaneous L-SEM/N-SEM excitation can be placed over the entire two-dimensional $k_x - k_u$ plane.

In the 1D simulations, the standard deviations of the excitation profile from unity are 0.14, 0.021, 0.128, and 0.005 for uncorrected, corrected with only L-SEMs, only N-SEM and simultaneous use, respectively. Using only L-SEMs provides an 85% reduction in the flip angle inhomogeneity. Because optimization with only L-SEMs results in a higher spoke location, a high-frequency oscillatory excitation profile is observed in Fig. 6.5f. The use of only N-SEM yields poor performance with an insignificant (7%) reduction in the inhomogeneity. The reason for such a poor improvement is that the x^2 field profile can only perform symmetrical correction around 0, which does not match with the inverse of the B_1^+ profile. Simultaneous use almost ideally corrects the B_1^+ inhomogeneity, with a 96% reduction in the inhomogeneity.

In this example, using only the N-SEM provides almost no correction. Using only L-SEMs significantly corrects the excitation profile; however, simultaneous use leads to a 4-times lower standard deviation of the excitation profile with almost perfect correction.

6.4.2 2D Simulations

2D simulations aim to demonstrate that the advantage of simultaneously using L-SEMs and N-SEM is also valid for a more realistic scenario involving B_1 inhomogeneity correction as well as slice selection. Example B_1 inhomogeneity is assumed as in Fig. 6.6a. Fig. 6.6b-6.6d shows the resulting corrected excitation profiles for only L-SEMs, only the N-SEM and simultaneous use, respectively. Furthermore, for the same B_1 inhomogeneity, RF power limited simulations have been performed, and the P value is upper bounded by 1, which corresponds to 1-spoke or uncorrected excitation. Resulting homogeneity and RF power levels as well as spoke locations are shown in Table 6.1. Simultaneous use performed better than only L-SEMs and only the N-SEM for both RF power-limited and RF power-unlimited sets. Similar to the 1D simulation, the use of only the N-SEM provides poor correction of the excitation profile. For both RF power-limited and power-unlimited cases, although the excitation profiles differ slightly, standard deviations inside the ROI are the same if only L-SEMs or only the N-SEM are considered. For simultaneous use, a limitation on the RF power causes a slight increase in the inhomogeneity of the excitation profile. However, the RF power limitation does not affect the homogeneity correction performance significantly while decreasing the RF amplitudes for each case. In 2D simulations, the standard deviation of B_1^+ inhomogeneity was 45%. For both the RF power-unlimited

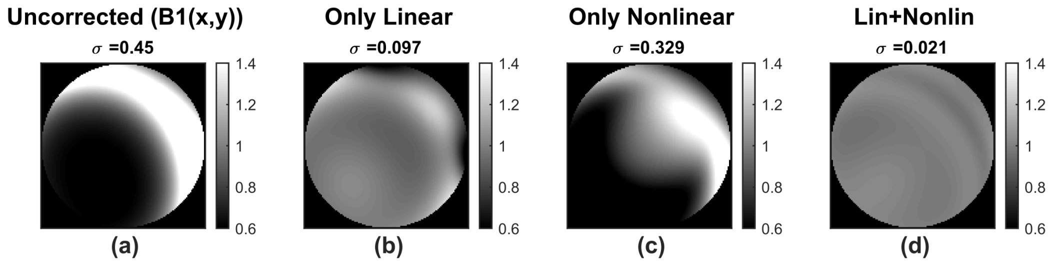

Figure 6.6: 2D simulation results. Available gradients are x, y, $x^2 + y^2$. **(a)** Example B1 inhomogeneity (uncorrected excitation profile) **(b-d)**: Comparison of resulting excitation profiles corrected with only L-SEM, only N-SEM and simultaneous use of both. RF power-limited solutions are presented in this figure.

and RF power-limited sets, the standard deviations are reduced by 78% and 27% for only L-SEMs and only the N-SEM, respectively. For simultaneous use, the standard deviation decreased by 95% and 92% for the RF power-unlimited and RF power-limited cases. Although the RF power-limited and RF power-unlimited cases result in different spoke locations and RF amplitudes, the final standard deviations are almost the same for only L-SEMs or only the N-SEM. This is an indication that there might be multiple optimal solutions for each case. All three cases show that when P is included in the optimization, there can still be solutions that provide near-optimal standard deviations. For the RF power-unlimited case, P is increased to 1.1, 15.2 and 2.5 for only L-SEMs, only the N-SEM and simultaneous use, respectively. When the P values are limited by 1, each case resulted in a P value of 1. Expectedly, the solution of the optimization problem resulted in the highest possible P value since an increase in the RF power can result in decreased inhomogeneity [95]. Alternatively, a P criterion can be inserted into the cost function with an adaptable weighting to provide a tradeoff between RF power and homogeneity.

To give a sense of understanding regarding the required computational power for the optimization problems, the details are provided for 2D RF power-unlimited cases as an example. For each method, generation and analyses of 1000 trial points are accomplished in 410, 614 and 462 seconds for only L-SEMS, only the N-SEM and simultaneous use, respectively. The global search algorithm does not always run local solvers at the trial points. The trial points can be rejected according to basin, score and constraint filters. Therefore, the number of local solver calls are 67, 60 and 57 for only L-SEMS, only the N-SEM and simultaneous use, respectively. Furthermore, the first local solution at the initial guess resulted in the best score among all trial points for only the L-SEM case. Therefore, other trials points could not improve the results, although most of the optimization times are dedicated to generation and analyses of the trial points. For only N-SEMs, the best score is found among the first 200 trial points, and it resulted in an insignificant decrease of 1.5% of the local minimization at the initial guess. However, the solution for simultaneous use is improved several times in the first 671 trial points, and the cost function value of the local minimizer at the initial guess decreased to 99.7% at the end of the optimization.

Fig. 6.7 shows the advantage of simultaneously using L-SEMs and the N-SEM with the resulting $u-x-y$ distributions for the same data as Fig. 6.6. In Eq. 6.5, $u(r)$ is considered as $x^2 + y^2$. The inverse of the $B_1(x, y)$ distribution is called the target correction profile, and it is used to obtain the homogenous excitation profile after the correction. In the $u - x - y$ volume approach, the target profile is mapped onto $\delta(u - x^2 - y^2)$, and only the first quadrant is shown in Fig. 6.7a. In Fig. 6.7a, only the values on $\delta(u - x^2 - y^2)$ are the design criterion, and the entire volume except for $\delta(u - x^2 - y^2)$ can be filled freely without affecting the excitation. However, the excitation k-space can be completely different depending on how the free space is filled. In Fig. 6.7b, spoke locations are restricted to the $k_x - k_y$ plane for only L-SEMs. Fig. 6.7c shows the resulting $u - x - y$ volume distribution, which is also the Fourier transform of the excitation k-space in three dimensions. Only the values on the paraboloid correspond to the actual excitation. However, there is no variation in the u-direction due to the restriction of spokes to the $k_x - k_y$ plane, which limits the flexibility of the excitation. In Fig. 6.7d, optimized spoke locations are on the k_u line for the correction with only the N-SEM. In Fig. 6.7e, there is no variation in the x- or y-direction, which limits the correction to being equal at each circle. In Fig. 6.7f, spokes are located in the entire three-dimensional volume, defined by $k_x - k_y - k_u$, by using the L-SEMs and N-SEM together. Therefore, in the corresponding $u - x - y$ volume distribution, variations in all directions are visible, as in Fig. 6.7g, and the actual correction on the paraboloid is a better approximation to the target correction in Fig. 6.7a.

6.4.3 Experiments

In the experiments, the spatial dependency of the custom nonlinear gradient coil and the B_0 and B_1 maps at the slice location are required as input for the optimization solver. Corresponding distributions are provided in Fig. 6.8.

Optimizations results are presented in Fig. 6.9. The normalized B_1^+ map has a standard deviation of 0.148. If the expected normalized flip angle distributions in the first row of Fig. 6.9 are considered, the standard deviations decrease to 0.119, 0.142 and 0.095 for only L-SEMs, only N-SEMs and simultaneous use, respectively. In the second row of Fig. 6.9, normalized measured flip angle maps are provided. The standard deviations for the measured flip angle maps are 0.143, 0.158 and 0.121 for only linear, only nonlinear and simultaneous use. In Figure 9i, simultaneous use of L-SEMs and N-SEM yields a much narrower distribution centered on 1, which is an indication of more uniform excitation.

In the experiment, although the profiles of the expected and measured normalized flip angle maps are similar, due to a practical reason that will be explained later, expected and measured normalized flip angle maps have slightly different standard deviations. The root mean square error (RMSE) between the expected and measured flip angle maps is 0.09 for all three cases. The standard deviations are decreased by 20%, 4% and 46% for only the N-SEM, only L-SEMs and simultaneous use, respectively. The profiles of the corrected map using only the N-SEM are very similar to the B_1^+ profile, and the very small decrease in the standard deviation suggests that the N-SEM alone is inadequate to correct inhomogeneity. The use of L-SEMs alone performed better than the N-SEM alone; however, it provides almost half of the correction provided by simultaneous use. Both in Fig. 6.9c and Fig. 6.9f, the final excitation profiles have almost ideal uniformity except the regions close to edges. One possible reason might be that the algorithm suffers from relatively higher B_0 inhomogeneity at the edges.

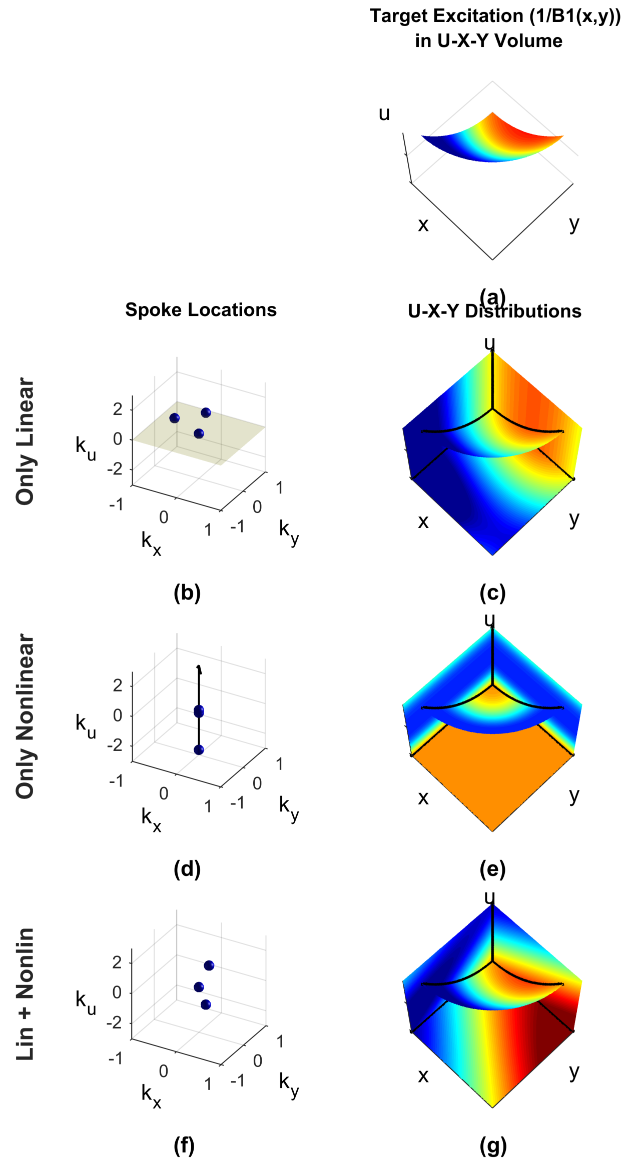

Figure 6.7: Results for 2D simulations. $U - X - Y$ Volume distributions show the realized corrections and Fourier transform of the spokes. Distributions on $\delta(u - x^2 - y^2)$ are shown. **(a)** Inverse of the $B_1(x, y)$ distribution in Fig. 6.6a is mapped onto $\delta(u - x^2 - y^2)$. **(b)** Optimized spoke locations are on the $k_u = 0$ plane by using only L-SEMs. **(c)** In the $U - X - Y$ Volume, no variation in the u-direction is observed. **(d)** Optimized spoke locations are on the $(k_x, k_y) = (0,0)$ line by using only the N-SEM. **(e)** In the $U - X - Y$ Volume, no variation in the x- or y-direction is observed. **(f)** Optimized spoke locations are in 3D space by using both L-SEMs and the N-SEM. **(g)** In the $U - X - Y$ Volume, there are variations in all directions.

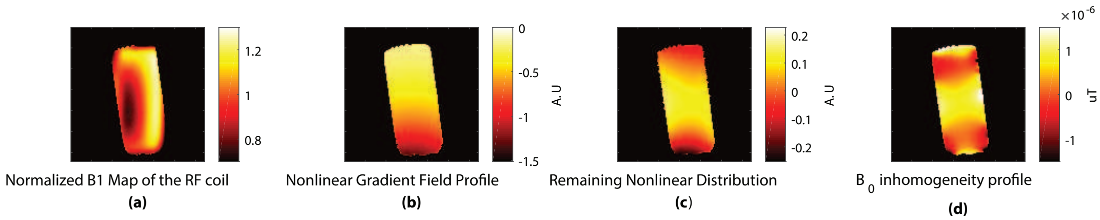

Figure 6.8: Input distributions for optimization. **(a)** Normalized B_1^+ map of the single-channel transmit coil such that the average of the B_1^+ over ROI is 1. **(b)** Spatial dependency of the nonlinear gradient coil over ROI given in arbitrary units (A.U.). **(c)** Spatially nonlinear distribution of the coil after subtraction of spatially constant term and LSEM terms from the actual profile of the NSEM coil. **(d)** Deviation of the static magnetic field from the magnetic field corresponding to the adjusted frequency.

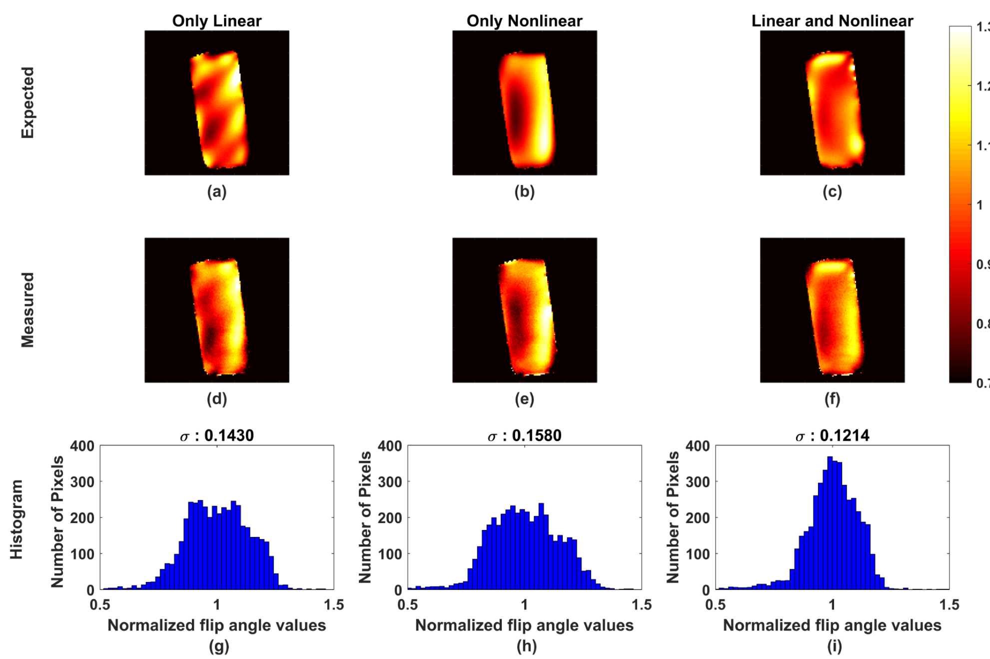

Figure 6.9: Normalized flip angle maps after correction using only L-SEMs, only the N-SEM and the combination of L-SEMs and the N-SEM. **(a-c)**: Normalized expected flip angle distributions after the optimizations for only L-SEMs, only the N-SEM and simultaneous use of both. **(d-f)**: Normalized flip angle distributions measured with the Double Angle method for each case. **(g-i)**: Histogram of the pixels in the normalized measured flip angle distribution over the ROI. The standard deviation from the average is provided for each case.

6.5 Discussion and Conclusion

6.5.1 Freedom of the Simultaneous Use of L-SEMs and N-SEMs

Although the simultaneous use of L-SEMs and N-SEMs is harder to interpret and requires more complicated design strategies, driving them with independent time waveforms is the most flexible design for a given target transverse magnetization. For a design framework and better intuition, the excitation k-space is formulated in Eq. 6.5 with an increase from three dimensions to four through the inclusion of the N-SEM. According to this formulation, infinitely many different excitation k-spaces can lead to the same excitation profile in space. This is demonstrated in Fig. 6.2 with Fig. 6.4 different examples, resulting in a rectangular 1D excitation profile originating from completely different excitation k-spaces that differ in total energy, dimensionality and length of the required trajectory. A dual approach would be for the $u - x$ plane to be freely filled (except for the points lying on $\delta(u(r) - u)$) while altering the excitation k-space. However, in Figs. 6.2f, 6.2g, 6.5b, and 6.5c, the use of only L-SEMs or only the N-SEM leads to only 1D variation in the $u - x$ plane, which results in suboptimal solutions. As a result of this flexibility, simultaneous use leads to more homogenous excitation profiles than the use of only L-SEMs or only N-SEMs, as in Figures 6.5, 6.6, 6.6 and Table 6.1. Especially for the same RF power limit, simultaneous use still performs better than using only L-SEMs. Without this result, one might suspect that homogeneity improvement might be obtained at the expense of increased SAR when L-SEMs and N-SEMs are simultaneously used. However, it is shown that the better performance of simultaneous use is not due to an increase in the SAR but to an increase in the degrees of freedom. Because the simultaneous use of L-SEMs and the N-SEM is the generalized case of using only L-SEMs or N-SEMs, improvement in the performance is enabled at the expense of hardware and design complexity.

Although the experimentally measured and simulated flip angle profiles are in agreement, the measured standard deviations of the flip angles are slightly higher than the simulated ones in Fig. 6.9. However, the RMSEs between the measured and simulated flip angle maps are 9% for all cases, which still allows fair comparison between the cases. There are two main reasons for this in addition to experimental imperfections. First, the double angle method assumes a linear relationship between the transmit field and flip angle. This linear relation starts to break down after the small tip angle regime, which is 30° for spatially selective excitation pulses [88]. However, small tip angle pulses still work reasonably well up to 90° pulses [88], and deviations from the linear relation in the double angle method can be neglected up to 140° [96]. Therefore, the error of the double angle method in spoke excitation is neglected. Another possible reason for the higher standard deviation in the experiments is that noise is present during the experiments, and nonlinear computation of the double angle method amplifies the noise [97]. However, simultaneous use also provides better homogeneity in the measured flip angle maps.

Contrary to orthogonal L-SEMs, N-SEMs can be written as a summation of a spatially constant term, L-SEMs and a remaining spatially nonlinear term, which is very similar to terminology in [89]. In the spoke excitation with simultaneous use of L-SEMs and N-SEM, a spatially constant term causes a spatially constant phase term for the magnetization that can be provided with the phase of the RF pulse. L-SEM terms in the N-SEM profile can already be provided by the actual L-SEM coils. The remaining spatially nonlinear term is the actual cause of the increase in the degrees of freedom. For our example N-SEM coil, the remaining spatially nonlinear term is shown in Fig. 6.8c.

In this work, different example B_1^+ distributions for each case are used. In the case of a general B_1^+, all possible B_1^+ inhomogeneities can be corrected with only L-SEMs theoretically if there is no strict limit on the spoke number. In such a scenario, the freedom resulting from the addition of an N-SEM channel might be used to decrease the RF power or pulse duration. If there is a limit on the spoke number, the remaining spatially nonlinear distribution of the N-SEM channel has a significant impact on the final flip angle homogeneity performance. The increase in the performance is more explicit when the spatial harmonics of the inverse B_1^+

profile can be expressed as a superposition of different combinations of L-SEM and N-SEM profiles. For example, flip angle inhomogeneity is decreased to 96% of the uncorrected case in Fig. 6.5 because the inverse of the B_1 profile has mostly second and first order variations that can be corrected with the simultaneous use of L-SEM (x) and N-SEM (x^2). However, the increase in the performance can vary for different B_1^+ inhomogeneity profiles. For instance, the increase in the performance by adding an additional N-SEM channel is higher for 2D simulations compared to the experiments because the simulated B_1^+ profile can be better expressed with the available channels in Fig. 6.6. In experiments, the B_1^+ inhomogeneity profile has more variation along the x-direction compared to the z-direction in Fig. 6.8a, and the remaining spatially nonlinear term has more variation along z and less variation along the x-direction as in Fig. 6.8c. However, simultaneous use of L-SEMs and N-SEM could increase the performance in all cases.

Furthermore, static field heterogeneity is not formulated in the excitation k-space formulation because it is always present during the RF pulse and cannot be controlled. There are two main drawbacks to B_0 inhomogeneity in spoke excitation. First, if spokes are in the reverse direction, the effects of B0 inhomogeneity for even and odd spokes are different, which can disturb the expected spoke excitation profile. Therefore, the flyback trajectory is used to avoid this effect as in Fig. 6.4. In the flyback trajectory, even if the slice profiles are disturbed, they are in-phase for all spokes; therefore, the expected spoke excitation can be obtained. To decrease this effect, N-SEM coils can be used as shim coils during the RF pulses if the N-SEM profile can correct some portion of the B_0 inhomogeneity. The second effect is the probably unwanted phase accumulation due to B_0 inhomogeneity between the RF pulses, and it is already included in the optimization in Eq. 6.6 for correction as much as possible by the N-SEM profile.

6.5.2 Related Works

In a conference abstract [98], Grissom showed that for a specific transmit array B_1^+ profile, the simultaneous use of L-SEMs and N-SEMs in combination with parallel transmission can result in better uniformity, which can be exchanged for a lower number of spokes or a lower number of transmit channels. As an extension to Grissom's work, our study provides a theoretical perspective for understanding the increase in the degrees of freedom when additional N-SEMs are included, which is the first experimental validation of the concept with spoke numbers higher than two and considerations of RF power limitations and static field heterogeneity.

Kopanoglu et al. has also introduced the excitation k-space variables for N-SEMs [91]. These authors used a coordinate transformation from linear spatial variables to nonlinear spatial variables by assuming that encoding fields are bijective, which is generally not the case for higher order spherical harmonics. In their work, the coordinate transformation does not consider the simultaneous use of L-SEMs together with N-SEMs. Furthermore, in [98], the general phase term during the excitation is expressed as a summation of the static nonlinear terms, the dynamic nonlinear terms and the terms that can be interpreted as commonly known excitation k-space variables for L-SEMs. Similarly, Haas has used parallel transmission together with only N-SEMs and expressed the total phase term as a summation of independent gradient channels that can have independent time evolutions or space dependencies [90]. Both studies [90, 98] have used the direct phase evolution approach in the RF pulse design.

Other works aiming to conduct B_1^+ correction via N-SEMs have used 2-spoke excitation with a specific combination of N-SEMs and L-SEMs [99, 100]. In [99, 100], the best spatial phase profile that can be generated between the two spokes is analytically derived by assuming the same amplitude and phase for each spoke. The analytical expression is advantageous in terms of computation time, but the fixed number of spokes with the same amplitude and phase can limit the performance of the B_1^+ correction. Later, the required phase profiles are estimated by using L-SEMs and N-SEMs with either second-order static shim coils [99] or 48-channel dynamic MC hardware [100]. Another study [35] has proposed creating the spatial profile as a superposition of the first- and second-order gradients, which should be similar to the inverse profile of B_1^+, to correct B_1^+ inhomogeneity in simulations. In such a scenario, the single excitation k-space variable for the superposition of the first- and second-order gradients is defined. Furthermore, it is assumed that the desired target magnetization profile can be parameterized by the gradient encoding fields, which leads to a Fourier transformation relation in a lower dimension between single excitation k-space and transverse magnetization. As an extension of this work, our excitation k-space formulation defines independent variables for each N-SEM channel, and a Fourier transform relationship is still re-established in the increased dimension without requiring the parameterization of the target distribution. Later, this work has been extended to parallel transmission with a similar design principle for a spatial phase profile [36]. Although the number of spokes is greater than 2, the approach is also suboptimal since it uses the same combination of N-SEMs and L-SEMs for all spokes; in other words, the phase profiles created between the spokes are only linearly scaled versions of each other. Previous methods [35, 36, 99, 100] might be extremely effective for correcting even highly variant B_1^+ inhomogeneities in space if there are a high number of independent N-SEM channels to implement the required phase profile at the expense of hardware complexity. However, the approaches are still suboptimal because the required phase profile might not be created by the available hardware; therefore, an optimization that considers the available field profiles at the first stage can still be useful.

6.5.3 Pulse Design

In this paper, the term B_1^+ inhomogeneity correction is referred since it is referred in the original paper and a common name in the literature [35]. Actually, B_1^+ profile cannot be altered using the pulse design or gradients. It is originated from the wavelength effect of the RF coil. In this study, flip angle inhomogeneity originated from B_1^+ inhomogeneity is corrected simultaneously using L-SEMs and N-SEM in the pulse design.

Although the addition of a single channel N-SEM coil improves the flip angle uniformity, the pulse design problem becomes computationally more expensive due to spoke placement in higher dimension and an increased number of local minima resulting from the possibility of infinitely many trajectories for the same excitation pattern. The best solution for L-SEMs and N-SEMs would have been obtained if fewer trial points were specified as a stopping criterion. However, the value of the objective function for simultaneous use is still less than that for the use of only L-SEMs or N-SEMs for the first 200 trial points. Therefore, increases in the number of local minima and the number of variables lead to a more complex optimization procedure for simultaneous use of L-SEMs and the N-SEM; however, simultaneous use might still have superior performance in terms of local solutions in comparison with using only L-SEMs or the N-SEM.

Global optimization can also be used to minimize the cost function under the linear or nonlinear inequality constraints such as maximum distance in the excitation k-space, maximum RF average power or peak power. Furthermore, computation is parallelized, and the computation time can be limited as applied in the optimizations in the experiments. However, finding the global optimum for a much higher number of N-SEM channels is still a challenging problem, although the scatter search algorithm can find global solutions to the problem of over 100 variables and 100 constraints in one or two local solver calls for most of the nonlinear programming applications [92]. In a practical case with a time limitation, some algorithms for finding the local solutions instead of the global solution can result in a better performance. However, the built-in "GlobalSearch" function in MATLAB is used to demonstrate that the global solution of the simultaneous use of L-SEMs and the N-SEMs can provide more homogeneous excitations than the use of only L-SEMs or N-SEMs.

The pulse design techniques in the literature, which use only L-SEMs, can be utilized to accelerate the computation time or to obtain a better solution in a limited time, although they are not studied for N-SEMs. For instance, it can be shown that the analytical minimum to obtain the most homogenous flip angle distribution for given spoke locations in local gradient-based algorithms [101] is still applicable when L-SEMs and N-SEMs are simultaneously used. A sparsity enforced method can also be adapted to the simultaneous use of L-SEMs and N-SEMs to decrease the spoke numbers [33]. However, the gradient based methods and the sparsity enforced methods do not consider the B_0 effect at the beginning and require retuning after the spoke placement. They can be used for a given target excitation phase distribution, which makes them suboptimal for optimizing only the amplitude distribution. Grissom et. al. [102] proposes an interleaved greedy and local optimization method including target phase optimization. Although his pulse design technique is closer to the global optimum than the abovementioned two methods for the amplitude excitation profile optimization at the expense of computation time, sequential placement of spokes avoids the global optimality. In the "GlobalSearch" optimization, the target excitation phase is not fixed, and the spokes are not placed sequentially for global optimality with a fixed number of spokes. Lastly, the pulse design process can be extremely accelerated and better homogeneity performance can be managed with fewer spokes if there are numerous channels for obtaining the optimal phase distribution between two spokes at the expense of hardware complexity [99, 100].

Another important consideration for the RF pulse design is the three-dimensional spatial dependency of the N-SEM channel. Due to the zero Laplacian property of static magnetic fields, nonlinear deviation in one direction is likely to cause nonlinear deviation in another direction. Therefore, the field profile of N-SEM channels has through-plane deviations. Under thin slice approximation, this dependency can be approximated as two-dimensional, and Eq. 6.6 can be valid. If the thin slice approximation fails, two related drawbacks might occur. First, the transverse excitation profile can be changed because through-slice phase accumulation is not uniform in the transverse plane. Second, if there is still through-slice phase dependency after the excitation, signal dephasing inside the pixel will decrease the image intensity. Even if the B_1^+ inhomogeneity is two-dimensional, three-dimensional considerations should be included to correct B_1^+ inhomogeneity in thicker slices or slabs with N-SEMs. In the prototype coil, simulations suggest that the field profile can deviate from 1% to 2% in the slice direction for each pixel. For the field measurement, one reference GRE image and another GRE image with a blip current applied to the N-SEM channel are obtained. Due to signal dephasing not only in the slice direction but also in all three-dimensional pixel volumes, the average amplitude was 3% lower in the GRE image with blip current. During field measurements, the maximum phase deviation was lower than π, and during the spoke excitation, the most distant spoke location was -0.65, as in Table 6.1, which suggest that 2% in-slice phase deviation of the total 0.65π phase is present during the excitation in a worst-case scenario. Such a phase distribution is negligible in our case, which is consistent with the match between measured and expected flip angle maps in Fig 6.9; however, the in-slice dependency of N-SEM channels must be carefully considered in other applications.

6.5.4 Practical Considerations

Although coil and amplifier design is beyond the scope of this chapter, a prototype N-SEM coil is manufactured as proof of concept with a diameter of 20 cm to fit inside the scanner, and it is torque balanced due to angular symmetry. However, the pulse design techniques and theoretical formulations would have been valid if a human-size N-SEM coil had been available. The switching times of N-SEM coils must be further investigated when they are simultaneously used with L-SEMs in a human experiment. From the hardware perspective, switching times are mostly determined by the voltage of the amplifier; however, physiological factors, such as PNS, generally determine the limits. Depending on the vector E-field distributions of the N-SEMs and L-SEMs, new PNS limitations should be determined considering the superposition of the fields during simultaneous use. In spoke excitation, the optimal phase distribution is generally smooth between the RF pulses to correct slowly varying transmit heterogeneity. The dead space between the RF pulses due to the rise and fall times of the slice select gradient is generally enough to switch the required small current values of N-SEM coils. Even if the dead space is insufficient, the excitation k-space is designed in this work, and realizing a specific excitation k-space with RF and gradient waveforms can be solved by including slew rate considerations. However, the VERSE excitation [82] or receive purposes are generally more demanding in terms of slew rate, and the simultaneous use of N-SEMs and L-SEMs requires further investigations.

Because the custom coil system does not have a shield, the eddy current and the coupling issues are also considered. Coupling from our coil to system gradients is neglected since the shield of the system gradients almost cancels the net effect. More importantly, the coupling from system gradients to the custom coil is stronger. When the custom coil is placed at the isocenter of the scanner, the x and y gradients do not cause any coupling problems since the net flux passing through the custom coil is 0; however, such symmetry does not exist for the z gradient. Thus, the slew rate is minimized for all system gradient waveforms. The eddy current effects are considered in two classes: short- and long-time constant eddy currents. For the short-time constant eddy currents, most of the effect exists in the same duration as the current applied to the custom coil. In the measurement of the field profile on the slice of interest and spoke sequences, a triangular current waveform that is exactly the same except for the amplitude is used. Therefore, fast decaying eddy current effects are considered in the field profile and should be the same for the spoke sequence assuming that the eddy current effects are linear. As mentioned in previous works [103], for long-lasting eddy current effects, if the duration of the current waveform is very small compared to the time constant, the eddy currents caused by rising and falling edges tend to cancel each other out. Therefore, a very fast triangular current waveform is used to drive the custom coil. As a result, eddy current and coupling effects for the custom coil are mostly counteracted.

6.5.5 Possible Enhancements

In this chapter, defining an independent excitation k-space for N-SEMs is shown to provide freedom and improvements in correcting the B_1^+ inhomogeneity. Very similar techniques can be used for FOV reduction and slice selection. Additionally, the excitation k-space can be designed in such a way that shorter trajectories or lower SAR RF pulses can lead to the same excitation profiles. Furthermore, although spoke excitation is used in this study, in principle, time-varying gradient waveforms can be played during the RF pulse to traverse curved k-space trajectories and allow more freedom to optimize the solution.

The independent excitation k-space formulation trivially allows for increasing the number of N-SEMs. Although computationally more expensive, it might provide a dramatic improvement in the performance. Instead of using multiple N-SEMs, it is shown that the addition of each N-SEM increases the dimension of the degrees of freedom in the RF excitation problem. Existing gradient coil arrays in [7, 99, 100, 104] and dynamic second-order coils can be utilized under the proposed technique. Furthermore, alternative linear gradient coil designs [79, 105, 106] can be used to generate nonlinear gradients, although they have been designed for flexible linear gradient systems. Further, parallel excitation techniques [30, 31] can be combined with the proposed method if the formulation is generalized. Lastly, although this study only considers the small tip angle excitation regime, the formulation might be extended in a similar manner to large tip angle pulses since the excitation k-space concept is still present for Cayley-Klein parameters in the small excitation solution of large tip angle pulses [107].

Chapter 7

Discussion and Conclusion

In the first part of Chapter 2, nine channel z-gradient coil array is physically described. Simulations and field profiles measurements confirms that coil is manufactured with a reasonably well accuracy. Continuous winding of array elements enables to generate highly flexible field profiles that are angularly symmetric. In other words, any continuous current density required for a target field [84] as a function z coordinate can be sampled with a z-gradient array by applying independent currents to each channel. The main limitation of the manufactured z-gradient coil array is that diameter of the coil is not suitable for human applications. The design of a human-size gradient coil array should consider many practical issues such as inductance, DC and AC resistance, force, torque, available physical space in the scanner, heat exchange, mechanical design, patient comfort and shielding. Furthermore, coil should be able to create enough field variation and slew rate considering the current and voltage limitations of the amplifier, respectively, and the power requirements of the gradient amplifiers are proportional to the fifth power of the coil dimensions [108]. Moreover, coil is designed as unshielded. In future applications, a shield can be designed for each element separately or an array of shield coils can be driven to minimize the magnetic flux outside of the shield.

In the second part of Chapter 2, some amplifier and driver challenges together with their solutions are proposed. The mutual coupling between the channels is a main challenge to drive the gradient coil arrays. Although mutual coupling can be avoided in the design process, any effort to decrease the mutual coupling also decreases the degree of freedom in the coil design. Additionally, it is impractical to completely avoid mutual coupling for high number of channels. A simple first order circuit model is proposed and validated with impedance meter measurements, current measurements and MRI experiments. First order model enables an analytical expression to calculate the minimum rise time for a given current vector, mutual impedance parameters and amplifier limitations. As a result, it is verified in Chapter 2 that z-gradient array system is operational and can provide high time fidelity current to be used in imaging.

In chapter 3, linear gradient fields with different specifications and performance parameters are optimized using the z-gradient array. This chapter is studied to prove that gradient array coil can generate dynamically arrangeable linear gradient profiles in contrast to conventional linear gradient coils. Therefore, linear gradient fields optimized for only target VOIs with maximum tolerable linearity error can be used to increase the performance of the gradient fields without any change in the pulse design and image reconstruction techniques which are all developed for linear gradient fields.

Expectedly, It is shown that peak linearity error of the gradient fields can be reduced significantly by optimizing the field profiles only in the target VOIs. Moreover, optimization problems are formulated for maximum gradient strength, maximum slew rate, minimum current norm and minimum peak B-field. One advantage of this optimization problems is that they are all convex problem and can be solved using fast local solvers. In all of the optimization problems linearity error is constrained. The results of the sweep for L_{VOI} and α shows that all optimization problems have similar characteristics in terms of L_{VOI} and α. In all cases, increased α or decreased L_{VOI} results in increased performance parameters. Therefore, decisions on these parameters can significantly affect the performance. One can also construct a look-up table similar to Fig. 3.3 to determine the minimum linearity error for a given performance metrics. As part of this thesis, only the slew rate limits in terms of hardware are investigated. There is no single slew rate limitation in terms of PNS since the E-field distributions of the coil elements are superposed with dynamically changing current weightings. However, this effect should be analyzed in future studies of gradient coil arrays for human applications. Although results for shifted VOIs are not presented in this chapter, results might be extended for VOIs with shifted central locations.

In Chapter 4, the concepts in Chapter 3 is applied to DWI to reduce the diffusion gradient duration and echo time to increase the SNR. Performance increase of the gradient strength per unit current due to increased linearity error or decreased VOI size is utilized to obtain higher gradient strength if the gradients are dynamically optimized for each slice instead of optimization over the entire volume. Surely, method is not limited for slices only, any VOI can be determined and gradient strengths can be maximized only inside the VOI. Moreover, allowing some nonlinearity also helps to increase the gradient strength which results in non-uniform b-value maps. In such a case, b-value should be calculated at each pixel together with a direction which should be used in the post-processing while calculating the ADC maps. Similar to decreased diffusion gradients, dynamically optimized gradient fields can also be used in the readout part to further decrease the TE, especially for in-slice diffusion directions.

In addition to dynamic optimization of linear gradient fields, novel applications of nonlinear gradients are studied since gradient array system can generate various different nonlinear gradient field profiles. The nonlinear gradients are already shown to provide additional degrees of freedom to improve the efficiency of both the reception and excitation phases of an imaging sequence. In the reception h n phase of a pulse sequence, the N-SEMs are utilized in accelerating the scan [2–5], reducing the FOV [6], reducing the peripheral nerve stimulation and increasing the resolution at the periphery of the object [7–9]. For the excitation part of a pulse sequence, it has been shown that the N-SEMs can be used to excite curved slices [4, 10, 11], reduce the FOV with localized excitation [12–14, 94], reduce the SAR [91] in addition to the B1+ inhomogeneity correction . Additionally, the dynamic shimming methods using time-varying higher-order spatial field terms [54, 56, 104] can be considered as an application for the N-SEMs. Therefore, gradient array system is not only useful for the applications in this thesis, it can also be used in other applications of nonlinear gradients and might even advance those methods.

In Chapter 5, gradient array is used to encode multiple slice locations to the same frequency. This enables excitation of multiple slices or slabs with a single band RF pulse without increasing the SAR. Simultaneous multi-slice (SMS) imaging is a technique to speed up the MRI data acquisition. However, increase in the SAR of the RF pulse might limit the decrease in the MRI data acquisition. Moreover, duration of the RF pulse can be shortened for increased robustness to B_0 inhomogeneity or decreased TE since SAR and peak RF power is decreased using the proposed technique. In most challenging sequences in terms of SAR such as Turbo Spin Echo, this technique might even be more useful to combine them with SMS. There are two limitations of this study. Firstly, center location of the slices and slice thickness as function of radial direction might vary inside the slice. Secondly, slice separations cannot be decreased below 5 cm without compromising dramatic performance decrease. However, it is shown that both limitations do not prevent to cover entire 3D volume by shifting slice locations appropriately.

In Chapter 6, single nonlinear gradient is used simultaneously with linear gradients to compensate the B_1^+ inhomogeneity. Although nonlinear gradient field is not generated by gradient array, gradient array is fully capable of generating such gradient and might even optimize the required nonlinear gradient profile. Simultaneous use of linear and nonlinear gradients during the RF excitation is formulated as excitation k-space with increased dimension. Although this formulation does not directly solve inverse problem of designing gradient waveforms at all cases, it clearly emphasizes the increased degree of freedom when nonlinear gradients are simultaneously used with linear gradients. As a results, it is shown with both simulations and experiments that simultaneous use of linear and nonlinear gradients can provide more uniform excitation patterns compared to using only nonlinear gradients or linear gradients alone.

In this PhD thesis, design and applications of a gradient array are studied.

Due to the fact that spatial distribution of gradient fields encodes the spin locations, gradient systems are significant part of the magnetic resonance scanners. As discusses in the thesis, transforming conventional gradient coils into an array system requires some hardware challenges in return of tremendous increase in the gradient field design flexibility. Some hardware challenges and solutions of a gradient array system is addressed as part of this thesis. Capability of dynamically designing gradient fields enables optimization of encoding the spin locations. The advantage of increased degree of freedom in the gradient field design is utilized in two ways. Firstly, it is shown that some performance parameters and target VOI can be modulated for linear gradient fields. As an example application of this, diffusion encoding gradient duration for a fixed b-value is decreased to increase SNR by maximizing the gradient strength only inside the target VOI and allowing more linearity error. Secondly, gradient array can generate nonlinear gradients. Example and novel applications of nonlinear gradients are presented such as multi-slice excitation with a single band RF pulse and simultaneous use of linear and nonlinear gradients for improved B_1^+ inhomogeneity correction. In summary, feasibility and advantage of the gradient array system is demonstrated with both simulations and experiments to further motivate the studies in this field and expedite the clinical use of this technology.

Bibliography

[1] R. Turner, "Gradient coil design: a review of methods," *Magnetic resonance imaging*, vol. 11, no. 7, pp. 903–920, 1993.

[2] J. P. Stockmann, P. A. Ciris, G. Galiana, L. Tam, and R. T. Constable, "O-space imaging: highly efficient parallel imaging using second-order nonlinear fields as encoding gradients with no phase encoding," *Magnetic resonance in medicine*, vol. 64, no. 2, pp. 447–456, 2010.

[3] L. K. Tam, J. P. Stockmann, G. Galiana, and R. T. Constable, "Null space imaging: nonlinear magnetic encoding fields designed complementary to receiver coil sensitivities for improved acceleration in parallel imaging," *Magnetic resonance in medicine*, vol. 68, no. 4, pp. 1166–1175, 2012.

[4] H. Weber, G. Schultz, D. Gallichan, J. Hennig, and M. Zaitsev, "Local field of view imaging for alias-free undersampling with nonlinear spatial encoding magnetic fields," *Magnetic resonance in medicine*, vol. 71, no. 3, pp. 1002–1014, 2014.

[5] K. J. Layton, D. Gallichan, F. Testud, C. A. Cocosco, A. M. Welz, C. Barmet, K. P. Pruessmann, J. Hennig, and M. Zaitsev, "Single shot trajectory design for region-specific imaging using linear and nonlinear magnetic encoding fields," *Magnetic resonance in medicine*, vol. 70, no. 3, pp. 684–696, 2013.

[6] D. G. Wiesler, H. Wen, S. D. Wolff, and R. S. Balaban, "Reduction of field of view in mri using a surface-spoiling local gradient insert," *Journal of Magnetic Resonance Imaging*, vol. 8, no. 4, pp. 981–988, 1998.

[7] J. Hennig, A. M. Welz, G. Schultz, J. Korvink, Z. Liu, O. Speck, and M. Zaitsev, "Parallel imaging in non-bijective, curvilinear magnetic field gradients: a concept study," *Magnetic Resonance Materials in Physics, Biology and Medicine*, vol. 21, no. 1-2, p. 5, 2008.

[8] D. Gallichan, C. A. Cocosco, A. Dewdney, G. Schultz, A. Welz, J. Hennig, and M. Zaitsev, "Simultaneously driven linear and nonlinear spatial encoding fields in mri," *Magnetic resonance in medicine*, vol. 65, no. 3, pp. 702–714, 2011.

[9] G. Schultz, P. Ullmann, H. Lehr, A. M. Welz, J. Hennig, and M. Zaitsev, "Reconstruction of mri data encoded with arbitrarily shaped, curvilinear, nonbijective magnetic fields," *Magnetic resonance in medicine*, vol. 64, no. 5, pp. 1390–1403, 2010.

[10] P. Börnert and T. Schäffter, "Curved slice imaging," *Magnetic resonance in medicine*, vol. 36, no. 6, pp. 932–939, 1996.

[11] H. Weber, D. Gallichan, G. Schultz, C. A. Cocosco, S. Littin, W. Reichardt, A. Welz, W. Witschey, J. Hennig, and M. Zaitsev, "Excitation and geometrically matched local encoding of curved slices," *Magnetic resonance in medicine*, vol. 69, no. 5, pp. 1317–1325, 2013.

[12] C. Ma, D. Xu, K. F. King, and Z.-P. Liang, "Reduced field-of-view excitation using second-order gradients and spatial-spectral radiofrequency pulses," *Magnetic resonance in medicine*, vol. 69, no. 2, pp. 503–508, 2013.

[13] W. R. Witschey, C. A. Cocosco, D. Gallichan, G. Schultz, H. Weber, A. Welz, J. Hennig, and M. Zaitsev, "Localization by nonlinear phase preparation and k-space trajectory design," *Magnetic resonance in medicine*, vol. 67, no. 6, pp. 1620–1632, 2012.

[14] H. Islam and G. H. Glover, "Reduced field of view imaging using a static second-order gradient for functional mri applications," *Magnetic resonance in medicine*, vol. 75, no. 2, pp. 817–822, 2016.

[15] S. Taraghinia, "A z-gradient coil array system for magnetic resonance imaging," Master's thesis, Bilkent University, 2016.

[16] K. Setsompop, R. Kimmlingen, E. Eberlein, T. Witzel, J. Cohen-Adad, J. A. McNab, B. Keil, M. D. Tisdall, P. Hoecht, P. Dietz, *et al.*, "Pushing the limits of in vivo diffusion mri for the human connectome project," *Neuroimage*, vol. 80, pp. 220–233, 2013.

[17] M. Barth, F. Breuer, P. J. Koopmans, D. G. Norris, and B. A. Poser, "Simultaneous multislice (sms) imaging techniques," *Magnetic resonance in medicine*, vol. 75, no. 1, pp. 63–81, 2016.

[18] A. Sbrizzi, B. A. Poser, D. H. Tse, H. Hoogduin, P. R. Luijten, and C. A. van den Berg, "Rf peak power reduction in caipirinha excitation by interslice phase optimization," *NMR in Biomedicine*, vol. 28, no. 11, pp. 1393–1401, 2015.

[19] E. J. Auerbach, J. Xu, E. Yacoub, S. Moeller, and K. Uğurbil, "Multiband accelerated spin-echo echo planar imaging with reduced peak rf power using time-shifted rf pulses," *Magnetic resonance in medicine*, vol. 69, no. 5, pp. 1261–1267, 2013.

[20] D. G. Norris, P. J. Koopmans, R. Boyacioğlu, and M. Barth, "Power independent of number of slices (pins) radiofrequency pulses for low-power simultaneous multislice excitation," *Magnetic resonance in medicine*, vol. 66, no. 5, pp. 1234–1240, 2011.

[21] C. Eichner, L. L. Wald, and K. Setsompop, "A low power radiofrequency pulse for simultaneous multislice excitation and refocusing," *Magnetic resonance in medicine*, vol. 72, no. 4, pp. 949–958, 2014.

[22] A. Sharma, M. Lustig, and W. A. Grissom, "Root-flipped multiband refocusing pulses," *Magnetic resonance in medicine*, vol. 75, no. 1, pp. 227–237, 2016.

[23] C. S. Aigner, C. Clason, A. Rund, and R. Stollberger, "Efficient high-resolution rf pulse design applied to simultaneous multi-slice excitation," *Journal of magnetic resonance*, vol. 263, pp. 33–44, 2016.

[24] B. A. Poser, R. J. Anderson, B. Guérin, K. Setsompop, W. Deng, A. Mareyam, P. Serano, L. L. Wald, and V. A. Stenger, "Simultaneous multislice excitation by parallel transmission," *Magnetic resonance in medicine*, vol. 71, no. 4, pp. 1416–1427, 2014.

[25] X. Wu, S. Schmitter, E. J. Auerbach, S. Moeller, K. Uğurbil, and P.-F. Van de Moortele, "Simultaneous multislice multiband parallel radiofrequency excitation with independent slice-specific transmit b1 homogenization," *Magnetic resonance in medicine*, vol. 70, no. 3, pp. 630–638, 2013.

[26] B. Guérin, K. Setsompop, H. Ye, B. A. Poser, A. V. Stenger, and L. L. Wald, "Design of parallel transmission pulses for simultaneous multislice with explicit control for peak power and local specific absorption rate," *Magnetic resonance in medicine*, vol. 73, no. 5, pp. 1946–1953, 2015.

[27] J. T. Vaughan, M. Garwood, C. Collins, W. Liu, L. DelaBarre, G. Adriany, P. Andersen, H. Merkle, R. Goebel, M. Smith, *et al.*, "7t vs. 4t: Rf power, homogeneity, and signal-to-noise comparison in head images," *Magnetic resonance in medicine*, vol. 46, no. 1, pp. 24–30, 2001.

[28] P.-F. Van de Moortele, C. Akgun, G. Adriany, S. Moeller, J. Ritter, C. M. Collins, M. B. Smith, J. T. Vaughan, and K. Uğurbil, "B1 destructive interferences and spatial phase patterns at 7 t with a head transceiver array coil," *Magnetic resonance in medicine*, vol. 54, no. 6, pp. 1503–1518, 2005.

[29] W. Mao, M. B. Smith, and C. M. Collins, "Exploring the limits of rf shimming for high-field mri of the human head," *Magnetic Resonance in Medicine*, vol. 56, no. 4, pp. 918–922, 2006.

[30] U. Katscher, P. Börnert, C. Leussler, and J. S. Van Den Brink, "Transmit sense," *Magnetic Resonance in Medicine*, vol. 49, no. 1, pp. 144–150, 2003.

[31] C. M. Collins, W. Liu, B. J. Swift, and M. B. Smith, "Combination of optimized transmit arrays and some receive array reconstruction methods can yield homogeneous images at very high frequencies," *Magnetic resonance in medicine*, vol. 54, no. 6, pp. 1327–1332, 2005.

[32] S. Saekho, C.-y. Yip, D. C. Noll, F. E. Boada, and V. A. Stenger, “Fast-kz three-dimensional tailored radiofrequency pulse for reduced b1 inhomogeneity,” *Magnetic Resonance in Medicine*, vol. 55, no. 4, pp. 719–724, 2006.

[33] A. C. Zelinski, L. L. Wald, K. Setsompop, V. Alagappan, B. A. Gagoski, V. K. Goyal, and E. Adalsteinsson, “Fast slice-selective radio-frequency excitation pulses for mitigating b inhomogeneity in the human brain at 7 tesla,” *Magnetic resonance in medicine*, vol. 59, no. 6, pp. 1355–1364, 2008.

[34] A. C. Zelinski, L. L. Wald, K. Setsompop, V. K. Goyal, and E. Adalsteinsson, “Sparsity-enforced slice-selective mri rf excitation pulse design,” *IEEE transactions on medical imaging*, vol. 27, no. 9, pp. 1213–1229, 2008.

[35] Y.-C. Hsu, I.-L. Chern, W. Zhao, B. Gagoski, T. Witzel, and F.-H. Lin, “Mitigate b1+ inhomogeneity using spatially selective radiofrequency excitation with generalized spatial encoding magnetic fields,” *Magnetic resonance in medicine*, vol. 71, no. 4, pp. 1458–1469, 2014.

[36] Y.-C. Hsu, R. Lattanzi, Y.-H. Chu, M. A. Cloos, D. K. Sodickson, and F.-H. Lin, “Mitigation of inhomogeneity using spatially selective excitation with jointly designed quadratic spatial encoding magnetic fields and rf shimming,” *Magnetic resonance in medicine*, vol. 78, no. 2, pp. 577–587, 2017.

[37] K. Ertan, S. Taraghinia, A. Sadeghi, and E. Atalar, “A z-gradient array for spatially oscillating magnetic fields in multi-slice excitation,” in *Proceedings of the 33rd Annual Scientific Meeting of ESMRMB, Vienna, Austria*, 2016.

[38] K. Ertan, S. Taraghinia, A. Sadeghi, and E. Atalar, “A z-gradient array for simultaneous multi-slice excitation with a single-band rf pulse,” *Magnetic resonance in medicine*, vol. 80, no. 1, pp. 400–412, 2018.

[39] K. Ertan, S. Taraghinia, and E. Atalar, “Driving mutually coupled coils in gradient array systems in magnetic resonance imaging,” in *Proceedings of the 26th Annual Meeting of ISMRM, Paris, France*, 2018.

[40] C. Juchem, O. M. Nahhass, T. W. Nixon, and R. A. de Graaf, “Multi-slice mri with the dynamic multi-coil technique,” *NMR in Biomedicine*, vol. 28, no. 11, pp. 1526–1534, 2015.

[41] S. Littin, F. Jia, K. J. Layton, S. Kroboth, H. Yu, J. Hennig, and M. Zaitsev, “Development and implementation of an 84-channel matrix gradient coil,” *Magnetic resonance in medicine*, vol. 79, no. 2, pp. 1181–1191, 2018.

[42] S. J. Vannesjo, Y. Duerst, L. Vionnet, B. E. Dietrich, M. Pavan, S. Gross, C. Barmet, and K. P. Pruessmann, “Gradient and shim pre-emphasis by inversion of a linear time-invariant system model,” *Magnetic resonance in medicine*, vol. 78, no. 4, pp. 1607–1622, 2017.

[43] E. Smith, F. Freschi, M. Repetto, and S. Crozier, “The coil array method for creating a dynamic imaging volume,” *Magnetic resonance in medicine*, vol. 78, no. 2, pp. 784–793, 2017.

[44] M. Stich, T. Wech, A. Slawig, R. Ringler, A. Dewdney, A. Greiser, G. Ruyters, T. A. Bley, and H. Köstler, “Gradient waveform pre-emphasis based on the gradient system transfer function,” *Magnetic resonance in medicine*, 2018.

[45] J. Sabate, M. Schutten, R. Steigerwald, Q. Li, and W. F. Wirth, “Ripple cancellation filter for magnetic resonance imaging gradient amplifiers,” in *Applied Power Electronics Conference and Exposition, 2004. APEC’04. Nineteenth Annual IEEE*, vol. 2, pp. 792–796, IEEE, 2004.

[46] H. Yu, S. Littin, F. Jia, S. Kroboth, and M. Zaitsev, “Output filter design for gradient amplifier and shimming amplifier of mri: an overview,” in *Proceedings of the 26th Annual Meeting of ISMRM, Paris, France*, 2018.

[47] J. Sabate, L. J. Garces, P. M. Szczesny, Q. Li, and W. F. Wirth, “High-power high-fidelity switching amplifier driving gradient coils for mri systems,” in *Power Electronics Specialists Conference, 2004. PESC 04. 2004 IEEE 35th Annual*, vol. 1, pp. 261–266, IEEE, 2004.

[48] S. Skogestad and I. Postlethwaite, *Multivariable feedback control: analysis and design*, vol. 2. Wiley New York, 2007.

[49] P. Jehenson, M. Westphal, and N. Schuff, "Analytical method for the compensation of eddy-current effects induced by pulsed magnetic field gradients in nmr systems," *Journal of Magnetic Resonance (1969)*, vol. 90, no. 2, pp. 264–278, 1990.

[50] H. M. Gach, I. J. Lowe, D. P. Madio, A. Caprihan, S. A. Altobelli, D. O. Kuethe, and E. Fukushima, "A programmable pre-emphasis system," *Magnetic resonance in medicine*, vol. 40, no. 3, pp. 427–431, 1998.

[51] R. Lai, J. Sabate, S. Chi, and W. Skeffington, "High performance gradient driver for magnetic resonance imaging system," in *Energy Conversion Congress and Exposition (ECCE), 2011 IEEE*, pp. 3511–3515, IEEE, 2011.

[52] S. Taraghinia, K. Ertan, and E. Atalar, "Minimum current ripple in the gradient array system by applying optimum-phase pulse-width modulation pattern," in *Proceedings of the 25th Annual Meeting of ISMRM, Honolulu, Hawaii, USA*, 2017.

[53] S. Taraghinia, K. Ertan, and E. Atalar, "Efficient ripple current reduction in gradient array system using optimized-phase control signals with one stage lc filter," in *Proceedings of the 34th Annual Meeting of ESMRMB, Barcelona, Spain*, ESMRMB, 2017.

[54] C. Juchem, T. W. Nixon, S. McIntyre, V. O. Boer, D. L. Rothman, and R. A. de Graaf, "Dynamic multi-coil shimming of the human brain at 7 t," *Journal of magnetic resonance*, vol. 212, no. 2, pp. 280–288, 2011.

[55] C. Juchem, T. W. Nixon, S. McIntyre, D. L. Rothman, and R. A. de Graaf, "Magnetic field modeling with a set of individual localized coils," *Journal of Magnetic Resonance*, vol. 204, no. 2, pp. 281–289, 2010.

[56] C. Juchem, S. U. Rudrapatna, T. W. Nixon, and R. A. de Graaf, "Dynamic multi-coil technique (dynamite) shimming for echo-planar imaging of the human brain at 7 tesla," *Neuroimage*, vol. 105, pp. 462–472, 2015.

[57] R. Topfer, P. Starewicz, K.-M. Lo, K. Metzemaekers, D. Jette, H. P. Hetherington, N. Stikov, and J. Cohen-Adad, "A 24-channel shim array for the

human spinal cord: Design, evaluation, and application," *Magnetic resonance in medicine*, vol. 76, no. 5, pp. 1604–1611, 2016.

[58] H. Han, A. W. Song, and T.-K. Truong, "Integrated parallel reception, excitation, and shimming (ipres)," *Magnetic resonance in medicine*, vol. 70, no. 1, pp. 241–247, 2013.

[59] J. P. Stockmann, T. Witzel, B. Keil, J. R. Polimeni, A. Mareyam, C. LaPierre, K. Setsompop, and L. L. Wald, "A 32-channel combined rf and b0 shim array for 3t brain imaging," *Magnetic resonance in medicine*, vol. 75, no. 1, pp. 441–451, 2016.

[60] S. Umesh Rudrapatna, F. Fluerenbrock, T. W. Nixon, R. A. de Graaf, and C. Juchem, "Combined imaging and shimming with the dynamic multi-coil technique," *Magnetic resonance in medicine*, 2018.

[61] B. Zhang, Y.-F. Yen, B. A. Chronik, G. C. McKinnon, D. J. Schaefer, and B. K. Rutt, "Peripheral nerve stimulation properties of head and body gradient coils of various sizes," *Magnetic Resonance in Medicine*, vol. 50, no. 1, pp. 50–58, 2003.

[62] S.-K. Lee, J.-B. Mathieu, D. Graziani, J. Piel, E. Budesheim, E. Fiveland, C. J. Hardy, E. T. Tan, B. Amm, T. K.-F. Foo, *et al.*, "Peripheral nerve stimulation characteristics of an asymmetric head-only gradient coil compatible with a high-channel-count receiver array," *Magnetic resonance in medicine*, vol. 76, no. 6, pp. 1939–1950, 2016.

[63] S. J. Doran, L. Charles-Edwards, S. A. Reinsberg, and M. O. Leach, "A complete distortion correction for mr images: I. gradient warp correction," *Physics in Medicine & Biology*, vol. 50, no. 7, p. 1343, 2005.

[64] A. Janke, H. Zhao, G. J. Cowin, G. J. Galloway, and D. M. Doddrell, "Use of spherical harmonic deconvolution methods to compensate for nonlinear gradient effects on mri images," *Magnetic Resonance in Medicine: An Official Journal of the International Society for Magnetic Resonance in Medicine*, vol. 52, no. 1, pp. 115–122, 2004.

[65] P. T. While, L. K. Forbes, and S. Crozier, "Designing gradient coils with reduced hot spot temperatures," *Journal of Magnetic Resonance*, vol. 203, no. 1, pp. 91–99, 2010.

[66] M. Davids, B. Guérin, A. vom Endt, L. R. Schad, and L. L. Wald, "Prediction of peripheral nerve stimulation thresholds of mri gradient coils using coupled electromagnetic and neurodynamic simulations," *Magnetic resonance in medicine*, vol. 81, no. 1, pp. 686–701, 2018.

[67] C. Ham, J. Engels, G. Van de Wiel, and A. Machielsen, "Peripheral nerve stimulation during mri: effects of high gradient amplitudes and switching rates," *Journal of Magnetic Resonance Imaging*, vol. 7, no. 5, pp. 933–937, 1997.

[68] E. A. Turk, E. Kopanoglu, S. Guney, K. E. Bugdayci, Y. Z. Ider, V. B. Erturk, and E. Atalar, "A simple analytical expression for the gradient induced potential on active implants during mri," *IEEE Transactions on Biomedical Engineering*, vol. 59, no. 10, pp. 2845–2851, 2012.

[69] K. Ertan, S. Taraghinia, E. U. Saritas, and E. Atalar, "Local optimization of diffusion encoding gradients using a z-gradient array for echo time reduction in dwi," in *Proceedings of the 26th Annual Meeting of ISMRM, Paris, France*, 2018.

[70] P. Hagmann, L. Jonasson, P. Maeder, J.-P. Thiran, V. J. Wedeen, and R. Meuli, "Understanding diffusion mr imaging techniques: from scalar diffusion-weighted imaging to diffusion tensor imaging and beyond," *Radiographics*, vol. 26, no. suppl_1, pp. S205–S223, 2006.

[71] R. Bammer, M. Markl, A. Barnett, B. Acar, M. Alley, N. Pelc, G. Glover, and M. Moseley, "Analysis and generalized correction of the effect of spatial gradient field distortions in diffusion-weighted imaging," *Magnetic Resonance in Medicine*, vol. 50, no. 3, pp. 560–569, 2003.

[72] D. K. Jones and P. J. Basser, "“squashing peanuts and smashing pumpkins”: how noise distorts diffusion-weighted mr data," *Magnetic Resonance in Medicine*, vol. 52, no. 5, pp. 979–993, 2004.

[73] M. Weiger, J. Overweg, M. B. Rösler, R. Froidevaux, F. Hennel, B. J. Wilm, A. Penn, U. Sturzenegger, W. Schuth, M. Mathlener, *et al.*, "A high-performance gradient insert for rapid and short-t2 imaging at full duty cycle," *Magnetic resonance in medicine*, vol. 79, no. 6, pp. 3256–3266, 2018.

[74] K. Ertan, S. Taraghinia, H. Mohammadi, and E. Atalar, "Gradient field design for rf excitation in simultaneous multi-slice and simultaneous multi-slab imaging by using a z-gradient array," in *Proceedings of the 25th Annual Meeting of ISMRM, Honolulu, Hawaii, USA*, 2017.

[75] B. A. Gagoski, B. Bilgic, C. Eichner, H. Bhat, P. E. Grant, L. L. Wald, and K. Setsompop, "Rare/turbo spin echo imaging with simultaneous multislice wave-caipi," *Magnetic resonance in medicine*, vol. 73, no. 3, pp. 929–938, 2015.

[76] S. Moeller, E. Yacoub, C. A. Olman, E. Auerbach, J. Strupp, N. Harel, and K. Uğurbil, "Multiband multislice ge-epi at 7 tesla, with 16-fold acceleration using partial parallel imaging with application to high spatial and temporal whole-brain fmri," *Magnetic resonance in medicine*, vol. 63, no. 5, pp. 1144–1153, 2010.

[77] K. Setsompop, B. A. Gagoski, J. R. Polimeni, T. Witzel, V. J. Wedeen, and L. L. Wald, "Blipped-controlled aliasing in parallel imaging for simultaneous multislice echo planar imaging with reduced g-factor penalty," *Magnetic resonance in medicine*, vol. 67, no. 5, pp. 1210–1224, 2012.

[78] J. Schulz, R. Boyacioğlu, and D. G. Norris, "Multiband multislab 3 d time-of-flight magnetic resonance angiography for reduced acquisition time and improved sensitivity," *Magnetic resonance in medicine*, vol. 75, no. 4, pp. 1662–1668, 2016.

[79] D. L. Parker and J. R. Hadley, "Multiple-region gradient arrays for extended field of view, increased performance, and reduced nerve stimulation in magnetic resonance imaging," *Magnetic Resonance in Medicine*, vol. 56, no. 6, pp. 1251–1260, 2006.

[80] M. A. Bernstein, X. J. Zhou, J. A. Polzin, K. F. King, A. Ganin, N. J. Pelc, and G. H. Glover, "Concomitant gradient terms in phase contrast mr: analysis and correction," *Magnetic resonance in medicine*, vol. 39, no. 2, pp. 300–308, 1998.

[81] J. Pauly, P. Le Roux, D. Nishimura, and A. Macovski, "Parameter relations for the shinnar-le roux selective excitation pulse design algorithm (nmr imaging)," *IEEE transactions on medical imaging*, vol. 10, no. 1, pp. 53–65, 1991.

[82] S. Conolly, D. Nishimura, A. Macovski, and G. Glover, "Variable-rate selective excitation," *Journal of Magnetic Resonance (1969)*, vol. 78, no. 3, pp. 440–458, 1988.

[83] W. Lu, K. B. Pauly, G. E. Gold, J. M. Pauly, and B. A. Hargreaves, "Semac: slice encoding for metal artifact correction in mri," *Magnetic Resonance in Medicine*, vol. 62, no. 1, pp. 66–76, 2009.

[84] R. Turner, "A target field approach to optimal coil design," *Journal of physics D: Applied physics*, vol. 19, no. 8, p. L147, 1986.

[85] K. Ertan and E. Atalar, "Simultaneous use of linear and nonlinear gradients for b1+ inhomogeneity correction," *NMR in Biomedicine*, vol. 30, no. 9, p. e3742, 2017.

[86] K. Ertan and E. Atalar, "Simultaneous use of linear and nonlinear gradients as independent k-space variables for rf excitation," in *Proceedings of the 22nd Annual Scientific Meeting of ISMRM, Milan, Italy*, 2014.

[87] K. Ertan and E. Atalar, "Simultaneously driven linear and nonlinear gradients as independent k-space variables for rf excitation experimental validation," in *Proceedings of the 32nd Annual Scientific Meeting of ESMRMB, Edinburg, UK*, 2015.

[88] J. Pauly, D. Nishimura, and A. Macovski, "A k-space analysis of small-tip-angle excitation," *Journal of Magnetic Resonance (1969)*, vol. 81, no. 1, pp. 43–56, 1989.

[89] J. T. Schneider, M. Haas, W. Ruhm, J. Hennig, and P. Ullmann, "Robust spatially selective excitation using radiofrequency pulses adapted to the effective spatially encoding magnetic fields," *Magnetic resonance in medicine*, vol. 65, no. 2, pp. 409–421, 2011.

[90] M. Haas, P. Ullmann, J. Schneider, H. Post, W. Ruhm, J. Hennig, and M. Zaitsev, "Pexloc—parallel excitation using local encoding magnetic fields with nonlinear and nonbijective spatial profiles," *Magnetic resonance in medicine*, vol. 70, no. 5, pp. 1220–1228, 2013.

[91] E. Kopanoglu, U. Yilmaz, Y. Gokhalk, and E. Atalar, "Specific absorption rate reduction using nonlinear gradient fields," *Magnetic resonance in medicine*, vol. 70, no. 2, pp. 537–546, 2013.

[92] Z. Ugray, L. Lasdon, J. Plummer, F. Glover, J. Kelly, and R. Martí, "Scatter search and local nlp solvers: A multistart framework for global optimization," *INFORMS Journal on Computing*, vol. 19, no. 3, pp. 328–340, 2007.

[93] L. I. Sacolick, F. Wiesinger, I. Hancu, and M. W. Vogel, "B1 mapping by bloch-siegert shift," *Magnetic Resonance in Medicine*, vol. 63, no. 5, pp. 1315–1322, 2010.

[94] E. Kopanoglu and R. T. Constable, "Radiofrequency pulse design using nonlinear gradient magnetic fields," *Magnetic resonance in medicine*, vol. 74, no. 3, pp. 826–839, 2015.

[95] A. S. Childs, S. J. Malik, D. P. O'Regan, and J. V. Hajnal, "Impact of number of channels on rf shimming at 3t," *Magnetic Resonance Materials in Physics, Biology and Medicine*, vol. 26, no. 4, pp. 401–410, 2013.

[96] R. Stollberger and P. Wach, "Imaging of the active b1 field in vivo," *Magnetic Resonance in Medicine*, vol. 35, no. 2, pp. 246–251, 1996.

[97] C. H. Cunningham, J. M. Pauly, and K. S. Nayak, "Saturated double-angle method for rapid b1+ mapping," *Magnetic Resonance in Medicine*, vol. 55, no. 6, pp. 1326–1333, 2006.

[98] W. Grissom, L. Sacolick, and M. Vogel, "B1+ inhomogeneity compensation using 3d parallel excitation is enhanced by simultaneous linear and nonlinear gradient encoding," in *Proceedings of the 19th Annual Meeting of ISMRM, Montreal, Canada*, vol. 2898, 2011.

[99] Q. Duan, P. van Gelderen, and J. Duyn, "Tailored excitation using nonlinear b0-shims," *Magnetic resonance in medicine*, vol. 67, no. 3, pp. 601–608, 2012.

[100] S. Umesh Rudrapatna, C. Juchem, T. W. Nixon, and R. A. de Graaf, "Dynamic multi-coil tailored excitation for transmit b 1 correction at 7 tesla," *Magnetic resonance in medicine*, vol. 76, no. 1, pp. 83–93, 2016.

[101] C. Ma, D. Xu, K. F. King, and Z.-P. Liang, "Joint design of spoke trajectories and rf pulses for parallel excitation," *Magnetic resonance in medicine*, vol. 65, no. 4, pp. 973–985, 2011.

[102] W. A. Grissom, M.-M. Khalighi, L. I. Sacolick, B. K. Rutt, and M. W. Vogel, "Small-tip-angle spokes pulse design using interleaved greedy and local optimization methods," *Magnetic resonance in medicine*, vol. 68, no. 5, pp. 1553–1562, 2012.

[103] A. L. Alexander, J. S. Tsuruda, and D. L. Parker, "Elimination of eddy current artifacts in diffusion-weighted echo-planar images: the use of bipolar gradients," *Magnetic Resonance in Medicine*, vol. 38, no. 6, pp. 1016–1021, 1997.

[104] C. T. Harris, W. B. Handler, and B. A. Chronik, "A new approach to shimming: the dynamically controlled adaptive current network," *Magnetic resonance in medicine*, vol. 71, no. 2, pp. 859–869, 2014.

[105] R. Kimmlingen, M. Gebhardt, J. Schuster, M. Brand, F. Schmitt, and A. Haase, "Gradient system providing continuously variable field characteristics," *Magnetic Resonance in Medicine*, vol. 47, no. 4, pp. 800–808, 2002.

[106] P. R. Harvey and E. Katznelson, "Modular gradient coil: A new concept in high-performance whole-body gradient coil design," *Magnetic Resonance in Medicine*, vol. 42, no. 3, pp. 561–570, 1999.

[107] J. Pauly, D. Nishimura, and A. Macovski, "A linear class of large-tip-angle selective excitation pulses," *Journal of Magnetic Resonance (1969)*, vol. 82, no. 3, pp. 571–587, 1989.

[108] R. Bowtell and P. Mansfield, "Gradient coil design using active magnetic screening," *Magnetic resonance in medicine*, vol. 17, no. 1, pp. 15–21, 1991.

[109] K. Ertan, S. Taraghinia, A. Takmaz, S. E. Dogan, S. Ozdemir, and E. Atalar, "Spatiotemporal magnetic field monitoring with hall effect sensors," in *Proceedings of the 25th Annual Meeting of ISMRM, Honolulu, Hawaii, USA*, 2017.

[110] C. Barmet, N. D. Zanche, and K. P. Pruessmann, "Spatiotemporal magnetic field monitoring for mr," *Magnetic Resonance in Medicine*, vol. 60, no. 1, pp. 187–197, 2008.

[111] B. E. Dietrich, D. O. Brunner, B. J. Wilm, C. Barmet, S. Gross, L. Kasper, M. Haeberlin, T. Schmid, S. J. Vannesjo, and K. P. Pruessmann, "A field camera for mr sequence monitoring and system analysis," *Magnetic resonance in medicine*, vol. 75, no. 4, pp. 1831–1840, 2016.

[112] N. De Zanche, C. Barmet, J. A. Nordmeyer-Massner, and K. P. Pruessmann, "Nmr probes for measuring magnetic fields and field dynamics in mr systems," *Magnetic Resonance in Medicine*, vol. 60, no. 1, pp. 176–186, 2008.

Appendix A

Spatiotemporal Magnetic Field Monitoring with Hall Effect Sensors

This study is related to measure both temporal and spatial dependency of the gradient fields during the MRI scan. Although proposed technique is appropriate for gradient fields generated by gradient arrays as well as conventional gradients, conventional gradients are used for the proof of concept studies. Therefore, this study is presented in the Appendix. This chapter uses some content from previously presented conference abstract [109].

A.1 Introduction

Due to hardware imperfections and physical limitations, magnetic fields during an imaging sequence is never exactly same as it is expected by a pulse programmer. The imperfections cause artifacts in the image, however, as long as they are precisely measured, resulting artifacts and image distortions can be corrected. NMR probes have already been used to monitor both spatial and temporal dependency of the magnetic fields which leads to estimation of the correct k-space trajectory to be used in the image reconstruction [110]. Later dynamic field camera has been developed to measure field dynamics up to third order spherical harmonics including 16 NMR probes [111]. Although, NMR is a very suitable way of field monitoring, requirement of spectrometer for the NMR probes, transmit and low noise RX chain for all probes as well as demanding constructing process of the NMR probes [112] might lead to a significant cost increase.

As an alternative, we propose to use Hall effect sensors to monitor the spatiotemporal field dynamics. However, measurement of the z component of the magnetic field (B_z) requires very large dynamic range for the Hall effect sensors due to superposition of encoding fields with main magnetic field (B_0). Instead, we propose to measure the transverse components of the magnetic field in several spatial positions to reconstruct spatiotemporal dependency of B_z using the Maxwell equations with the spherical harmonics order dependent on the number of sensors.

A.2 Methods

A.2.1 Reconstruction Technique

Hall effect sensors might be used to measure directly Bz inside the MRI scanner; however, field deviations on the order of ppms of the (B_0) can be effective in the images and should be monitored. Such a dynamic range is not practical and will result in either very low sensitivity or saturation of the sensor. Ideally, when Hall elements are aligned to measure concomitant fields, there will be no interference with the main magnetic fields which will not cause saturation and high sensitivity can be maintained. Additionally, if the direction of the current in Hall element is aligned with the z-direction inside the MR scanner, Maxwell equation can be written in the form which directly leads to the following Eq. A.1a.

$$\nabla \times B = \hat{a}_x \left(\frac{\partial B_z}{\partial y} - \frac{\partial B_y}{\partial z} \right) + \hat{a}_y \left(\frac{\partial B_z}{\partial x} - \frac{\partial B_x}{\partial z} \right) + \hat{a}_z \left(\frac{\partial B_y}{\partial x} - \frac{\partial B_x}{\partial y} \right) = \hat{a}_z \mu_0 J \tag{A.1a}$$

$$\frac{\partial B_z}{\partial y} = \frac{\partial B_y}{\partial z} \tag{A.1b}$$

$$\frac{\partial B_z}{\partial x} = \frac{\partial B_x}{\partial z} \tag{A.1c}$$

where J is the current density on the Hall elements, μ_0 is the free space permeability. Eq. A.1a directly implies Eqs. A.1b-c using simple algebraic steps. Therefore measuring the z-derivative of the transverse fields is enough to determine the x and y derivatives of the z-directed magnetic field.

Furthermore, remaining partial derivative of the B_z can be determined from the zero divergence condition as in Eq. A.2. Therefore, knowledge of transverse fields is adequate to determine the all partial derivatives of the B_z, in other words ∇B_z. However, spatial DC component cannot be determined with this formulation. Since DC term is not used to calculate B_z, measurement at three point is adequate to measure first order spherical harmonics of B_x and B_y. Afterwards, by using Eq. A.1 and Eq. A.2, B_z can be calculated up to same order spherical harmonics with B_x and B_y.

$$\nabla \cdot B = \frac{\partial B_x}{\partial x} + \frac{\partial B_y}{\partial y} + \frac{\partial B_z}{\partial z} = 0 \tag{A.2a}$$

$$\frac{\partial B_z}{\partial z} = -\frac{\partial B_x}{\partial x} - \frac{\partial B_y}{\partial y} \tag{A.2b}$$

A.2.2 Experiments

Two commercially available Hall effect sensors (DRV5053, Texas Instruments) with 20 kHz bandwidth and 23 mV/mT sensitivity are used to measure magnetic field in x and -y directions. Fig. A.1 shows the image of the experimental setup.Sensors are manually aligned perpendicular to z-axis by adjusting the sensor output to 0 Volts. There is also support structure holding the sensor in a fixed

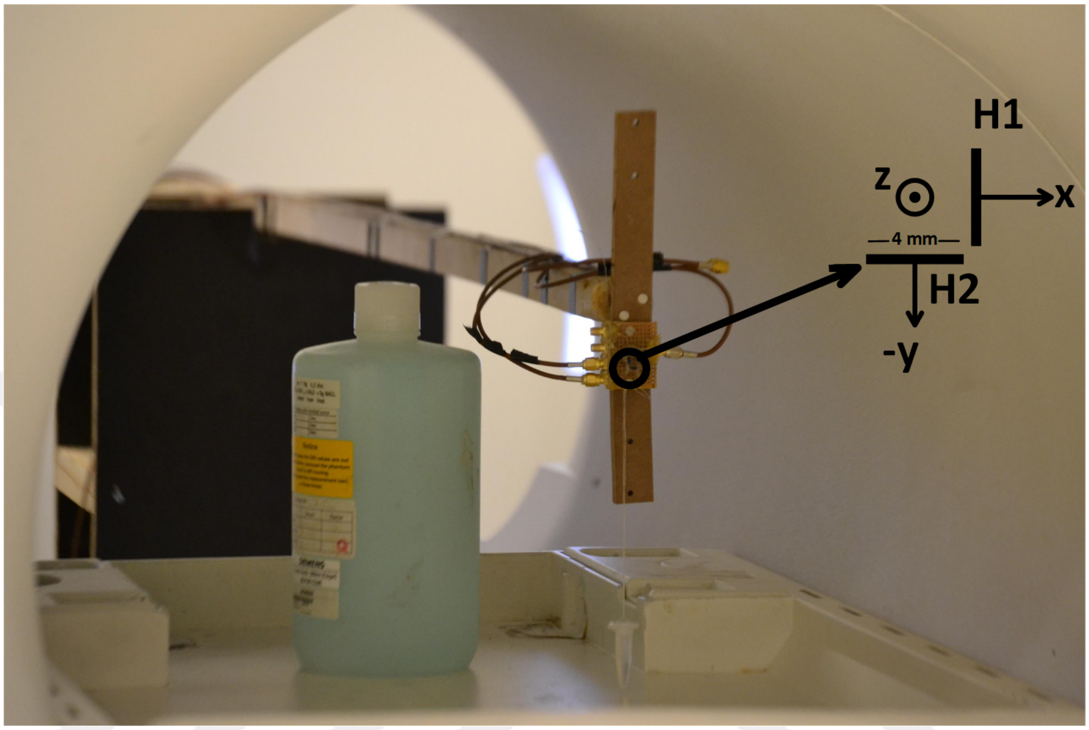

Figure A.1: Experimental Setup including two Hall effect sensors, and support structure. One of them is aligned to measure the field in the –y direction and other one is aligned to measure the field in +x direction.

position so that after initial calibration, sensors will stay perpendicular to z position when they are moved to other position. There is also additional apparatus connected to holder in order to determine the exact position of the sensors.

Data is digitized with the ADC of an oscilloscope (Ds07104B, Agilent Technologies). Experiments are performed with a 3T MRI Scanner (Tim Trio, Siemens). To demonstrate the proof of concept, sensors are placed at 3 different positions in 3 different scans due to insufficient number of sensors. At each scan, y-gradient is applied with strength of 20mT/m, rise and fall times of 2ms and flat top duration of 12ms.

A.3 Results

Magnetic field in x and y directions are measured in 3 different spatial locations as in Fig. A.2. By using the magnetic field levels at each time and inverse of the probing matrix1, spatiotemporal dependency of B_x and B_y are constructed up to first order spherical harmonics as in Fig. A.2a and Fig. A.2b. After B_x and B_y are determined, B_z is determined using the Eq. A.1 and A.2 and it is shown in Fig. A.2c. In Fig. A.2c, red plot shows the applied y-gradient during sequence with reasonably consistent timing and amplitude. This three plots is enough to determine the first order spatial variations of the magnetic field as well as temporal dynamics.

A.4 Discussion and Conclusion

Proposed technique cannot measure the spatial DC component. Only one channel NMR probe can be used as a reference point to estimate the DC component. Our method requires double number of sensors compared to NMR probes because field is measured in two directions in our case which leads to an advantage of measuring concomitant field directly without any processing. Alignment and measuring the position of the sensors are extremely important in the precision. As a conclusioin, feasibility of measuring the three-dimensional spatiotemporal dependency of magnetic field during an MRI scanner with Hall effect sensors are demonstrated with preliminary experiments.

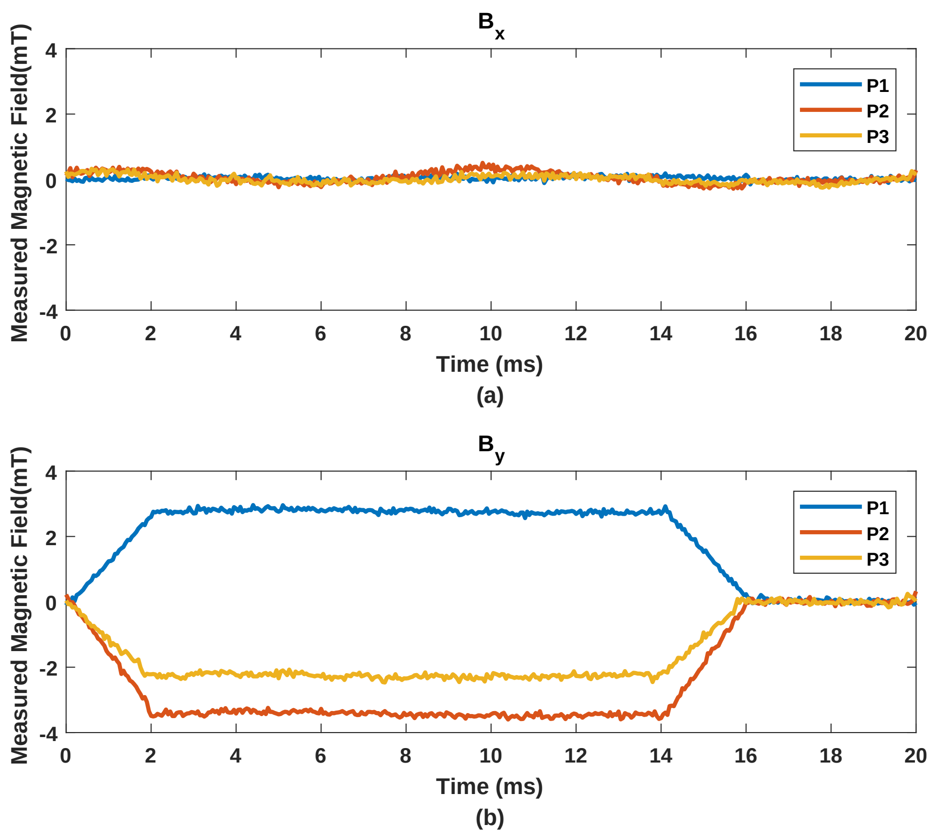

Figure A.2: Measured sensor output voltages are converted to magnetic field. **(a)** B_x, x component of the magnetic field **(b)** B_y, y component of the magnetic field. Measurements are obtained at 3 different spatial positions to be able to reconstruct first order spherical harmonics.

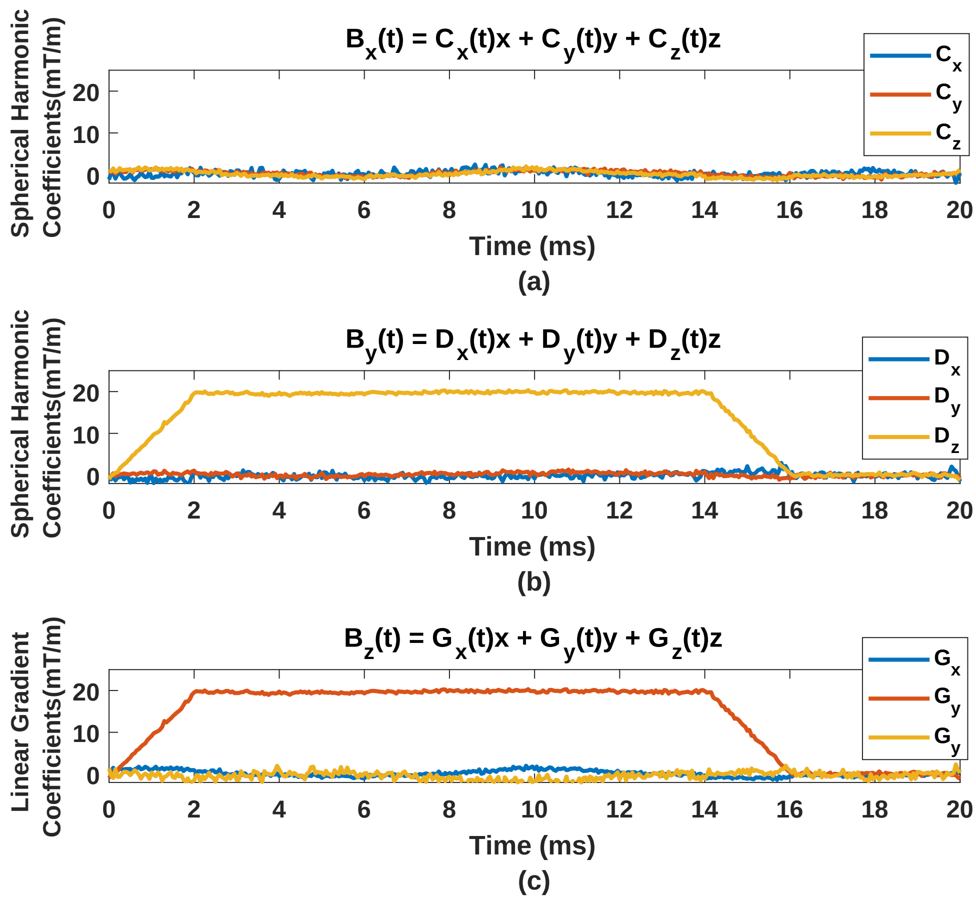

Figure A.3: Reconstructed first order spherical harmonic coefficients in 3 axes for **(a)** B_x, x component of the magnetic field, **(b)** B_y, y component of the magnetic field, **(c)** B_z, z component of the magnetic field.